ALTERATIONS IN BONE TISSUE PROPERTIES WITH PARATHYROID HORMONE TREATMENT

A Dissertation

Presented to the Faculty of the Graduate School

of Cornell University

In Partial Fulfillment of the Requirements for the Degree of

Doctor of Philosophy

by

Julia Ting Hsuan Chen

May 2018

ALTERATIONS IN BONE TISSUE PROPERTIES WITH PARATHYROID HORMONE TREATMENT

Julia Ting Hsuan Chen, Ph.D.

Cornell University 2018

Osteoporosis, an age-related bone disease characterized by low bone mass, is a potential public health problem responsible for over 8.9 million fractures annually. From an engineering perspective to understanding the mechanism of increased fragility with osteoporosis, we applied engineering theory to study this complex composite material, bone. Amount of bone, bone distribution, and tissue material properties are determinants of whole bone strength. Parathyroid hormone (PTH, teriparatide, hPTH [1-34]) is a FDA-approved anabolic osteoporosis treatment. PTH has shown to reduce fracture risk by over 50% and increased bone volume fraction. However, the alterations in material properties and mechanical properties with PTH treatment, and the correlations to bone mechanical failure are unknown. The objectives of this research were to 1) examine alterations in microstructure and tissue properties of both cortical and cancellous bone with PTH treatment using an osteopenia sheep model, and 2) investigate the influence of microstructure and anisotropic material properties on crack propagation in a pre-notched cortical beam under bending.

To investigate the alterations in tissue properties across different length scales,

a large, multi-level experiment was designed for both cortical and cancellous bone in an osteopenia sheep model. The first study focused on cortical bone and the effect of PTH treatment was greater at the micro- and nanoscale than at the whole bone level. There was no difference with whole-bone strength; however, fatigue life has shown to increase compared to other bisphosphonate-treated samples whereas fracture toughness was decreased in PTH-treated group and osteon density was higher. Furthermore, mineralization increased whereas indentation modulus decreased and hardness reduced with PTH treatment. Millimeter and nano-scale material properties were correlated with whole bone strength, but fatigue properties correlated little to bending strength or fracture toughness.

In the second study, cancellous bone was examined. There was no difference in monotonic compressive strength with PTH treatment; however, PTH-treated group preserved mechanical properties during cyclic loading compared to vehicle group. Additionally, PTH increased the volume fraction of rod-type trabeculae and decreased mineralization whereas nanoindentaion and hardness were not different. Correlating tissue composition, microstructure, and mechanical performance, energy dissipation was highly correlated with volume fraction of rods and mineralization.

In the third study, fracture behavior in a single pre-notched cortical bone tissue was examined with finite element based simulation software (FRANC2D). The role of anisotropy of fracture toughness and of altered microstructure in crack trajectory and the force needed to propagate a crack was investigated. Cortical bone with more osteons located further away from the applied loads to maximize intact material would withstand more load before propagating cracks and fracturing.

BIOGRAPHICAL SKETCH

The Taiwanese writer Chu Tien-hsin wrote: “A shimmering ocean, a beautiful island, the essential site of our wise ancestors' destiny.". This is where Julia Ting Hsuan Chen was born in 1989. She attended the National Cheng Kung University studying mechanical engineering. While at NCKU, Julia served as Treasurer and President to Student Association in Mechanical Engineering. During her last 6 months in undergraduate, she was accepted to the international student exchange program to study in Technische Universität München, Germany. In 2012 summer, Julia graduated with a Bachelor’s of Science in Mechanical Engineering and received the Outstanding Undergraduate Award.

In the following fall she began her doctoral studies at Cornell University under the guidance of Marjolein van der Meulen. A year later, she received the Graduate Research Fellowship from the National Science Foundation. While at Cornell, Julia served as Treasurer to the Sibley Graduates in Mechanical and Aerospace Engineering, a Social Chair to the Cornell Taiwanese Student Association and received American Society for Bone and Mineral Research Young Investigator Travel Award. She also pursued her love for teaching, serving as a Teaching Assistant for statics and mechanics of solids, and participated in the Center for Teaching Excellence Fellowship program. Julia earned her M.S. degree in Mechanical Engineering in 2015 and received her Ph.D. in the same field in December 2017.

This work is dedicated to my parents, my family and my homeland, Taiwan.

ACKNOWLEDGMENTS

The completion of this thesis would not have been possible without the support of many people. First and foremost, I would like to express my sincere gratitude to my committee chair, Dr. Marjolein van der Meulen, for her scientific knowledge, incredible mentorship, and the opportunity to pursue a Ph.D. I would also like to thank committee members Dr. Christopher Hernandez and Dr. Derek Warner for their expertise and guidance. I thank Dr. Adele Boskey and Dr. Anthony Ingraffea for their enthusiasm and technical knowledge with these studies.

Lab members past and present, Grace Kim, Garry Brock, Frank Ko, Natalie Kelly, Olufunmilayo Adebayo, Derek Holyoak, Sophia Ziemian, Carolyn Chlebek, as well as all of the biomechanics faculty and students for being extremely supportive and providing insights and valuable feedback on research presentations and conference abstracts. I would like to thank Kirk Gunsallus, John Grazul, Kit Umbach, and Ryan Peterson for instrument training and technical advice. Judy Thoroughman and Marcia Swayer, thank you for your advice along the way, your help with administrative forms and ordering lab supplies.

Joyce Fang, I-Tzu Chen, SzuYu Cheng and Ting-Yu Lee, thank you for the emotional support when I needed it the most. You guys received excited or frustrated texts/phone calls 24/7 and always lent a sympathetic ear. Pankaj Singh, thank you for sharing many wonderful meals and memories with me. Your problem solving abilities and optimism will always be something I aspire to. SzuChen Yeh, thank you for always being there for me with your patience, calm and laughter. You tolerate me so

well and being my strong supporter when I lose my way. Finally, a thank you to my parents for their endless love and encouragement since the day I was born.

Speaking of coffee, I'd like to thank the staff of Gimme! in downtown for tolerating my presence once a week (and sometimes much more often than that) for the past year. Their coffee kept me writing.

Funding for this research was provided by a National Science Foundation Graduate Research Fellowship and by NIH grant R01-AR041325. This work made use of the Cornell Center for Materials Research Facilities and Cornell BRC-Imaging Facilities supported by National Science Foundation under Award Number DMR-1120296 and S10OD012287 respectively.

TABLE OF CONTENT

LIST OF FIGURE

LIST OF TABLES

CHAPTER 1

INTRODUCTION*

Musculoskeletal tissues such as bone play critical roles in bearing the loads created during activities of daily living. As a result, mechanical properties of bone are critical to its function and relevant to clinical conditions. Understanding the basic composition and architecture of bone tissue provides a base from which to understand tissue function and mechanical behavior. Diseases and other pathologic conditions often alter the mechanical properties of bone tissue resulting in disruptions of normal function. To be successful, treatments must restore/maintain the mechanical function.

1.1 Bone Composition and Architecture

Bone is the most abundant of the musculoskeletal tissues. Bone tissue contains 40% inorganic mineral, 35% organic matrix, and 25% water by weight. The inorganic phase is made of a ceramic crystalline type of mineral called hydroxyapatite. The organic phase is composed primarily of type I collagen, along with minor collagen types and noncollagenous proteins. When loaded, the mineral contributes to compressive behavior, and the collagen contributes to tensile behavior. Additionally, bone is a hierarchical material (Figure 1.1). At the lowest level (approximately 0.1 μm scale), bone consists of mineralized collagen fibrils embedded within the organic extracellular matrix. These fibrils are arranged into lamellae (7 to 10 μm thick). Circumferential structures of multiple lamellae with a central Haversian canal form

*Adapted from: Julia T. Chen, Timothy M. Wright, Marjolein C.H. van der Meulen. Musculoskeletal biomechanics. Orthopaedic Knowledge Update 12. Chapter 11.

structures known as osteons (approximately 200 μm in diameter). Lamellae and osteons are arranged into cortical or cancellous bone tissue at the highest level of scale, greater than 1 mm. Cortical bone consists of densely packed and longitudinally oriented osteons and lamellae. Cancellous bone, also known as trabecular bone, is an open cellular structure with a spatially variable microstructure consisting of individual struts or trabeculae.

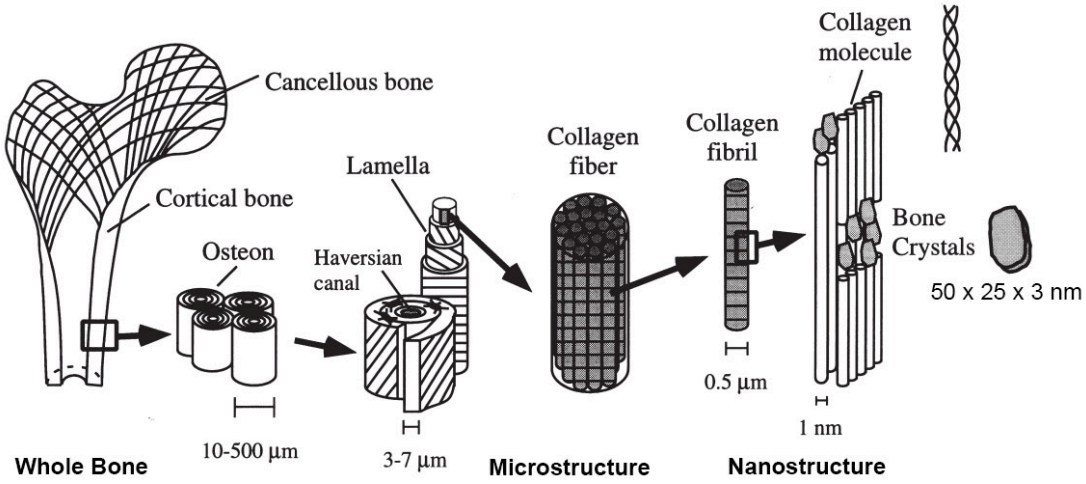

Figure 1.1 *Hierarchical structure of bone from macro- to nano-scale. Image adapted from Rho et al.*[(1)].

Bone tissue can change its microstructure and composition actively through the tissue's ability to repair damage and adapt to its mechanical environment by coordinated cellular activity known as modeling or remodeling. Modeling occurs primarily during growth and involves net bone formation and shaping through bone formation by osteoblasts and/or resorption by osteoclasts. Remodeling replaces old or damaged bone tissue and creates new tissue. In contrast to modeling, remodeling is performed by the coupled action of the osteoclast and osteoblast cells in bone.

Osteoclasts and osteoblasts are the key actors in bone remodeling; osteocytes are believed to be the sensors. Ideally, the amount of new bone formed is equal to the volume of older tissue removed. With age, however, this process becomes less efficient, and bone loss outpaces new bone formation, leading to reduced bone strength. This progressive bone loss leads to the development of osteoporosis and can be counteracted through the suppression of remodeling, particularly in cases of high bone turnover. High turnover rates increase cortical porosity and weaken cancellous bone through the loss of connectivity between trabecular plates and struts.[2] Various musculoskeletal diseases differentially affect tissue composition and turnover and thus, mechanical properties (Table 1.1).

Table 1.1 *Tissue Alterations Induced by Musculoskeletal Diseases and Effects on Mechanical Properties of Bone Tissue*

Tissue Alteration	Clinical Condition	Modulus	Ultimate Stress	Toughness
No or low turnover	Osteoporosis, atypical femoral fracture, irradiated bone, pycnodysostosis	↑	↓	↓
High turnover	Postmenopausal osteoporosis[3]	↑	↓	↓
Poor collagen	Marfan syndrome, scurvy, osteogenesis imperfecta, Ehlers Danlos syndrome	↓	↓	↓
Poor mineralization	Osteomalacia, hypophosphatasia, hypophosphatemic rickets, renal osteodystrophy	↓	↓	↓

In addition to variations in apparent level properties, spatial variations in tissue properties are important because these local changes are evident in the behavior of cracks initiation and propagation[4,5]. Osteons are layered concentric ring-like structures within cortical bone. Osteonal tissue is less mineralized and less stiff compared to interstitial matrix, which is primary bone tissue and has been present longer than osteonal tissue[6]. Through remodeling, tissue age, different from the age of animal, within single osteon increases from the center of the osteon towards the periphery[7]. In cortical bone in primates, material properties and nanomechanical properties vary due to tissue age in the osteon[8,9]. In the cancellous bone, tissue age increases towards the center of each trabecula; therefore, greater treatment effects are expected near the surfaces of trabeculae[10,11].

1.2 Bone Quality versus Bone Quantity

Clinically, reduced bone mass are diagnosed by dual-energy x-ray absorptiometry, and the reported bone mineral density (BMD) serves as the quantitative evaluation of osteoporotic fracture risk. BMD has limitations in predicting fracture risk. Small increases in BMD do not correspond with substantial changes in fracture risk in some populations such as women without vertebral fractures[12]. Factors other than BMD that may contribute to fracture risk often are referred to collectively as “bone quality.” Therefore, the term bone quality is quite broad and includes bone geometry, cancellous morphology, and material properties[13]. Some key concepts from

biomechanics regarding the determinants of whole bone structural strength are required to help define bone quality[1,14].

For bone quality, the structure of interest is the whole bone. In terms of structural behavior, different mechanical tests, such as bending, tension, and torsion, can be used to determine structural strength and structural stiffness. From these tests, structural strength is defined as the failure load of the whole bone, and structural stiffness is defined as the ability to resist deformation for a given load[15]. These two structural measurements are influenced by the geometric distribution of the material and the material properties of the tissue[1,14].

Geometry can be determined by a variety of techniques, including noninvasive imaging methods such as CT and MRI or destructive sectioning methods. The material properties of tissue are more difficult to assess. Tissue composition can be measured by chemical methods such as Fourier transform infrared spectroscopy (FTIR) and Raman spectroscopy[10]. Tissue mineral content also can be obtained from microcomputed tomography[16]. The mechanical properties of the tissue can be measured directly by the mechanical testing of small samples and the indentation of small tissue volumes[13].

1.3 Mechanical and Material Properties of Bone at Apparent-Level

Because of this hierarchical microstructure and composition, the material properties of bone are anisotropic, varying in different directions, and viscoelastic, depending on

the rate of loading. Cortical bone tissue loaded in the longitudinal direction along the axis of a long bone is stiffer and stronger than when loaded in the transverse direction[17] (Figure 1.2). The stresses experienced by cortical bone during activities of daily living such as walking and running are largest in the longitudinal direction. In addition to having anisotropic properties in a given loading direction, cortical bone strength is greater in compression than in tension (Figure 1.2)[17]. The strength and stiffness of cortical bone tissue also depend on the loading rate. When the material is loaded more quickly, cortical bone behaves more stiffly, but the amount of deformation until failure (ultimate strain) decreases[18]. In cancellous bone, these material properties are difficult to generalize. The material properties depend on the apparent density through an exponential relationship[19]. Like cortical bone, the compressive yield strength of cancellous bone is greater than its tensile yield strength.

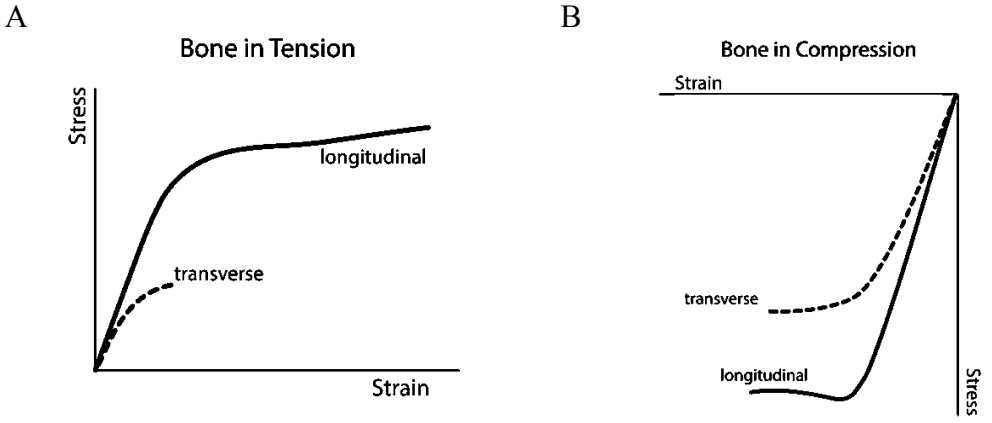

Figure 1.2 *Representative stress-strain curves are shown for bone (A) in tension and (B) compression. Two curves are shown reflecting different behavior as a result of specimen orientation relative to the applied load (longitudinal/transverse).*

Traditionally, the focus of tissue mechanical behavior has been on whole bone and tissue stiffness and failure strength, as described previously. Most in vivo loading experienced under normal activity is cyclic; thus, cyclic loading and fatigue behavior have gained renewed importance.

Fatigue loading is cyclic with low magnitude loads, the stresses of which are well below the ultimate stress required to fracture bone tissue in a single overload (Figure 1.3). Fatigue loads are created through repetitive activities such as walking and running. When a tissue is subjected to fatigue loading, localized damage to the structure, such as microcracks, is initiated. With continued cyclic loading, cracks accumulate and propagate, reaching critical lengths, and the structure fails. This structural fatigue failure also occurs in stress fractures.

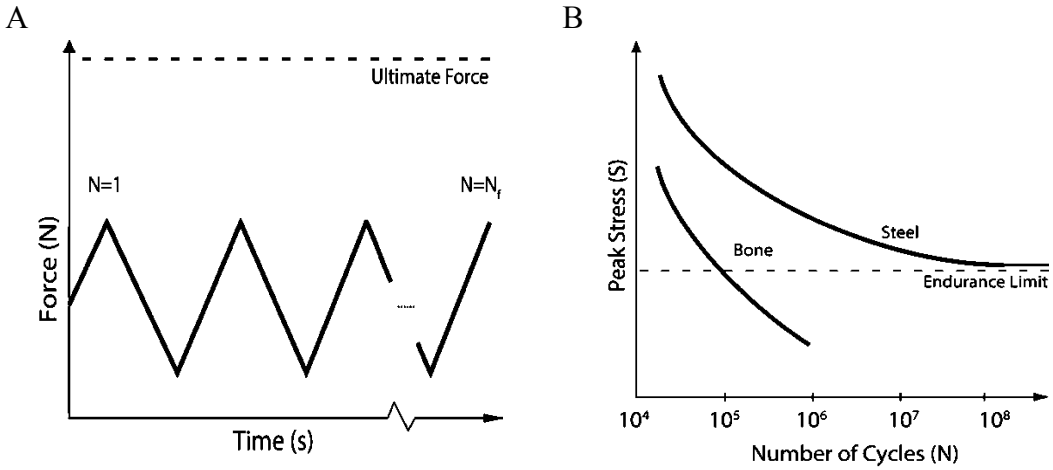

Figure 1.3 *Graphs show applied cyclic loading and key outcomes for fatigue testing. Fatigue behavior is determined by applying cyclic loading over time to a material sample (**A**) and measuring the number of cycles to failure to produce peak stress (S) versus the number of cycles to failure (N), resulting in the representative S-N curves shown for bone and steel (**B**). Steel displays an endurance limit, a stress below which failure never occurs, whereas bone does not have an endurance limit.*

The fatigue properties of bone have been studied for several decades, and most of this work has been performed by examining cortical bone. Fatigue life is influenced by loading direction, strain rate, and osteoporosis treatment. Fatigue life of cortical bone was longer in compression than in tension[20]. Strain rate affects damage accumulation in cortical bone; cyclic loading at high physiologic strain rates causes more damage than at low strain rates[21]. Osteoporosis treatments alter the fatigue properties as well. In two recent studies, fatigue life was increased following anabolic osteoporosis treatment, but the resistance of cortical bone to failure declined with catabolic osteoporosis treatment[22,23].

Limited data are available for the fatigue behavior of cancellous bone. As for conventional materials, cancellous fatigue life declines with an increase in applied strain magnitude. In addition, microcrack propagation in cancellous bone under fatigue loading is determined by tissue heterogeneity not by local tissue stress. Damage was formed near the centers of trabeculae instead of at the surfaces or near the remodeling cavities, indicating the differences in tissue properties at centers and surfaces were dominant for crack propagation[24]. Furthermore, fatigue damage was not generated throughout the tissue, but was concentrated at a limited number of locations far from the tissue surface, suggesting that the damage sites contain older less remodeled tissue[25].

In addition to bone strength and fatigue strength, fracture toughness, correlates with bone fragility, characterizes the ability of a material to withstand a crack without

brittle fracture occurring. The mechanical properties from monotonic loading and fatigue tests are obtained assuming that no unusual cracks are present in the material. However, cracks do exist in most bone tissue and affect failure. Therefore, understanding the ability to resist crack growth is essential. Fracture toughness is determined by the tension, bending, or cyclic loading of a sample with a notch that localizes crack formation[26,27]. Measured values depend on the notch direction and microstructures[4,5,28]. For example, transverse fracture toughness is higher than longitudinal fracture toughness[28,29]. Fracture toughness has been positively correlated with osteon density but negatively correlated with bone porosity[4,5]. Moreover, as crack propagates in bone tissue, fracture toughness increases[26,27].

These three tissue properties (bone strength, fracture toughness, and fatigue strength) are independent but correlated with each other[30]. Based on the common clinical fracture modes, the differential effects of alterations in these three tissue properties have been noted[31]. For example, the prodromal symptoms and radiographic appearance of atypical femoral fractures (AFF) are similar to those of stress fractures and thus suggest fatigue failure. AFFs are characterized by a unique transverse fracture line and bilateral occurrence[32], occurring under normal loading conditions such as walking in postmenopausal women. AFFs occur in the cortex at a location that normally does not easily fracture, indicating high whole-bone strength, and have been suggested instead to be caused by fatigue loading with accumulated microdamage and insufficient fracture toughness. The fracture trajectory is a transverse crack growth, consistent with impaired fracture toughness rather than insufficient bone strength[33,34].

1.4 Nanomechanics and Tissue Composition of Bone

To characterize tissue-level mechanical properties and composition, nanoindentation, Raman spectroscopy, FTIR, and Second Harmonic Generation spectroscopy (SHG) are being discussed here. Tissue mechanical properties such as indentation modulus and hardness are determined by nanoindentation. Quasistatic nanoindentation tests are performed by loading and unloading an indenter of a known geometry into the sample while recording load-displacement data. Indentation modulus (E_i) and hardness (H) can be determined from load-displacement curves with Oliver-Pharr method[35]. Nanoindentation has been used to characterize tissue mechanical properties in a submicron length scale such as lamellar, interstitial and osteonal tissue[10,11].

Tissue composition such as mineral-to-matrix ratio, carbonate substitution, collagen maturity, and crystallinity can be examined by Raman spectroscopy and FTIR. Both instruments provide complimentary composition data about the mineral and organic phases of bone. Raman spectroscopy has higher resolution and can be performed on bulk samples whereas FTIR needs thick sections. Inelastic scattered light, interacting with vibrated molecular bonds in the sample, is collected by Raman spectroscopy, whereas, FTIR measures light absorption by the bonds of a vibrating molecule. Tissue composition can be determined from peak height or peak area ratio of specific wavelengths associated with particular chemical bonds or compositions. In addition to Raman spectroscopy and FTIR, SHG microscopy measures aligned collagen content associated with higher tissue stiffness[36]. SHG creates a map of aligned collagen

content with nonlinear scattering photons from aligned collagen fibers within bone. These measurements distinguish whether the collagen is aligned within the plane[8,36,37]. The alignment of the collagen was positively correlated with tissue strength[38].

Spatial distributions in tissue composition, tissue age, cause similar variations in nanomechanical properties. In human cortical bone, osteons have lower stiffness and hardness compared to more mineralized and older interstitial tissue[7]. Similarly, in cancellous bone, stiffness and hardness are lower on the surface of a single trabecula compared to the center of the trabecula[11]. Additionally, the correlations between tissue mechanical properties and composition have been examined[11]. For example, tissue stiffness and hardness are positively correlated with mineralization[8,39]. These nanomechanical properties also follow trends in greater aligned collagen content[11].

1.5 Osteoporosis and Aging

Osteoporosis is an age-related disease, caused by loss of estrogen in women at menopause[40]. Estrogen regulates the rate and balance of remodeling. A negative balance of bone mass develops, with more bone resorbed than formed in each remodeling cycle, due to the loss of estrogen. In addition to estrogen loss, activation frequency of bone multicellular units (BMUs), the number of new BMUs created per unit volume per unit time[41], is age-dependent[42]. Activation frequency of BMUs declines from childhood to a minimum at about age 35, and then rises and falls again at the end of life-span[43] (Figure 1.4). As a result of loss of estrogen[44] and increased

activation frequency, bone mass drops rapidly with postmenopausal type I osteoporosis in women.

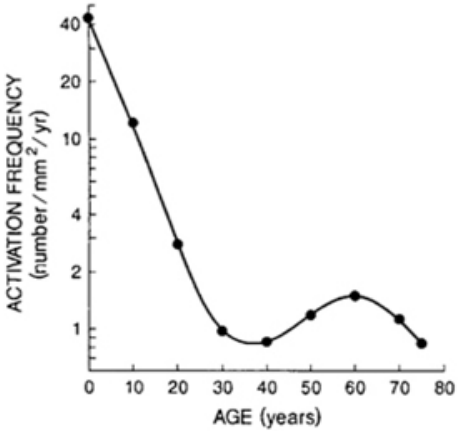

Figure 1.4 *Activation frequency of BMU versus human age. Figure adapted from Martin et al.*[42].

With age, apparent level strength and stiffness of cortical and cancellous bone both decline resulting from increased porosity and decreased apparent density [45,46]. Osteon numbers increase, and osteon dimensions are altered[47,48]. For example, in aging humans, osteonal area tends to decrease, which might reflect the higher probability that larger osteons are remodeled[49]. Haversian canal area tends to increase[42], which could result from reduced osteoblast lifetimes or reduced apposition rates[50].

In addition to microstructural alteration, osteoporosis alters tissue composition and nanomechanical properties as well. Bone tissue mineralization was reduced, carbonate substitution and crystallinity were increased in ovariectomized animal models and patients with osteoporotic fractures[51,52]. Few studies have examined changes in mechanical properties with osteoporosis; however, they appear not to change. Indentation modulus and hardness did not differ between normal and osteoporotic

patients[53]. Moreover, due to different metabolic activities in cortical and cancellous bone, mechanical properties with osteoporosis in each bone type would be affected differently[54,55].

1.6 Osteoporosis Treatment and Its Effects on Bone Tissue Properties

Anti-resorptive agents used to treat osteoporosis include bisphosphonates such as alendronate, zoledronate, and risedronate, selective estrogen receptor modulators (SERMs, tamoxifen and raloxifene), and antibodies to RANKL (denosumab). The most commonly prescribed class of antiresorptive therapy is the bisphosphonates. These agents are quite effective and reduce osteoporotic fractures by 40% to 50%[56]. Inhibiting resorption overcomes the deficits in bone mass associated with insufficient bone formation during elevated bone remodeling. These treatments are intended to reduce elevated bone turnover rates to normal levels, thereby improving bone strength and reducing the incidence of fracture.

Apparent strength and stiffness of bone tissue are increased with bisphosphonate treatment[57]. Fatigue life under cyclic compressive loading, however, was reduced in bisphosphonate-treated osteopenia sheep compared to PTH-treated group[22]. This reduction could be due to several factors including altered tissue properties, decreased heterogeneity of the properties or microdamage accumulation. At the tissue-level, indentation modulus, hardness and mineral-to-matrix ratio were increased with bisphosphonate treatment in sheep [11]. Tissue heterogeneity was decreased as measured by Fourier transform infrared spectroscopy (FTIR) imaging[58]. Furthermore,

bisphosphonate use is associated with microdamage accumulation, resulting in loss of toughness and fatigue life[22,59]. The effects of long-term suppression of bone turnover on bone mechanical properties are not well understood, particularly whether the lack of bone turnover has consequences for tissue renewal and the repair of tissue damage. In fact, AFFs are associated with long-term bisphosphonate use, suggesting an adverse effect of the prolonged suppression of bone remodeling[32]. Although the mechanism of AFF is unknown and has been suggested to reflect damage accumulation due to inadequate tissue renewal, other factors such as lower-limb geometry[60] and loading also may contribute to their development.

In addition to catabolic osteoporosis treatment, two anabolic osteoporosis treatments are currently approved by the Food and Drug Administration (FDA): teriparatide (PTH [1-34]) and abaloparatide (PTHrP analog). Both anabolic treatments increase bone turnover and stimulate osteoblasts more than osteoclasts (Figure 1.5), opposite to the mechanism of anti-resorptive treatments[61]. The life span of osteoblasts is prolonged, the number of osteoblasts is increased, and bone formation is stimulated[62-65]. The effect of PTH depends on the injection frequency. When PTH is administered continuously, bone resorption increases. However, if PTH is given intermittently, bone formation increases[66].

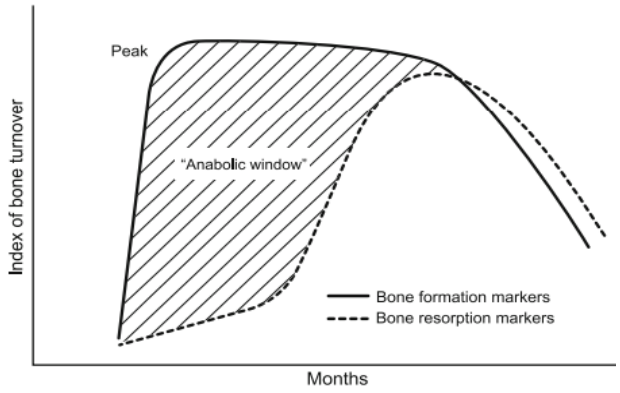

Figure 1.5 *Intermittent PTH administration stimulated osteoblasts more than osteoclasts. Figure adapted from Gallacher et al.*[61].

PTH decreases fracture risk at both vertebrae and hip by over 50%[67]. On average BMD increases by 10-14%[68,69]. Regarding microstructural features, trabecular thickness and connectivity increase with PTH treatment whereas bisphosphonate treatment only stabilizes and preserves trabecular architecture[68,69]. In cortical bone, however, changes are not as evident with PTH treatment as in cancellous tissue due to different metabolic activities. Elevated endocortical remodeling with PTH treatment slightly decreases cortical BMD and increases cortical porosity[69]. Biomechanical properties, however, are not altered. Periosteal apposition increases cortical diameter and thickness, balancing out the BMD reduction biomechanically[69].

Many studies also have examined apparent mechanical properties in small animal models with PTH treatment. Bone strength was increased with PTH treatment in intact animal models[70,71]. Furthermore, PTH increased bone strength at the femoral neck and vertebra in ovariectomized rat models[72,73]. Fewer studies have examined changes in mechanical properties with PTH treatment in large animal models[74-76]. The proximal femur was stronger with PTH treatment compared to ovariectomized

monkeys; even after withdrawal of 6 months, the treatment effect was still retained[76]. In addition, a study utilizing tissue from the exact same sheep from Chapter 2 and Chapter 3 has demonstrated prolonged fatigue life of cortical bone with PTH treatment compared to bisphosphonate treatment [22]. However, its effect on bone tissue composition should also be examined to fully understand the mechanisms contributing to fracture.

1.7 Simulation on Mechanical Behavior of Bone Tissue

As the ability to image the skeleton in vivo has improved, the data acquired for additional noninvasive analyses have become important resources. Over the past decade, computational methods have been developed to simulate the mechanical behavior of the skeleton in healthy individuals. These approaches are noninvasive and inexpensive. Using in vivo CT of bone, the patient's specific skeletal geometry is converted to a three-dimensional computational model that can simulate a mechanical test and identify fracture risk[77]. This approach captures not only the overall bony geometry of sites such as the hip, spine, or distal radius, but also the relative material properties of cancellous bone (Figure 1.6). Quantitative CT values for cancellous bone can be converted to tissue density and is related to tissue stiffness in the laboratory[78].

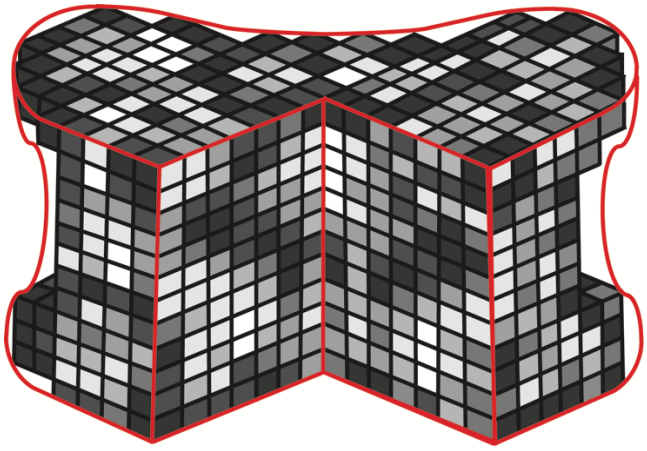

Figure 1.6 *Illustration depicts a three-dimensional finite element model of a vertebral body developed from CT image data with the front quarter removed. The red line shows the geometric outline of the vertebra. The cubes are individual finite elements, and the gray scale represents different material properties. The individual CT voxels are converted to finite elements with variable material properties based on the attenuation values from the scan.*

The finite element method (FEM) is a computational technique used to perform mechanical analyses. Complex geometries and material distributions are analyzed by replacing a continuous structure with a discrete model structure of small subunits (finite elements) whose mechanical behavior is defined well. The discretization (geometric representation and element characteristics), boundary conditions (applied loading and interfaces), and material properties (generally, linear and elastic) determine the quality of the model solution. Because FEM requires discretizing a complex geometry, the conversion of image voxels from CT to a geometric finite element model is straightforward, and bone material properties can be assigned to each element based on CT attenuation values. When loads are applied to the model to simulate the in vivo activities of interest, the simulation predicts the mechanical behavior of the model. Even though FEM analysis requires computational time, this

noninvasive method can capture complex loading conditions and geometries; thus predicting fracture locations well when compared with the reference of mechanical testing[79].

Another simulation approach focusing on crack propagation and crack tip analysis is a quasi-automated computer code based on finite element method (FRacture Analysis Code)[80]. FRANC automatically meshes in an arbitrary region in which a crack propagates and calculates the driving force in front of the crack tip regardless of the mixity of fracture modes[81,82] (Figure 1.7). In addition to automatically re-meshing around the crack tip without losing unaffected structure information, other main features of FRANC are predicting crack trajectory, calculating the local stability and stress intensity factor. Displacement correlation[83,84], modified crack closure integral[85], and the equivalent domain correlation[86] approaches are different methods to calculate stress intensity factors. All methods generate accurate results[87] whereas the latter two approaches are more reliable when the cracks are under complex mixed-mode loading[80]. Furthermore, FRANC overcomes the limitation of current FEM simulation software that lacking ability to continuously re-mesh the model to accommodate incremental crack extension.

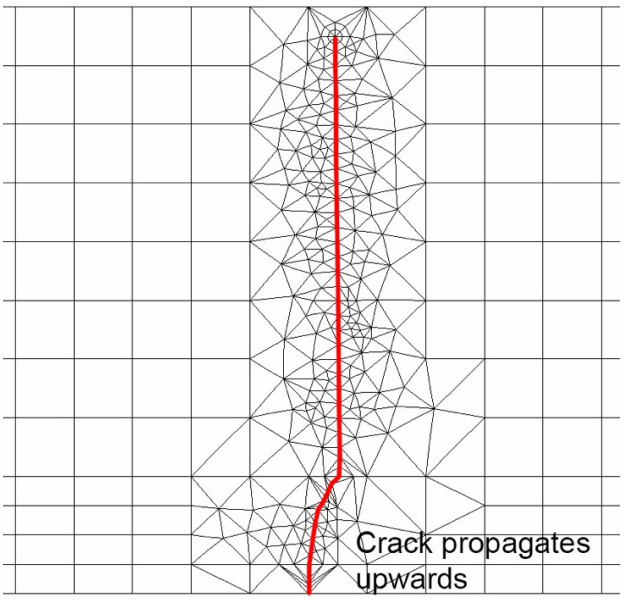

Figure 1.7 *Illustration of FRANC2D model with re-meshing along the crack tip (shown in red).*

1.8 Study Objectives and Significance

Osteoporosis is a bone disease associated with fracture, due to an imbalance in bone remodeling favoring bone resorption. Bone quantity and quality are decreased with osteoporosis[11,52,88,89]. Parathyroid hormone (PTH), an FDA-approved anabolic osteoporosis treatment, increases bone mass in animal studies[62,71,75], but its effect on bone tissue composition and mechanics is unknown. Moreover, few studies utilize larger animal models with Haversian remodeling that better capture the dynamics of human bone tissue. Sheep experience a similar aging process including menopause and reproductive hormone profile as human does[90,91]. In this research, osteopenia was induced in mature sheep using ovariectomy combined with a metabolic acidosis diet

for two years. During the second year, sheep were treated with PTH (PTH, $n = 7$, 5μg/kg/day) or saline (vehicle, $n = 6$).

For the first objective, the alterations of mechanical and material properties of cortical bone with PTH treatment in an osteopenia sheep model were examined. We hypothesized that PTH would increase bone mass and elevate tissue properties to resist bone failure due to altered tissue composition. We performed multi-scale analysis to determine the contribution of tissue-scale material changes to whole bone mechanical behavior. Whole-bone mechanical performance and morphology (bending strength, bending stiffness, and cross-sectional moment of inertia) were determined in femurs using four-point bending tests and CT scans. Millimeter-scale specimens of cortical bone from the mid-shaft of right femur were used to determine tissue fatigue strength and fracture toughness. Nano-scale characterization of cortical bone tissue included nanoindentation, Raman spectroscopy, and second harmonic generation microscopy (SHG). The correlation among whole bone bending strength, fatigue behavior, and fracture toughness were determined. This study is the first to compare and correlate all three mechanical failure properties: whole bone strength, fatigue behavior, and fracture toughness.

For the second objective, the effects of PTH treatment on bone tissue composition and mechanics of cancellous bone in an osteopenia sheep model were investigated. We hypothesized that PTH would increase tissue heterogeneity and preserve mechanical properties during cyclic loading through architectural and compositional changes. In each animal two cancellous samples were taken from the distal femur: one for

monotonic loading and one for cyclic fatigue loading. Samples were subjected to microCT scanning and individual trabecular segmentation (ITS) to determine volume fraction of rod- and plate-like trabeculae. Then specimens were failed in compression to determine cancellous bone strength or cyclic loading to evaluate fatigue life and energy dissipation. Cancellous tissue mechanics and composition were analyzed by nanoindentation and Raman spectroscopy. In addition, specimens from iliac crest and vertebra were obtained for characterizing PTH effect on bone quality and tissue heterogeneity with histomorphometry, FTIRI and a novel nanoscale infrared technique called AFM-IR. All the experimental sheep were subjected to bone density and serum measurements.

Our third objective was to use a computational mechanics approach to investigate the role of anisotropy of fracture toughness and of altered microstructure in crack trajectory and the energy of propagating a crack in cortical bone. Previous simulations demonstrated that strength and fracture properties of osteons affected crack propagation[92-94], mostly based on isotropic fracture toughness. Anisotropic fracture toughness is more representative of bone, but difficult to measure. Simulations were performed because limited experimental data are available for anisotropic fracture toughness. A 2x20 mm pre-notched (0.05 mm initial crack on tensile side) beam was created in Franc2D and loaded in 3-point bending. We altered anisotropic fracture toughness of osteon, osteon location, number and diameter for different simulation cases. Crack trajectory was examined, and normalized critical load was calculated, indicating the load needed to propagate a unit length of a crack. Investigating the role

of microstructure and anisotropy of fracture toughness in crack propagation simulations provided additional insight into crack propagation mechanisms in bone and ultimately understanding bone fragility.

References

1. Rho J-Y, Kuhn-Spearing L, Zioupos P. Mechanical properties and the hierarchical structure of bone. Medical engineering & physics. 1998;20(2):92-102.

2. Epstein S. The roles of bone mineral density, bone turnover, and other properties in reducing fracture risk during antiresorptive therapy. Mayo Clinic Proceedings: Elsevier; 2005. p. 379-88.

3. Garnero P, Sornay-Rendu E, Chapuy MC, Delmas PD. Increased bone turnover in late postmenopausal women is a major determinant of osteoporosis. Journal of Bone and Mineral Research. 1996;11(3):337-49.

4. Yeni Y, Brown C, Wang Z, Norman T. The influence of bone morphology on fracture toughness of the human femur and tibia. Bone. 1997;21(5):453-9.

5. Yeni YN, Norman TL. Calculation of porosity and osteonal cement line effects on the effective fracture toughness of cortical bone in longitudinal crack growth. Journal of Biomedical Materials Research Part A. 2000;51(3):504-9.

6. Fratzl P. Hierarchical structure and mechanical adaptation of biological materials. Learning From Nature How to Design New Implantable Biomaterials: From Biomineralization Fundamentals to Biomimetic Materials and Processing Routes,(NATO Science Series II: Mathematics, Physics and Chemistry Vol 171), RL Reis and S Weiner, eds, Kluwer Academic Publishers, Amsterdam. 2004:15-34.

7. Rho JY, Zioupos P, Currey JD, Pharr GM. Microstructural elasticity and regional heterogeneity in human femoral bone of various ages examined by nano-indentation. Journal of biomechanics. 2002;35(2):189-98.

8. Burket J, Gourion-Arsiquaud S, Havill LM, Baker SP, Boskey AL, Van der Meulen MC. Microstructure and nanomechanical properties in osteons relate to tissue and animal age. Journal of Biomechanics. 2011;44(2):277-84.

9. Gourion-Arsiquaud S, Burket JC, Havill LM, et al. Spatial variation in osteonal bone properties relative to tissue and animal age. Journal of Bone and Mineral Research. 2009;24(7):1271-81.

10. Donnelly E, Boskey AL, Baker SP, Van der Meulen MC. Effects of tissue age on bone tissue material composition and nanomechanical properties in the rat cortex. Journal of Biomedical Materials Research. 2010;92(3):1048-56.

11. Burket JC, Brooks DJ, MacLeay JM, Baker SP, Boskey AL, van der Meulen MC. Variations in nanomechanical properties and tissue composition within trabeculae from an ovine model of osteoporosis and treatment. Bone. 2013;52(1):326-36.

12. Cummings SR, Karpf DB, Harris F, et al. Improvement in spine bone density and reduction in risk of vertebral fractures during treatment with antiresorptive drugs. The American journal of medicine. 2002;112(4):281-9.

13. Donnelly E. Methods for assessing bone quality: a review. Clinical Orthopaedics and Related Research®. 2011;469(8):2128-38.

14. Cole JH, van der Meulen MC. Whole bone mechanics and bone quality. Clinical Orthopaedics and Related Research®. 2011;469(8):2139-49.

15. Turner CH, Burr DB. Basic biomechanical measurements of bone: a tutorial. Bone. 1993;14(4):595-608.

16. Bourne BC, van der Meulen MC. Finite element models predict cancellous apparent modulus when tissue modulus is scaled from specimen CT-attenuation. Journal of biomechanics. 2004;37(5):613-21.

17. Reilly DT, Burstein AH. The elastic and ultimate properties of compact bone tissue. Journal of biomechanics. 1975;8(6):393IN9397-396IN11405.

18. McElhaney JH, Fogle JL, Melvin JW, Haynes RR, Roberts VL, Alem NM. Mechanical properties of cranial bone. Journal of biomechanics. 1970;3(5):495IN5497-496511.

19. Rice J, Cowin S, Bowman J. On the dependence of the elasticity and strength of cancellous bone on apparent density. Journal of biomechanics. 1988;21(2):155-68.

20. Carter DR, Caler WE, Spengler DM, Frankel VH. Fatigue behavior of adult

cortical bone: the influence of mean strain and strain range. Acta Orthopaedica Scandinavica. 1981;52(5):481-90.

21. Schaffler M, Radin E, Burr D. Mechanical and morphological effects of strain rate on fatigue of compact bone. Bone. 1989;10(3):207-14.

22. Brock GR, Chen JT, Ingraffea AR, et al. The effect of osteoporosis treatments on fatigue properties of cortical bone tissue. Bone Reports. 2015;2:8-13.

23. Bajaj D, Geissler JR, Allen MR, Burr DB, Fritton JC. The resistance of cortical bone tissue to failure under cyclic loading is reduced with alendronate. Bone. 2014;64:57-64.

24. Torres AM, Matheny JB, Keaveny TM, Taylor D, Rimnac CM, Hernandez CJ. Material heterogeneity in cancellous bone promotes deformation recovery after mechanical failure. Proceedings of the National Academy of Sciences. 2016;113(11):2892-7.

25. Goff M, Lambers F, Nguyen T, Sung J, Rimnac C, Hernandez C. Fatigue-induced microdamage in cancellous bone occurs distant from resorption cavities and trabecular surfaces. Bone. 2015;79:8-14.

26. Nalla RK, Kruzic JJ, Kinney JH, Ritchie RO. Effect of aging on the toughness of human cortical bone: evaluation by R-curves. Bone. 2004;35(6):1240-6.

27. Vashishth D. Rising crack-growth-resistance behavior in cortical bone:: implications for toughness measurements. Journal of Biomechanics. 2004;37(6):943-6.

28. Phelps J, Hubbard G, Wang X, Agrawal C. Microstructural heterogeneity and the fracture toughness of bone. Journal of Biomedical Materials Research. 2000;51(4):735-41.

29. Koester KJ, Iii JA, Ritchie R. The true toughness of human cortical bone measured with realistically short cracks. Nature Materials. 2008;7(8):672.

30. Hernandez C, van der Meulen M. Understanding Bone Strength Is not Enough. Journal of Bone and Mineral Research. 2017.

31. Hernandez CJ, van der Meulen MC. Understanding Bone Strength Is Not Enough. Journal of Bone and Mineral Research. 2017.

32. Shane E, Burr D, Abrahamsen B, et al. Atypical subtrochanteric and diaphyseal femoral fractures: second report of a task force of the American Society for Bone and Mineral Research. Journal of Bone and Mineral Research. 2014;29(1):1-23.

33. Shane E, Burr D, Ebeling PR, et al. Atypical subtrochanteric and diaphyseal femoral fractures: report of a task force of the American Society for Bone and Mineral Research. Journal of Bone and Mineral Research. 2010;25(11):2267-94.

34. Schilcher J, Sandberg O, Isaksson H, Aspenberg P. Histology of 8 atypical femoral fractures: remodeling but no healing. Acta orthopaedica. 2014;85(3):280-6.

35. Rho JY, Tsui TY, Pharr GM. Elastic properties of human cortical and trabecular lamellar bone measured by nanoindentation. Biomaterials. 1997;18(20):1325-30.

36. Boyd RW. Nonlinear optics: Academic press; 2003.

37. Zipfel WR, Williams RM, Webb WW. Nonlinear magic: multiphoton microscopy in the biosciences. Nature biotechnology. 2003;21(11):1369-77.

38. Viguet-Carrin S, Garnero P, Delmas P. The role of collagen in bone strength. Osteoporosis international. 2006;17(3):319-36.

39. Kim G, Boskey AL, Baker SP, van der Meulen MC. Improved prediction of rat cortical bone mechanical behavior using composite beam theory to integrate tissue level properties. Journal of biomechanics. 2012;45(16):2784-90.

40. Khosla S, Melton LJ, Riggs BL. The unitary model for estrogen deficiency and the pathogenesis of osteoporosis: is a revision needed? Journal of Bone and Mineral Research. 2011;26(3):441-51.

41. Martin R. On the histologic measurement of osteonal BMU activation

frequency. Bone. 1994;15(5):547-9.

42. Martin RB, Burr DB. Structure, function, and adaptation of compact bone: Raven Pr; 1989.

43. Frost H. The Laws of Bone Structure. 1–165. Springfield, IL: Charles P Thomas. 1964.

44. Lindsay R, Hart D, Clark D. The minimum effective dose of estrogen for prevention of postmenopausal bone loss. Obstetrics & Gynecology. 1984;63(6):759-63.

45. Zioupos P, Currey J. Changes in the stiffness, strength, and toughness of human cortical bone with age. Bone. 1998;22(1):57-66.

46. McCalden RW, McGeough JA. Age-related changes in the compressive strength of cancellous bone. The relative importance of changes in density and trabecular architecture. JBJS. 1997;79(3):421-7.

47. Evans FG. Mechanical properties and histology of cortical bone from younger and older men. The Anatomical Record. 1976;185(1):1-11.

48. Currey JD. Some effects of ageing in human Haversian systems. Journal of anatomy. 1964;98(1):69.

49. Pirok D, Ramser J, Takahashi H, Villanueva AR, Frost HM. Normal histological, tetracycline and dynamic parameters in human, mineralized bone sections. Henry Ford Hospital medical journal. 1966;14(2):195-218.

50. Merz W, Schenk R. A quantitative histological study on bone formation in human cancellous bone. Cells Tissues Organs. 1970;76(1):1-15.

51. Gadeleta S, Boskey A, Paschalis E, et al. A physical, chemical, and mechanical study of lumbar vertebrae from normal, ovariectomized, and nandrolone decanoate-treated cynomolgus monkeys (Macaca fascicularis). Bone. 2000;27(4):541-50.

52. McCreadie BR, Morris MD, Chen TC, et al. Bone tissue compositional differences in women with and without osteoporotic fracture. Bone. 2006;39(6):1190-5.

53. Fratzl-Zelman N, Roschger P, Gourrier A, et al. Combination of nanoindentation and quantitative backscattered electron imaging revealed altered bone material properties associated with femoral neck fragility. Calcified tissue international. 2009;85(4):335-43.

54. Burchardt H. The biology of bone graft repair. Clinical orthopaedics and related research. 1983;174:28-34.

55. Davis JW, Ross PD, Wasnich RD. Evidence for both generalized and regional low bone mass among elderly women. Journal of Bone and Mineral Research. 1994;9(3):305-9.

56. Bilezikian JP. Efficacy of bisphosphonates in reducing fracture risk in postmenopausal osteoporosis. The American journal of medicine. 2009;122(2):S14-S21.

57. Allen MR, Burr DB. Mineralization, microdamage, and matrix: how bisphosphonates influence material properties of bone. BoneKEy-Osteovision. 2007;4(2):49-60.

58. Donnelly E, Meredith DS, Nguyen JT, et al. Reduced cortical bone compositional heterogeneity with bisphosphonate treatment in postmenopausal women with intertrochanteric and subtrochanteric fractures. Journal of Bone and Mineral Research. 2012;27(3):672-8.

59. Mashiba T, Hirano T, Turner CH, Forwood MR, Johnston CC, Burr DB. Suppressed bone turnover by bisphosphonates increases microdamage accumulation and reduces some biomechanical properties in dog rib. Journal of Bone and Mineral Research. 2000;15(4):613-20.

60. Morin SN, Wall M, Belzile EL, et al. Assessment of femur geometrical parameters using EOS™ imaging technology in patients with atypical femur fractures; preliminary results. Bone. 2016;83:184-9.

61. Gallacher S, Dixon T. Impact of treatments for postmenopausal osteoporosis

(bisphosphonates, parathyroid hormone, strontium ranelate, and denosumab) on bone quality: a systematic review. Calcified tissue international. 2010;87(6):469-84.

62. Jilka RL, Weinstein RS, Bellido T, Roberson P, Parfitt AM, Manolagas SC. Increased bone formation by prevention of osteoblast apoptosis with parathyroid hormone. Journal of Clinical Investigation. 1999;104(4):439-46.

63. Dobnig H, Turner RT. Evidence that intermittent treatment with parathyroid hormone increases bone formation in adult rats by activation of bone lining cells. Endocrinology. 1995;136(8):3632-8.

64. de Bakker CM, Altman AR, Tseng W-J, et al. μCT-based, in vivo dynamic bone histomorphometry allows 3D evaluation of the early responses of bone resorption and formation to PTH and alendronate combination therapy. Bone. 2015;73:198-207.

65. Leder BZ, O'dea LSL, Zanchetta JR, et al. Effects of abaloparatide, a human parathyroid hormone-related peptide analog, on bone mineral density in postmenopausal women with osteoporosis. The Journal of Clinical Endocrinology & Metabolism. 2015;100(2):697-706.

66. Hock J, Gera I. Effects of continuous and intermittent administration and inhibition of resorption on the anabolic response of bone to parathyroid hormone. Journal of bone and mineral research. 1992;7(1):65-72.

67. Greenblatt D. Treatment of postmenopausal osteoporosis. Pharmacotherapy: The Journal of Human Pharmacology and Drug Therapy. 2005;25(4):574-84.

68. Quattrocchi E, Kourlas H. Teriparatide: a review. Clinical therapeutics. 2004;26(6):841-54.

69. Hodsman AB, Bauer DC, Dempster DW, et al. Parathyroid hormone and teriparatide for the treatment of osteoporosis: a review of the evidence and suggested guidelines for its use. Endocrine reviews. 2005;26(5):688-703.

70. Hirano T, Burr DB, Turner CH, Sato M, Cain RL, Hock JM. Anabolic effects of human biosynthetic parathyroid hormone fragment (1–34), LY333334, on remodeling and mechanical properties of cortical bone in rabbits. Journal of

bone and Mineral Research. 1999;14(4):536-45.

71. Oxlund H, Ejersted C, Andreassen T, Tørring O, Nilsson M. Parathyroid hormone (1-34) and (1-84) stimulate cortical bone formation both from periosteum and endosteum. Calcified tissue international. 1993;53(6):394-9.

72. Ejersted C, Andreassen T, Hauge E-M, Melsen F, Oxlund H. Parathyroid hormone (1–34) increases vertebral bone mass, compressive strength, and quality in old rats. Bone. 1995;17(6):507-11.

73. Søgaard C, Wronski T, McOsker J, Mosekilde L. The positive effect of parathyroid hormone on femoral neck bone strength in ovariectomized rats is more pronounced than that of estrogen or bisphosphonates. Endocrinology. 1994;134(2):650-7.

74. Turner C, Wang T, Hirano T, et al. In primates, treatment with PTH (1-34), LY333334, increases bone strength at trabecular bone sites without compromising the strength of cortical bone. Journal of Bone and Mineral Research. 1999;14:S414-S.

75. Fox J, Miller M, Newman M, Recker R, Turner C, Smith S. Effects of daily treatment with parathyroid hormone 1–84 for 16 months on density, architecture and biomechanical properties of cortical bone in adult ovariectomized rhesus monkeys. Bone. 2007;41(3):321-30.

76. Sato M, Westmore M, Ma YL, et al. Teriparatide [PTH (1–34)] strengthens the proximal femur of ovariectomized nonhuman primates despite increasing porosity. Journal of Bone and Mineral Research. 2004;19(4):623-9.

77. Keaveny TM. Biomechanical computed tomography—noninvasive bone strength analysis using clinical computed tomography scans. Annals of the New York Academy of Sciences. 2010;1192(1):57-65.

78. Morgan EF, Bayraktar HH, Keaveny TM. Trabecular bone modulus–density relationships depend on anatomic site. Journal of Biomechanics. 2003;36(7):897-904.

79. Luu AN, Anez-Bustillos L, Aran S, et al. Microstructural, densitometric and metabolic variations in bones from rats with normal or altered skeletal states.

PloS one. 2013;8(12):e82709.

80. Bittencourt T, Wawrzynek P, Ingraffea A, Sousa J. Quasi-automatic simulation of crack propagation for 2D LEFM problems. Engineering Fracture Mechanics. 1996;55(2):321-34.

81. Wawrzynek PA, Ingraffea A. Interactive finite element analysis of fracture processes: an integrated approach. Theoretical and Applied Fracture Mechanics. 1987;8(2):137-50.

82. Wawrzynek PA, Ingraffea AR. An interactive approach to local remeshing around a propagating crack. Finite Elements in Analysis and Design. 1989;5(1):87-96.

83. Tracey DM. Finite elements for determination of crack tip elastic stress intensity factors. Engineering Fracture Mechanics. 1971;3(3):255-65.

84. Tracey D. Discussion of 'on the use of isoparametric finite elements in linear fracture mechanics' by RS Barsoum. International Journal for Numerical Methods in Engineering. 1977;11(2):401-2.

85. Raju I. Calculation of strain-energy release rates with higher order and singular finite elements. Engineering Fracture Mechanics. 1987;28(3):251-74.

86. Dodds Jr RH, Vargas PM. Numerical evaluation of domain and contour integrals for nonlinear fracture mechanics: formulation and implementation aspects. University of Illinois Engineering Experiment Station. College of Engineering. University of Illinois at Urbana-Champaign.; 1988.

87. Bittencourt TN, Barry A, Ingraffea AR. Comparison of Mixed-Mode Stress-Intensity Factors Obtained Through Displacement Correlation, J-lntegral Formulation, and Modified Crack-Closure Integral. Fracture Mechanics: Twenty-Second Symposium (Volume II): ASTM International; 1992.

88. Seeman E, Martin TJ. Co-administration of Antiresorptive and Anabolic Agents: A Missed Opportunity. Journal of Bone and Mineral Research. 2015;30(5):753-64.

89. Boskey A, Mendelsohn R. Infrared analysis of bone in health and disease. Journal of biomedical optics. 2005;10(3):031102-0311029.

90. Newman E, Turner A, Wark J. The potential of sheep for the study of osteopenia: current status and comparison with other animal models. Bone. 1995;16(4):S277-S84.

91. Turner A. The sheep as a model for osteoporosis in humans. The Veterinary Journal. 2002;163(3):232-9.

92. Evans AG, He MY, Hutchinson JW. Interface debonding and fiber cracking in brittle matrix composites. Journal of the American Ceramic Society. 1989;72(12):2300-3.

93. Guo XE, He M, Goldstein SA. Understanding cement line interface in bone tissue: a linear fracture mechanics approach. ASME. 1995;29:303-.

94. Mischinski S, Ural A. Finite element modeling of microcrack growth in cortical bone. Journal of Applied Mechanics. 2011;78(4):041016.

CHAPTER 2

EXPLAINING THE EFFECTS OF PTH TREATMENT IN CORTICAL BONE IN A SHEEP MODEL OF OSTEOPOROSIS: CONTRIBUTIONS OF WHOLE BONE STRENGTH, FATIGUE BEHAVIOR AND FRACTURE TOUGHNESS*

2.1 Introduction

Osteoporosis-related fractures affect an estimated two hundred million people worldwide.(1) Patients with a prior osteoporosis-related fracture are at increased risk of experiencing a subsequent fracture.(2) Understanding the main contributors to skeletal fragility can improve fracture risk prediction. Bone mineral density (BMD), as measured by dual-energy x-ray absorptiometry, is the standard method of assessing fracture risk; however, BMD has known limitations, particularly in patients taking pharmaceuticals to address osteoporosis.(3)

The ability of a whole bone to resist fracture is determined by bone tissue mass, internal structure, and material properties.(4) Cortical bone carries a major share of the total load of the skeleton particularly in the long bones. Structural properties and intrinsic material properties of cortical bone determine its mechanical competence. Measures of BMD are sensitive to some structural properties of bone (mass and density), but not to variations in internal microstructure, tissue properties, or tissue composition.

---

*Submitted to Journal of Bone and Mineral Research. Julia T. Chen, Shefford P. Baker, Elizabeth G. Pluhar, Christopher J. Hernandez, Adele L. Boseky, Marjolein C.H. van der Meulen. Explaining the effects of PTH treatment in cortical bone in a sheep model of osteoporosis: contributions of whole bone strength, fatigue behavior

Mechanical failure of a whole bone may occur from a single load, which is sensitive to whole bone strength, from cyclic loading that is sensitive to fatigue behavior, or from sensitivity to crack growth, reflected by fracture toughness.[5] Fatigue behavior is the resistance to failure following many cycles of loading at levels well below the tissue strength, quantified as fatigue life. Fracture toughness is a material property that determines the resistance to crack growth at a stress concentration, measured in a standard three-point notch bending test. Whole bone strength, fracture toughness and fatigue behavior are interdependent,[6] and may have differential contributions to clinical fractures. For example, consider atypical femoral fractures (AFF), associated with long-term use of bisphosphonates. AFFs occur in a relatively dense cortical shell, indicating higher whole-bone strength compared to other bone tissue, but are believed to be caused by fatigue loading with accumulated microdamage and insufficient fracture toughness.[7] The fracture trajectory is a transverse crack growth, consistent with impaired fracture toughness rather than insufficient whole-bone strength.[8,9] Therefore, for a full understanding of resistance to fracture, one may need to examine whole bone strength, fracture toughness and fatigue behavior, as a function of changes in tissue composition due to either osteoporosis or therapeutics.

Several therapeutic approaches have been developed to treat osteoporosis by inhibiting bone resorption, or by enhancing bone formation.[10] In the current study, we focused on intermittent parathyroid hormone treatment (iPTH), an anabolic osteoporosis treatment that is approved for use in the US. PTH stimulates bone formation.[11] Treatment with PTH in animals led to increases in the fatigue life of

cortical bone[12] and increases in bone tissue strength.[13,14] The physical mechanism behind PTH-induced improvement in bone tissue mechanical properties is not yet known.

Cortical bone tissue strength, fracture toughness, and fatigue behavior are influenced by tissue heterogeneity and ultrastructure. In cortical bone in primates, material properties and nanomechanical properties vary due to tissue age in the osteon.[15,16] Tissue age is different from animal age resulting from remodeling process. Osteonal tissue is less mineralized and less stiff compared to interstitial matrix, which is primary bone tissue and has been present longer than osteonal tissue.[17] Through remodeling, tissue age can vary within an osteon. Tissue near the cement line has a slightly greater tissue age since it is formed first during remodeling.[18] These variations in tissue properties are important because fracture resistance is affected by local tissue properties. In addition, osteonal boundaries can influence the propagation of cracks and thereby contribute to tissue fatigue strength and fracture toughness.[19] The cement line in cortical bone tissue can serve as a toughening mechanism by deflecting crack propagation.[20] Hence, changes in tissue age and osteon density associated with bone remodeling may contribute to the ability of whole bone to resist fracture.

The objective of this study was to determine the effects of PTH on three metrics of bone mechanical performance (whole bone bending strength, fracture toughness, fatigue life) and to determine how tissue properties including nanoscale composition and mechanical properties contribute to whole bone bending strength. An ovine model was used because sheep undergo osteonal remodeling, thereby providing

a spatial material composition analysis similar to that of humans. In addition, hormone profiles of sheep are similar to those of women, especially the reproductive cycle during the breeding season.[21] We hypothesized that PTH would increase bone mass and elevate tissue properties to resist bone failure due to altered tissue composition in an ovine osteoporosis model.

2.2 Methods

2.2.1 Animal model

The present study utilized 13 mature Swiss Rambouillet ewes (6-7 years old, weighing 69-82 kg). All sheep were ovariectomized (OVX) and placed on a metabolic acidosis (MA) diet for one year to induce osteopenia.[22] All sheep in the present study were ovariectomized at the same time point to limit the effects of seasonal variations in bone mass [23]. One year following OVX and MA diet, the sheep were assigned to two treatment groups: (1) PTH group (n = 7): daily parathyroid hormone treatment (teriparatide 1-34, generously provided by Eli Lilly, 5μg/kg/day subcutaneous injection) and (2) Vehicle group (n = 6): daily saline vehicle injection for 12 months. Sheep remained on the MA diet during the 12 months of treatment. All animal procedures were reviewed and approved by the IACUC of the University of Minnesota (# 0907A68881) and the Hospital for Special Surgery (#11-09-02E).

Ewes were monitored by DEXA, and double labeled with tetracycline 4 and 9 days prior to euthanasia. Serum calcium levels, PTH levels, alkaline phosphatase

activity (ALP) and bone markers (BAP and CTx) were monitored quarterly throughout the study. Iliac crest biopsies (n = 2/sheep) were obtained from all sheep before transition to the treatment groups (after 12 months) and again at euthanasia (at 24 months). Images were collected with microCT for cortical bone volume fraction (BV/TV), tissue mineral density (TMD), and thickness (Ct.Th).

After euthanasia, femurs were harvested, wrapped in gauze soaked with PBS, and stored at -20 °C prior to specimen preparation. The right femur was preserved to assess cortical bone tissue, and the left femur was used for whole bone biomechanical analysis.

2.2.2 Cortical Bone Tissue: Fracture toughness and fatigue life

Cortical beams (n = 6-7/group) were created from the medial diaphysis of the right femurs, parallel to the long axis of the bone, using a low-speed diamond saw (Buehler Isomet; Lake Bluff, Illinois, USA). Beams were then polished using 15, 5, and 1 micron lapping films to a final size of 2 x 2 x 25 mm. Ethylene glycol was used as a lubricant to prevent mineral leaching.[24,25] After polishing, samples were notched (~200 μm deep) with a razor blade under irrigation with 1 μm diamond suspension. The orientation of the notch was transverse relative to the osteonal direction. Beams were stored at -20°C in saline-soaked gauze until testing.

Fracture toughness of cortical bone was determined using the notched three-point bending approach. The beams were thawed in PBS at 37°C for 3 hours before testing. The samples were placed in fixtures within a material testing device (Bose

Electroforce LM-1; Eden Prairie, Minnesota, USA) with a 20 mm span between the lower support rods. A compressive displacement rate of 0.015 mm/s was applied to failure. The critical load was determined, and transverse fracture toughness was calculated using the ASTM E399 standard.[26] Each fracture test was recorded using a high-speed camera (4000 fps with 248 μs exposure time). Total crack length was determined from a single frame of the video that showed the entire crack trajectory.

To examine the microstructure of the crack plane, rectangular prism-shaped specimens were cut about 2 mm below the fracture surface with a low-speed diamond saw and parallel to the long axis of the bone. The fracture fragments were soaked in ethanol, dehydrated, and coated with gold/palladium before SEM imaging at 5kV (Mira 3, Tescan, Czech Republic). Osteon density (number of osteons per 1x1 mm^2) was calculated from the SEM images.

To allow consideration of fatigue behavior, we include fatigue data from specimens previously reported by Brock and colleagues that were harvested from the same animals.[12] In those experiments, rectangular beams (2 x 2 x 25 mm beams, n = 6/group) were cycled between 400 and 4000 $\mu\varepsilon$ under load control until failure. During testing samples were hydrated with hydroxyapatite-buffered PBS at 37 ˚C. Fatigue life, determined by Brock and colleagues, was included to correlate with fracture toughness, whole bone bending strength and tissue nanomehcanics and compositions in the current study.

2.2.3 Nanoscale tissue characterization

A 15-mm thick segment was removed from the mid-diaphysis of the right femur. The segment was dehydrated in ethanol and embedded in polymethyl methacrylate (PMMA). A 3-mm slice was cut from the embedded segment. The slice was polished anhydrously to a final root-mean-square surface roughness less than 15 nm over a 5 x 5 μm^2 scan, as verified using atomic force microscopy (Dimension 3100, Veeco Metrology Group).[24] Three osteons per sample and three radial lines per osteon were chosen for tissue-property characterization by nanoindentation, Raman spectroscopy, and second harmonic generation microscopy (SHG).[15] To reduce variations caused by anatomical location, osteons were selected from the postero-lateral quadrant.

Nanoindentation was used to characterize tissue nanomechanical properties.[27] A 20 x 20 μm^2 surface topography scan was acquired prior to indentation to accurately identify the center of each lamella. Indentations were made (TriboIndenter, Hyistron Inc., Minneapolis, MN) with a Berkovich diamond indenter in the middle of each lamella, moving away from the center of each osteon. Three osteons were selected, resulting in 45-135 indentations per animal. Indentation loading occurred at a rate of 50 μN/s, a 10-second hold at 700 μN, and unloading at 50 μN/s. The resulting indentations were ~150 nm deep. The indentation modulus and hardness were calculated from the unloading part of the load-displacement curve following Rho *et al.*.[28]

Tissue composition was characterized by Raman spectroscopy. As described previously, data were collected at the same mid-lamellar locations probed by nanoindentation.[15] The white light optical microscope attached to the Raman

spectroscope (InVia microRaman, Renishaw, Gloucestershire, United Kingdom) was used to identify the residual indents and center the laser spot (~2 μm^2) over each residual indent. Spectra were collected between 800 and 1800 cm^{-1} with background fluorescence removed using WiRE™ V4.0 software (Renishaw). Tissue mineralization (mineral:matrix), B-type carbonate substitution (carbonate:phosphate), and crystallinity were calculated as described previously.[15]

Aligned collagen content associated with tissue stiffness was determined by SHG (Mai Tai Deep See, Spectra Physics, Santa Clara, CA).[29] A map of aligned collagen content within each osteon was created. The square root of SHG intensity is proportional to the aligned collagen within the transverse plane.[30] SHG intensity was averaged for a window 1 pixel wide and 4 pixels high (497 x 1988 nm^2, Image J, National Institutes of Health) along a radial line from the center of each osteon. For each lamella, maxima corresponded to lamellar aligned collagen and minima corresponded to interlamellar aligned collagen.[15] Peak height ratio, representing the variation in the amount of aligned collagen and a measure of inhomogeneity, was calculated as the ratio of the intensity of lamellar-to-interlamellar aligned collagen.

2.2.4 Whole bone strength and geometry

Computed tomography (135 kV, 260 mAs, Toshiba Aquilion LB) was used to quantify whole bone geometry. CT images of the left femurs (n = 6-7/group) were collected before conducting four-point bending. Scans of a 3-cm thick segment of the mid-diaphysis were used to calculate the moment of inertia about the caudal-cranial

direction as described previously.[31]

Whole-bone mechanical behavior of the left femur was determined by four-point bending to failure in the caudal-cranial direction (858 Mini Bionix, MTS; 5mm/min loading rate; 13 cm upper span width; 22 cm lower span width). Bending stiffness and whole bone bending strength were calculated from the load-displacement data.

2.2.5 Data analysis

Analysis was performed on the raw, unaveraged data from all data sets (JMP 11.0, SAS Institute, INC.). Repeated nested ANOVA determined the effects of treatment and tissue age on cortical tissue properties from nanoindentation, Raman and SHG. Generalized linear models with treatment (PTH or Vehicle), osteon (1-3, nested variable), radial line (1-3, nested variable), and distance from the center of the osteon (0-70μm) were used. In addition, data were binned in 7 μm increments across the radius in three randomly-selected osteons per animal to visualize tissue age data.

The effects of PTH treatment on the micro- and whole-bone (fracture toughness, osteon density, total crack length, moment of inertia, bending strength, bending stiffness) outcome measures were analyzed by Student's *t*-test. A *p*-value less than 0.05 was considered significant. Group difference presented are significant unless noted otherwise. To determine the contributions of compositional variations to alterations in tissue properties and correlations between strength, fracture toughness and fatigue life, multi-variable regression analysis was performed with averaged

values from each data set.

2.3 Results

The average weight of the sheep in the PTH treatment group was 28 lb lower than the Vehicle group at 24 months (Table 2.1). BV/TV, TMD and Ct.Th of cortical bone from the iliac crest were not different between treatment groups (Table 2.1). Serum PTH levels were 0.26 pg/ml greater in the PTH group compared to Vehicle at 24 months. Serum CTx levels were slightly greater by 34.4% with PTH treatment relative to Vehicle ($p < 0.1$). Serum levels of calcium, and BAP and ALP levels were not different between the two groups (Table 2.1).

Table 2.1 *Reductions in body weight were present in the PTH-treated group before treatment started and remained at the end of treatment. Serum PTH at 24 months was higher in the PTH treatment group. Changes in serum CTx had a trend towards increasing with PTH treatment.*
*Data shown as mean (SD). *p < 0.05. **p < 0.1*

	Baseline (0 mo.)		1 year after ovariectomy (13 mo.)		1 year after treatment (24 mo.)	
	Vehicle	**PTH**	**Vehicle**	**PTH**	**Vehicle**	**PTH**
Sheep characteristics						
Body mass (lb)	163 (7.7)	165 (8.3)	186 (8.0)	166 (12)*	186 (11)	158 (20)*
Serum markers						
Calcium (mmol/L)	1.1 (0.07)	1.0 (0.04)	0.74 (0.27)	0.89 (0.27)	1.2 (0.11)	1.1 (0.05)
BAP (U/L)	34 (15)	25 (10)	43 (34)	44 (25)	35 (15)	23 (9.3)
CTx (ng/mL)	0.56 (0.3)	0.59 (0.2)	0.41 (0.2)	0.64 (0.5)**	0.18 (0.1)	0.86 (1.6)**
ALP (U/L)	80 (54)	46 (26)	54 (29)	52 (32)	110 (51)	62 (34)
PTH (pmol/L)	0.05 (0.12)	0.03 (0.08)	0.22 (0.17)	0.11 (0.15)	0.05 (0.12)	0.31 (0.18)*
Iliac crest structure						
Cortical BV/TV	Not applicable		0.79 (0.09)	0.78 (0.08)	0.76 (0.18)	0.82 (0.06)
Cortical TMD (mg/cm^3)			714 (19)	730 (40)	698 (35)	725 (43)
Ct.Th (μm)			272 (73)	260 (62)	275 (61)	312 (82)

The effect of PTH treatment on the femur was apparent at the micro- and nanoscale (Table 2.2). Fracture toughness was 22.4% lower in the PTH-treated sheep. Osteon density was 120% greater in the PTH group (Figure 2.1). Total crack length was not different between groups. Tissue indentation modulus was 4.3% lower in the PTH-treated group (Figure 2.2). Hardness was 10.8% less on average with PTH treatment (Figure 2.2). Hardness and indentation modulus did not vary with tissue age within osteons (Figure 2.2).

Table 2.2 *PTH treatment reduced indentation modulus, hardness, and carbonate substitution. Mineral-to-matrix ratio and peak height ratio were increased with PTH treatment, which also increased with tissue age. In addition to nano-scale tissue properties, fracture toughness was decreased and osteon density was increased with PTH treatment compared to Vehicle group. Data shown as mean (SD). *p < 0.05. NS = not significant. NA = not applicable*

	Treatment effect	
	Vehicle	**PTH**
Tissue nanomechanics		
Indentation Modulus (GPa)	28.0 (4.6)	26.8 (3.6)*
Hardness (MPa)	992 (200)	885 (150)*
Tissue composition		
Mineral : matrix	6.83 (0.70)	7.38 (0.84)*
Carbonate : phosphate	0.213 (0.01)	0.209 (0.01)*
Crystallinity	0.038 (0.001)	0.038 (0.001)
Aligned collagen content	1.79 (0.62)	2.38 (0.96)*
Cortex properties		
Fracture toughness (MPa$\sqrt{m}$)	6.24 (0.81)	4.82 (1.3)*
Osteon density (#/mm^2)	12.5 (5.3)	27.4 (11)*
Total crack length (pixels)	63.2 (11)	58.3 (9.0)
Diaphyseal moment of inertia (cm^4)	1.70 (0.58)	2.11 (1.1)
Whole bone bending stiffness (N-m^2)	91.7 (17)	110 (19)
Whole bone bending strength (N-m)	145 (24)	162 (40)

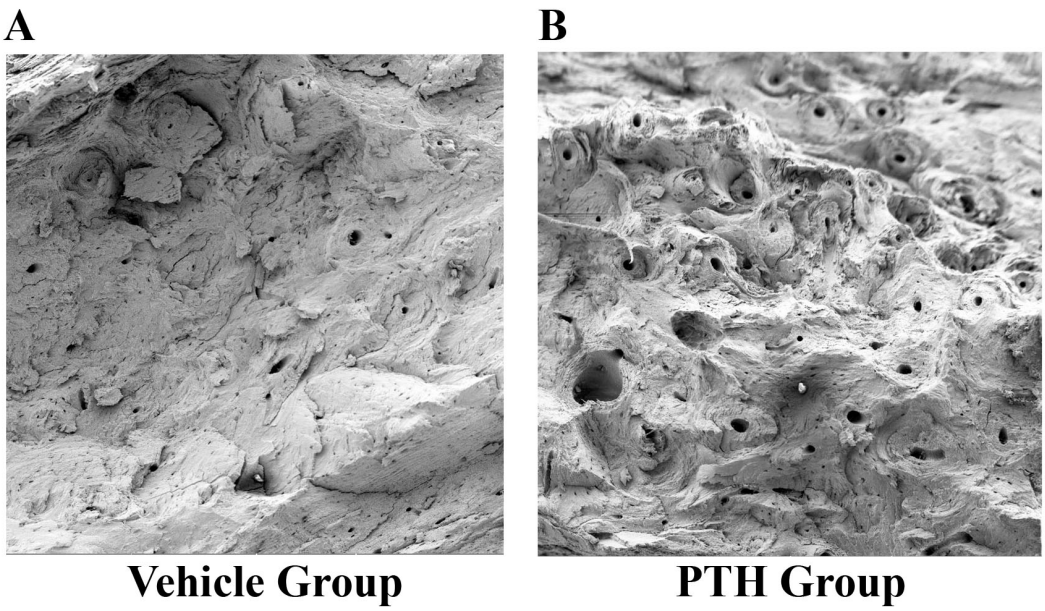

Figure 2.1 *Osteon density was increased with PTH treatment as shown in SEM images (A) Vehicle group (B) PTH group. Field of view 1 x 1 mm*^{2}.

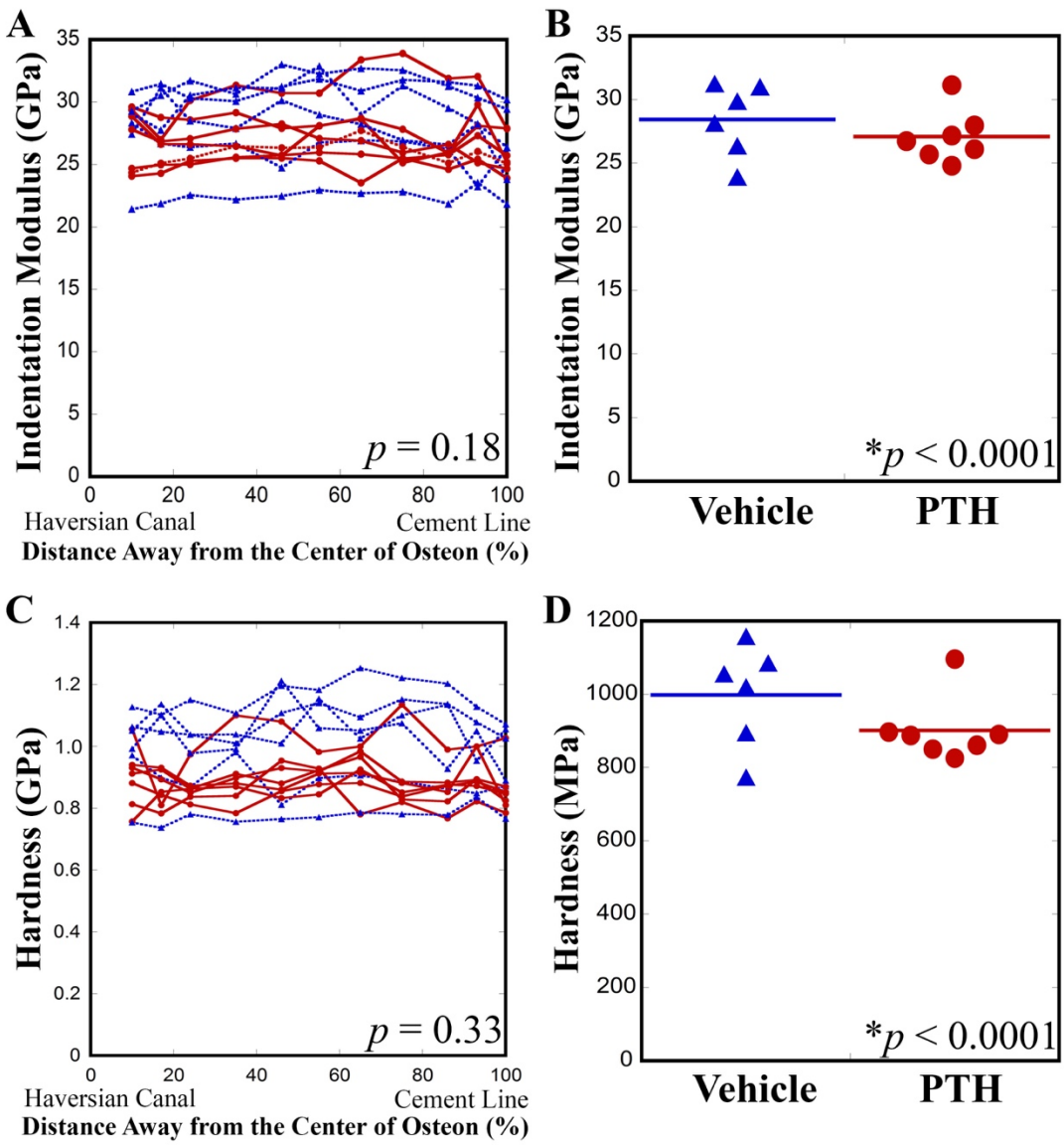

Figure 2.2 *Nanomechanical properties (indentation modulus and hardness) decreased with PTH treatment but not tissue age. (A) Indentation modulus (p = 0.18) and (C) hardness (p = 0.33) versus tissue age. Percent distance away from the center of osteon represents older tissue age. (B) Indentation modulus (p < 0.0001) and (D) hardness (p < 0.0001) with vehicle/PTH treatment. Each point in (B) and (D) is the average value of multiple nanoindentation measurements of per sheep (45-135 measurements per animal). Red circles with solid lines represent PTH group and blue triangles with dashed lines represent Vehicle group.*

Mineral-to-matrix ratio in the osteons was influenced by both treatment and tissue age (Figure 2.3). Mineral-to-matrix ratio was 8.1% greater in PTH-treated animals, and for a total increase of 4.8–9.6% across the osteon radii. The carbonate-to-phosphate ratio in osteons also was reduced in PTH-treated animals (Figure 2.3). Crystallinity did not vary within the osteon with either PTH-treatment or tissue age (Figure 2.3). Aligned collagen content varied with treatment and tissue age (Figure 2.4). The peak height ratio of lamellar-to-interlamellar aligned collagen increased by 24.8% in PTH-treated animals, and for a total increase of 5.7–11.4% across the osteon radii.

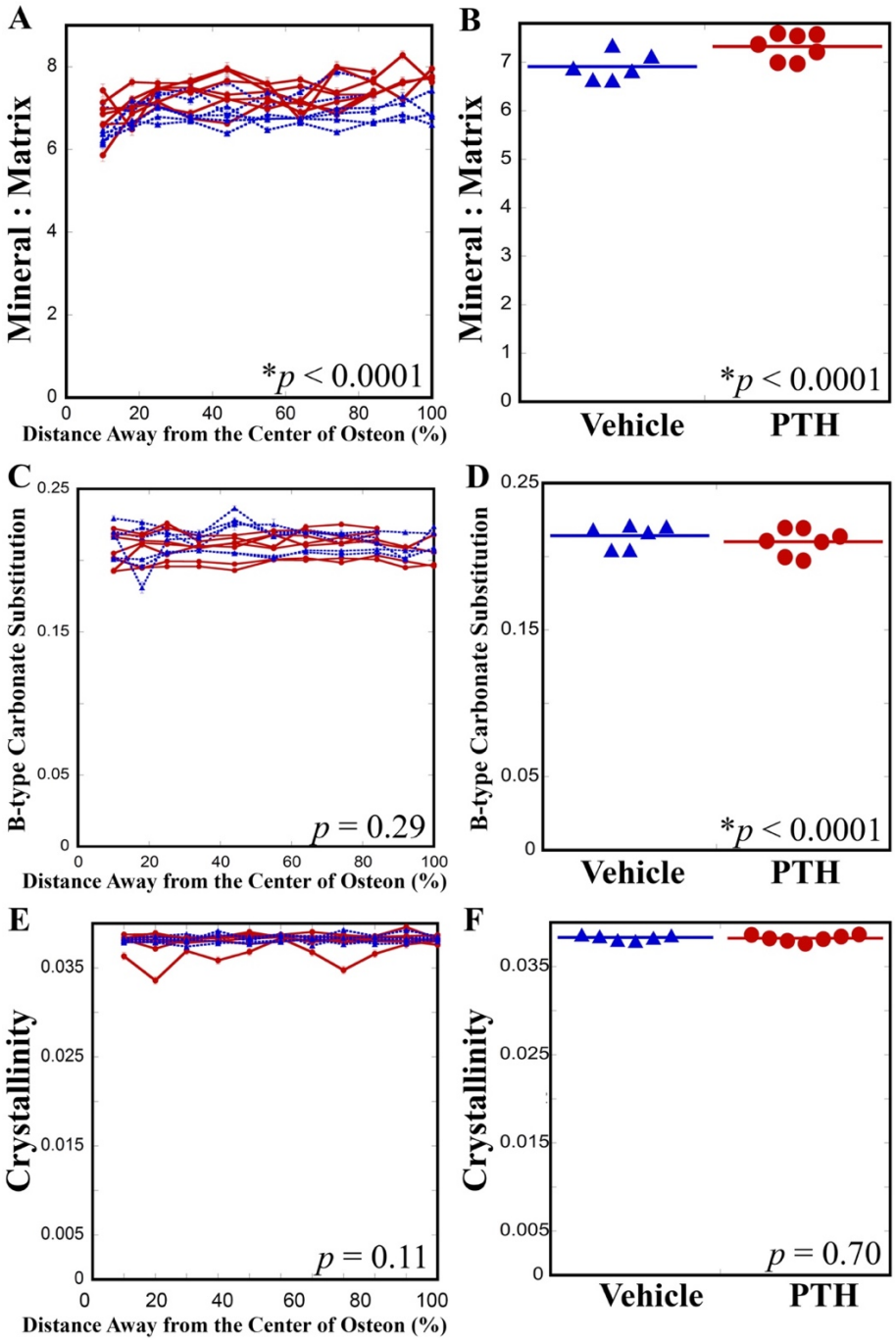

Figure 2.3 *Mineral-to-matrix ratio increased with tissue age and PTH treatment while carbonate substitution decreased with PTH treatment. (A) Mineral-to-matrix ratio ($p < 0.0001$), (C) carbonate substitution ($p = 0.29$) and (E) crystallinity ($p = 0.11$) versus tissue age. Percent distance away from the center of osteon represents older tissue age. (B) Mineral-to-matrix ratio ($p < 0.0001$), (D) carbonate substitution ($p < 0.0001$) and (F) crystallinity ($p = 0.70$) with vehicle/PTH treatment. Each point in (B), (D), (F) is the*

average value of multiple Raman measurements for a single sheep (5-15 indents per line, 3 lines for 3 osteons per sample, corresponding 45-135 measurements per animal). Red circles with solid lines represent PTH group and blue triangles with dashed lines represent Vehicle group.

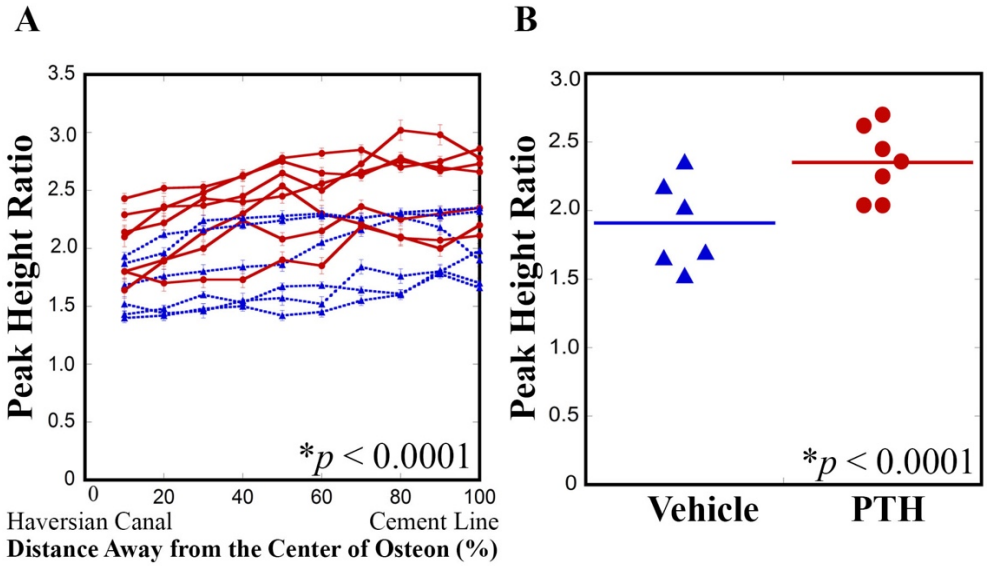

Figure 2.4 *The degree of aligned collagen (peak height ratio) increased with tissue age but increased with PTH treatment. (A) Peak height ratio (lamellar/interlamellar aligned collagen, $p < 0.0001$) versus tissue age. Percent distance away from the center of osteon represents older tissue age. (B) peak height ratio ($p < 0.0001$) with vehicle/PTH treatment. Each point in (B) is the average value of multiple SHG measurements for a single sheep (45-135 measurements per animal). Red circles with solid lines represent PTH group and blue triangles with dashed lines represent Vehicle group.*

Whole bone structure and mechanical performance were not influenced by PTH treatment. Moment of inertia, whole bone bending stiffness and strength did not differ between PTH and vehicle groups. Whole bone bending strength was correlated with bending stiffness ($r^2 = 0.32$).

Correlations among three mechanical failure properties (whole bone bending strength, fatigue life, fracture toughness), compositional properties from Raman

spectroscopy, and nanomechanical properties from nanoindentation were present (Table 2.3, Figure 2.5). At the nanoscale, mineralization (mineral-to-matrix ratio) explained 85% of the variation in aligned collagen content. However, carbonate substitution and crystallinity were not correlated with nanoindentation properties. Neither indentation modulus nor hardness was correlated with mineral-to-matrix ratio. For correlations of tissue composition with micro- and macro-scale mechanical properties, mineralization explained 35% of the variation in fracture toughness and 27% of the variation in fatigue life (Figure 2.6). Crystallinity explained 60% of the variation in whole bone bending strength. Whole bone bending strength was correlated with fracture toughness ($r^2 = 0.32$). Together, 63% of the variation in whole bone bending strength was explained by crystallinity and fracture toughness. Fatigue life was not correlated with either whole bone bending strength or fracture toughness.

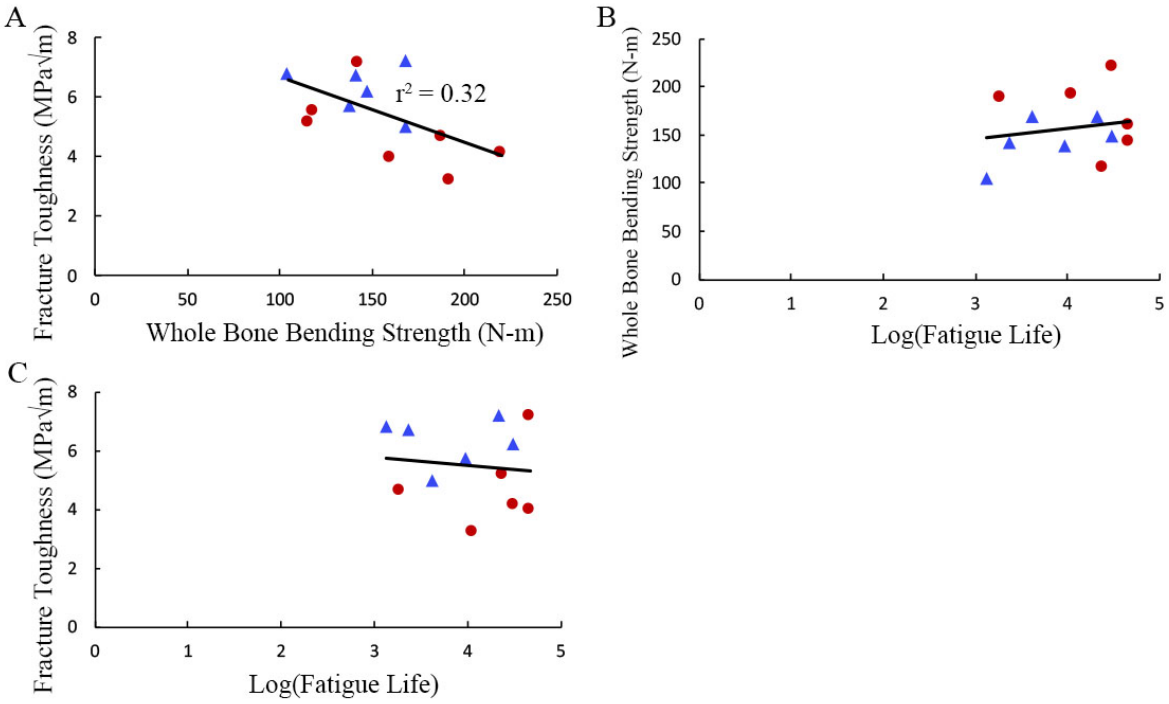

Figure 2.5 *Correlations among three interdependent mechanical failure properties: whole bone bending strength, fracture toughness, and fatigue life. Fracture toughness was associated with bending strength ($r^2 = 0.32$, $P < 0.05$). Fatigue life, however, did not correlate with either fracture toughness or bending strength. Red circles represent PTH group and blue triangles represent Vehicle group.*

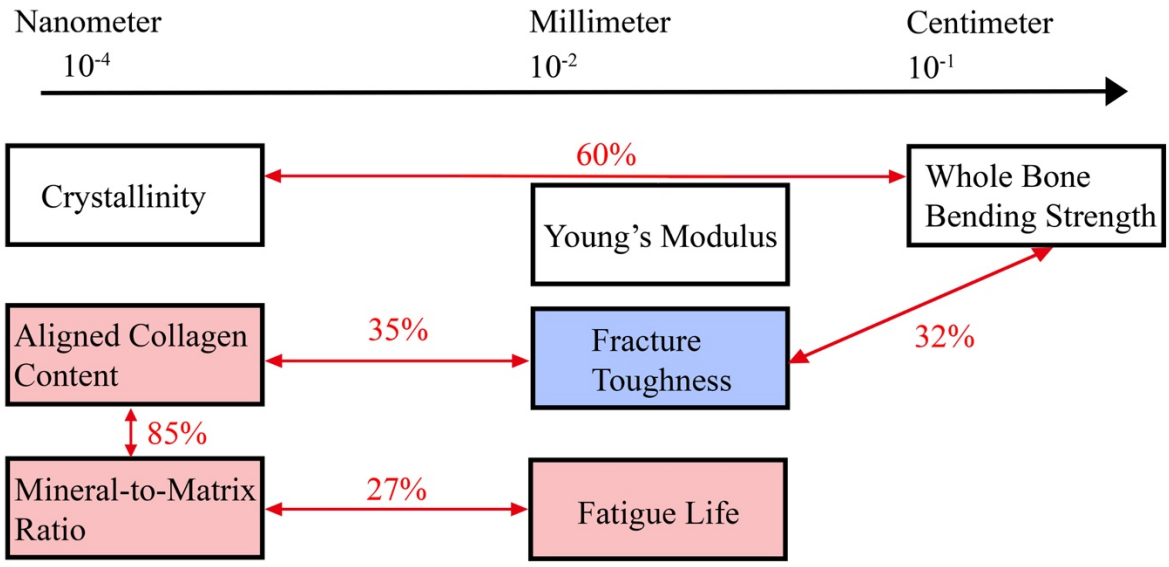

Figure 2.6 *Alterations in tissue composition contributed to tissue properties that describe bone failure. Red/blue background indicated properties increased/decreased with PTH treatment.*

Table 2.3 *Crystallinity and fracture toughness explained 60% and 32% of the variations in whole bone bending strength respectively. Together, crystallinity and fracture toughness explained 63% of the variation in whole bone bending strength. *$p < 0.05$. **$p < 0.1$. (r^2 of the correlations < 0.25 was not reported)*

Predictor	Independent variables	r^2
Whole bone bending strength	Crystallinity	0.60*
Fatigue life	Mineralization	0.27**
Fracture toughness	Mineralization	0.35*
Mineralization	Aligned collagen content	0.85*
Whole bone bending strength	Fracture toughness	0.32*
Whole bone bending stiffness	Fracture toughness	0.56*
Whole bone bending strength	Crystallinity + Fracture toughness	0.63*
Fracture toughness	Mineralization + Whole bone bending strength	0.54*
Fracture toughness	Mineralization + Whole bone bending stiffness	0.67*

2.4 Discussion

We hypothesized that PTH would alter tissue composition, and improve tissue mechanical properties and whole bone strength in this large animal model of osteoporosis. PTH treatment improved micro- and nano-scale mechanical properties. However, the effects of PTH treatment were not evident in macro-scale geometry or whole bone strength of the femur.

Despite the fact that whole bone strength was not altered by PTH treatment, bone tissue mechanical properties were altered. Fracture toughness was decreased with PTH treatment. Although fracture toughness correlated with whole bone bending strength, the changes in fracture toughness were not evident at the whole bone level through differences in bending strength. Mechanical failure of a whole bone may occur from a single load, which is sensitive to whole bone strength, from cyclic loading that is sensitive to fatigue behavior, or from sensitivity to crack growth, reflected by fracture toughness.[5] The altered tissue properties measured here reflected alterations in fatigue life and fracture toughness, which would cause mechanical failure independent of whole bone strength changes. The three mechanical properties are often investigated independently, but are correlated with each other as all describe failure of molecular bonds. To date studies have not closely examined the correlation of these distinct mechanical properties in bone.

Fatigue life is the resistance to many cycles of low- to moderate-magnitude loading whereas fracture toughness represents the energy needed to propagate a single pre-existing crack, a mechanism that contributes to both monotonic and cyclic strength

behavior. Previously, we showed increased fatigue life of cortical bone associated with PTH treatment compared to control and bisphosphonate-treated tissue.[12] Our data suggest that the increased fatigue life might be associated with increased tissue mineralization as measured by Raman spectroscopy ($r^2 = 0.27$, $p = 0.08$). Decreased fracture toughness was also correlated with increased tissue mineralization ($r^2 = 0.35$, $p < 0.05$). Crystallinity explained 60% of the variation in whole bone bending strength (Figure 2.6). This correlation was consistent with previous literatures: crystallinity has shown to be correlated with Young's modulus at microscale;[32] moreover, Young's modulus has shown to be correlated with whole bone strength at macroscale.[33] Furthermore, crystallinity and fracture toughness explained 63% of the variations in whole bone bending strength. This correlation showed that fracture toughness not only independently contributed to bone failure, but also contributed to bending strength to some degree; hence, two of the three distinct material properties that describe bone failure were related to each other in the present study (Figure 2.6).

Fatigue life, on the other hand, was not correlated with either fracture toughness or strength (Figure 2.5). Measurements from fatigue testing were sensitive to local microstructural details. In bone, cement line and other heterogeneities may limit the propagation of small cracks initiated by fatigue loading, resulting more variations in fatigue life. Fracture toughness and strength, on the other hand, are less dependent on random flaws or tissue heterogeneity. Due to the larger variations in fatigue behavior and small sample size, important correlations between whole-bone strength, fracture toughness and fatigue properties were not detected.

We attributed differences in tissue fracture toughness in PTH-treated bone

primarily to changes in osteon number and geometry. Clinically and in animal models,[34,35] PTH elevates the turnover rate; thereby increasing the number of osteons (Figure 2.1). Fracture toughness has been positively correlated with larger numbers of small osteons;[19] however, although PTH increased osteon density, the size of the osteons and Haversian canals were larger in the PTH-treated group. Larger osteons contribute to larger osteonal area (including Haversian canals), resulting increased porosity which negatively correlates to fracture toughness.[19] Therefore, we attribute the reduction in fracture toughness to larger Haversian canals and associated porosity from increased turnover in the PTH-treated group.

The mineral-to-matrix ratio in the osteons increased with tissue age and was elevated in the PTH-treated group whereas both indentation modulus and hardness were not different with tissue age and were decreased with PTH treatment. Mineralization is known to increase with tissue age,[36,37] consistent with our findings. However, the elevated mineralization with PTH treatment was not consistent with previous studies. Clinically, PTH treatment decreased mineralization and crystallinity measured by FTIR in osteoporotic patients.[38] Mineralization showed positive relationship with indentation modulus and hardness.[15] The absence of the positive relationship in our study might be resulted from the narrower range of indentation modulus and mineralization. In bamboo models,[15] indentation modulus ranged from 24-38 GPa and mineralization was from 5-10 whereas in the present study, indentation modulus ranged from 24-31 GPa and mineralization was from 6-8, demonstrating the negative relationship with mineralization. If more measurements across the entire cortex were obtained, positive relationship between indentation modulus and

mineralization would be captured. Moreover, we did not see a relationship between nanoindentation parameters and tissue age. A limitation of our tissue age data is our inability to know whether the specific osteons examined were recently formed or fully mineralized at the time of analysis. Alternatively, we might not have characterized the newly-formed bone tissue. We labeled our animals with tetracycline but did not measure turnover rate due to technical errors in dosage of formation markers. We do not know whether turnover in the femur increased with PTH treatment.

Combined OVX and MA diet was selected to produce extreme osteopenia, which is an appropriate model for post-menopausal osteoporosis. In the sheep, OVX induces increased bone resorption for six months, which was indicative of a high bone turnover rate and leads to bone loss in the vertebrae.[39] In sheep, dietary-induced MA reduced bone mineral density compared to sham surgery.[40] After 12 months, BMD in ovariectomized sheep in our study was consistent with other studies (data not shown).[41]

As in any experiment, certain limitations exist. We chose to use the femur for these analyses, as the femur is the most appropriate site for whole bone mechanical tests. However, reviewing the literature we found reports that ovariectomized sheep of comparable age to ours showed less loss of BMD in the femur than at other skeletal sites.[42,43] Bone volume fraction changed before and after PTH treatment in the spine, which are dominantly consisted of cancellous bone, of our animals (data not shown). The spine could have macroscopic and nanoscale differences with PTH treatment. Another consideration is the optimum dosage, duration, and frequency of the PTH treatment. We used the dose recommended for sheep.[44] The absence of hypercalcemia

which resulted from over-dose of PTH treatment[45] in the sheep indicates the PTH dosage was appropriate. Previously, a monkey model was also treated with teriparatide (1-34) 5μg/kg/day for 12 months.[46] In the clinical trial, patients were subcutaneously injected with parathyroid hormone (1-34) 20 or 40 μg daily for 21 months.[47] However, the effective treatment time period for sheep are unknown and one year of treatment may not be sufficient to observe an effect. In the present study, most serum measures (CTx, BAP, ALP, and Ca) demonstrated maximum changes at 20 rather than 24 months, suggesting that by 24 months, whole body markers of bone turnover might return to steady state. Furthermore, because few tetracycline double labels were apparent, new bone formation at the end of the experiment appeared to be minimal compared to other ovariectomized models.

Finally, we did not include sham-operated animals. In the present study, a sham-operated group might demonstrate whether bone loss from ovariectomized and metabolic acidosis was sufficient in the Vehicle group. Additionally, a drug holiday, stopping the treatment for a period of time, or combining different categories of treatment, could also be considered.[48] Monkey models with PTH treatment for 12 months followed by 6 months withdrawal still preserved the strength increase at the proximal femur compared to the OVX group; and the strength was not different from 18 months continuous treatment.[46] Rodent models treated with PTH for the first 8 weeks followed by bisphosphonate for 8 weeks prevented the decrease in mechanical strength that occurred after an 8-week PTH-withdrawal.[49]

In summary, few studies have examined the alteration of tissue mechanical and compositional properties after PTH treatment using animal models with Haversian

remodeling.[12,14] The significance of this study was to evaluate treatment and tissue age effects on mechanical properties and composition across different length-scales, from macro- to nano-scale. In addition, this study is the first to correlate all three tissue properties, whole bone strength, fracture toughness and fatigue behavior, that describe mechanical failure of bone together. We saw differences in the nanoscale composition and tissue mechanical properties with PTH treatment. Although we did not see variations in whole bone strength between treatment groups, alterations in tissue properties with PTH were critical contributors to fatigue properties and fracture toughness (crack propagation resistance). For example, whole bone bending strength can be explained by tissue composition and fracture toughness. In addition to the effects of PTH treatment on cortical bone in the current study, several studies have shown a response at cancellous sites,[47,50] the alteration of mechanical and material properties in the cancellous bone is under investigation.

References

1. Kannus P. International osteoporosis foundation: The facts about osteoporosis and its impact. International Osteoporosis Foundation; 2003.

2. Lindsay R, Silverman SL, Cooper C, et al. Risk of new vertebral fracture in the year following a fracture. Journal of the American Medical Association. 2001;285(3):320-3.

3. Kanis JA, Borgstrom F, De Laet C, et al. Assessment of fracture risk. Osteoporosis International. 2005;16(6):581-9.

4. Donnelly E. Methods for assessing bone quality: a review. Clinical Orthopaedics and Related Research®. 2011;469(8):2128-38.

5. Hernandez C, van der Meulen M. Understanding Bone Strength Is not Enough. Journal of Bone and Mineral Research. 2017.

6. Hernandez CJ, van der Meulen MC. Understanding Bone Strength Is Not Enough. Journal of Bone and Mineral Research. 2017.

7. Lloyd AA, Gludovatz B, Riedel C, et al. Atypical fracture with long-term bisphosphonate therapy is associated with altered cortical composition and reduced fracture resistance. Proceedings of the National Academy of Sciences. 2017:201704460.

8. Shane E, Burr D, Ebeling PR, et al. Atypical subtrochanteric and diaphyseal femoral fractures: report of a task force of the American Society for Bone and Mineral Research. Journal of Bone and Mineral Research. 2010;25(11):2267-94.

9. Schilcher J, Sandberg O, Isaksson H, Aspenberg P. Histology of 8 atypical femoral fractures: remodeling but no healing. Acta orthopaedica. 2014;85(3):280-6.

10. Imbert L, Boskey A. Effects of Drugs on Bone Quality. Clinical Reviews in Bone and Mineral Metabolism. 2016;14(3):167-96.

11. Jilka RL, Weinstein RS, Bellido T, Roberson P, Parfitt AM, Manolagas SC. Increased bone formation by prevention of osteoblast apoptosis with parathyroid hormone. Journal of Clinical Investigation. 1999;104(4):439-46.

12. Brock GR, Chen JT, Ingraffea AR, et al. The effect of osteoporosis treatments on fatigue properties of cortical bone tissue. Bone Reports. 2015;2:8-13.

13. Oxlund H, Ejersted C, Andreassen T, Tørring O, Nilsson M. Parathyroid hormone (1-34) and (1-84) stimulate cortical bone formation both from periosteum and endosteum. Calcified tissue international. 1993;53(6):394-9.

14. Fox J, Miller M, Newman M, Recker R, Turner C, Smith S. Effects of daily treatment with parathyroid hormone 1–84 for 16 months on density, architecture and biomechanical properties of cortical bone in adult ovariectomized rhesus monkeys. Bone. 2007;41(3):321-30.

15. Burket J, Gourion-Arsiquaud S, Havill LM, Baker SP, Boskey AL, Van der Meulen MC. Microstructure and nanomechanical properties in osteons relate to tissue and animal age. Journal of Biomechanics. 2011;44(2):277-84.

16. Gourion-Arsiquaud S, Burket JC, Havill LM, et al. Spatial variation in osteonal bone properties relative to tissue and animal age. Journal of Bone and Mineral Research. 2009;24(7):1271-81.

17. Fratzl P. Hierarchical structure and mechanical adaptation of biological materials. Learning From Nature How to Design New Implantable Biomaterials: From Biomineralization Fundamentals to Biomimetic Materials and Processing Routes,(NATO Science Series II: Mathematics, Physics and Chemistry Vol 171), RL Reis and S Weiner, eds, Kluwer Academic Publishers, Amsterdam. 2004:15-34.

18. Rho JY, Zioupos P, Currey JD, Pharr GM. Microstructural elasticity and regional heterogeneity in human femoral bone of various ages examined by nano-indentation. Journal of biomechanics. 2002;35(2):189-98.

19. Yeni Y, Brown C, Wang Z, Norman T. The influence of bone morphology on fracture toughness of the human femur and tibia. Bone. 1997;21(5):453-9.

20. Yeni YN, Norman TL. Calculation of porosity and osteonal cement line effects

on the effective fracture toughness of cortical bone in longitudinal crack growth. Journal of Biomedical Materials Research Part A. 2000;51(3):504-9.

21. Turner A. The sheep as a model for osteoporosis in humans. The Veterinary Journal. 2002;163(3):232-9.

22. Burket JC, Brooks DJ, MacLeay JM, Baker SP, Boskey AL, van der Meulen MC. Variations in nanomechanical properties and tissue composition within trabeculae from an ovine model of osteoporosis and treatment. Bone. 2013;52(1):326-36.

23. Arens D, Sigrist I, Alini M, Schawalder P, Schneider E, Egermann M. Seasonal changes in bone metabolism in sheep. The Veterinary Journal. 2007;174(3):585-91.

24. Donnelly E, Baker SP, Boskey AL, van der Meulen MC. Effects of surface roughness and maximum load on the mechanical properties of cancellous bone measured by nanoindentation. Journal of Biomedical Materials Research. 2006;77(2):426-35.

25. Brock GR, Kim G, Ingraffea AR, Andrews JC, Pianetta P, van der Meulen MC. Nanoscale examination of microdamage in sheep cortical bone using synchrotron radiation transmission x-ray microscopy. PloS One. 2013;8(3):e57942.

26. Standard A. E399-90. Standard Test Method for Plane-Strain Fracture Toughness of Metallic Materials1, Annual Book of ASTM Standards. 2002;3.

27. Donnelly E, Boskey AL, Baker SP, Van der Meulen MC. Effects of tissue age on bone tissue material composition and nanomechanical properties in the rat cortex. Journal of Biomedical Materials Research. 2010;92(3):1048-56.

28. Rho JY, Tsui TY, Pharr GM. Elastic properties of human cortical and trabecular lamellar bone measured by nanoindentation. Biomaterials. 1997;18(20):1325-30.

29. Boyd RW. Nonlinear optics: Academic press; 2003.

30. Zipfel WR, Williams RM, Webb WW. Nonlinear magic: multiphoton microscopy in the biosciences. Nature biotechnology. 2003;21(11):1369-77.

31. Kim G, Boskey AL, Baker SP, van der Meulen MC. Improved prediction of rat cortical bone mechanical behavior using composite beam theory to integrate tissue level properties. Journal of biomechanics. 2012;45(16):2784-90.

32. Yerramshetty JS, Akkus O. The associations between mineral crystallinity and the mechanical properties of human cortical bone. Bone. 2008;42(3):476-82.

33. Hernandez C, Beaupre G, Keller T, Carter D. The influence of bone volume fraction and ash fraction on bone strength and modulus. Bone. 2001;29(1):74-8.

34. Garnero P, Sornay-Rendu E, Chapuy MC, Delmas PD. Increased bone turnover in late postmenopausal women is a major determinant of osteoporosis. Journal of Bone and Mineral Research. 1996;11(3):337-49.

35. Hirano T, Burr DB, Turner CH, Sato M, Cain RL, Hock JM. Anabolic effects of human biosynthetic parathyroid hormone fragment (1–34), LY333334, on remodeling and mechanical properties of cortical bone in rabbits. Journal of bone and Mineral Research. 1999;14(4):536-45.

36. Paschalis E, DiCarlo E, Betts F, Sherman P, Mendelsohn R, Boskey A. FTIR microspectroscopic analysis of human osteonal bone. Calcified Tissue International. 1996;59(6):480-7.

37. Boskey AL, Coleman R. Aging and bone. Journal of Dental Research. 2010;89(12):1333-48.

38. Paschalis EP, Glass EV, Donley DW, Eriksen EF. Bone mineral and collagen quality in iliac crest biopsies of patients given teriparatide: new results from the fracture prevention trial. Journal of Clinical Endocrinology & Metabolism. 2005;90(8):4644-9.

39. Pastoureau P, Arlot M, Caulin F, Barlet J, Meunier P, Delmas P. Effects of oophorectomy on biochemical and histological indices of bone turnover in ewes. Journal of Bone and Mineral Research. 1989;4(Suppl 1):58.

40. MacLeay J, Olson J, Enns R, et al. Dietary-induced metabolic acidosis decreases bone mineral density in mature ovariectomized ewes. Calcified tissue international. 2004;75(5):431-7.

41. Wu Z-x, Lei W, Hu Y-y, et al. Effect of ovariectomy on BMD, micro-architecture and biomechanics of cortical and cancellous bones in a sheep model. Medical engineering & physics. 2008;30(9):1112-8.

42. Pogoda P, Egermann M, Schnell JC, et al. Leptin inhibits bone formation not only in rodents, but also in sheep. Journal of Bone and Mineral Research. 2006;21(10):1591-9.

43. Giavaresi G, Fini M, Martini L, et al. Histomorphometric characterization of cancellous and cortical bone in an ovariectomized sheep model. Journal of Applied Animal Research. 2001;20(2):221-32.

44. Delmas PD, Vergnaud P, Arlot ME, Pastoureau P, Meunier PJ, Nilssen M. The anabolic effect of human PTH (1–34) on bone formation is blunted when bone resorption is inhibited by the bisphosphonate tiludronate—is activated resorption a prerequisite for the in vivo effect of PTH on formation in a remodeling system? Bone. 1995;16(6):603-10.

45. Tashjian AH, Gagel RF. Teriparatide [Human PTH (1-34)]: 2.5 Years of Experience on the Use and Safety of the Drug for the Treatment of Osteoporosis. Journal of Bone and Mineral Research. 2006;21(3):354-65.

46. Sato M, Westmore M, Ma YL, et al. Teriparatide [PTH (1–34)] strengthens the proximal femur of ovariectomized nonhuman primates despite increasing porosity. Journal of Bone and Mineral Research. 2004;19(4):623-9.

47. Neer RM, Arnaud CD, Zanchetta JR, et al. Effect of parathyroid hormone (1-34) on fractures and bone mineral density in postmenopausal women with osteoporosis. New England journal of medicine. 2001;344(19):1434-41.

48. Anagnostis P, Paschou S, Mintziori G, Lambrinoudaki I, Goulis D. Bisphosphonate and denosumab “holiday” in postmenopausal osteoporosis: A systematic review of randomized-controlled trials. Maturitas. 2017;100:140.

49. Ejersted C, Oxlund H, Andreassen T. Bisphosphonate maintains parathyroid

hormone (1-34)-induced cortical bone mass and mechanical strength in old rats. Calcified tissue international. 1998;62(4):316-22.

50. Jerome C, Burr D, Van Bibber T, Hock J, Brommage R. Treatment with human parathyroid hormone (1-34) for 18 months increases cancellous bone volume and improves trabecular architecture in ovariectomized cynomolgus monkeys (Macaca fascicularis). Bone. 2001;28(2):150-9.

CHAPTER 3

PARATHYROID HORMONE (PTH) IMPROVES BONE HETEROGENEITY AND PRESERVES MECHANICAL PROPERTIES OF CANCELLOUS BONE BEFORE FATIGUE FAILURE IN A SHEEP MODEL OF OSTEOPOROSIS*

3.1 Introduction

Osteoporosis is a multifaceted condition characterized by loss of bone quantity and a deterioration of bone tissue quality, both contributing to fragility fractures. Typical osteoporotic fractures, at the hip for example, are due to a single overload.(1) Not all osteoporosis-related fractures, however, are caused by the application of a high load. Most loading during daily activities occurs at levels well below failure loads. Over time, these repetitive loads can lead to failure, particularly at sites such as the vertebra. By investigating the alterations in fatigue properties caused by osteoporosis and osteoporosis treatments, we can better understand bone fragility.

Osteoporotic fractures mainly occur at the spine, hip and wrist,(2) sites that contain large volumes of cancellous bone. The complex architecture of cancellous bone can be characterized as rod- and plate-type structures.(3) The contribution of each type of trabecula to the mechanical properties of the whole tissue has been examined through microCT images and finite element simulations.(4) When a single compressive

---

*Submitted to Bone. Julia T. Chen, Laurianne Imbert, Lyudmila Spevak, Lyudmila Lukashova, Ed DiCarlo Stephen B. Doty, Yihe Huang, Yan Ma, Elizabeth G. Pluhar, Christopher J. Hernandez, Adele L. Boseky, Marjolein C.H. van der Meulen. Parathyroid Hormone (PTH) Improves Bone Heterogeneity and Preserves Mechanical Properties of Cancellous Bone Before Fatigue Failure in a Sheep Model of Osteoporosis.

load to 1% strain was simulated, rod-like trabeculae failed early while plate-type trabeculae failed after yielding. Plate-shaped trabeculae, primary aligning with loading direction, are important to withstand single compressive loading whereas rod-type trabeculae are critical to stabilize the whole structure and to initiate failure.[4]

Besides tissue architecture, tissue mechanical and material properties are also important contributors to fracture risk. Local variations in tissue properties result from remodeling. Mineral and matrix constituents vary within each trabecula as a result of bone turnover initiated on the surface.[5-7] Heterogeneity of the mineralized tissue is decreased by osteoporosis and bisphosphonate treatment.[8,9] The loss of heterogeneity, with a corresponding increase of microcracks in the tissue, is thought to decrease mechanical strength and facilitate crack propagation.[10] Lower indentation modulus and mineralization near surfaces of trabeculae were measured with anti-resorptive treatment in a sheep model.[11] Therefore, both alterations of microarchitecture and tissue properties of osteoporotic and treated cancellous tissue should be examined to fully understand bone fracture.

Intermittent parathyroid hormone (iPTH) is an FDA-approved anabolic osteoporosis treatment that prolongs the life span of osteoblasts and stimulates bone formation.[12-14] Clinically, PTH decreases fracture risk of the spine by 10%.[15] Cancellous bone volume increases with PTH treatment and trabecular numbers and thickness are elevated clinically and in animal models.[16-20] Moreover, PTH increases bone strength at the femoral neck and vertebra in ovariectomized rat models.[21,22] However, its effect on bone tissue composition and mechanics in larger animals is unknown, particularly under cyclic fatigue loading.

The main goal of this study was to determine the effect of PTH on material and mechanical properties of cancellous bone at both the micro- and nanoscale using a sheep model of osteoporosis. Additionally, we examined the correlation between the alterations in architecture and composition, and mechanical properties. Our hypothesis was that PTH would improve measures of bone quality, such as tissue heterogeneity, and preserve mechanical properties during cyclic fatigue loading through architectural and compositional changes relative to osteopenic ewes.

3.2 Methods

3.2.1 Animal model

Under an IACUC-approved protocol at the University of Minnesota (#0907A68881) and Hospital for Special Surgery (#11-09-02E), thirteen mature Swiss Ramboulet female ewes (6-7 years old, weighing 69-82 kg at the start of the experiment) were ovariectomized and fed a metabolic acidosis (MA) diet for one year.[11] All ewes were then remained on the MA diet, and seven sheep were randomized into the parathyroid hormone treatment group (teriparatide 1-34, generously provided by Eli Lilly, 5μg/kg/day subcutaneous injection, PTH group, n = 7) and the remaining six sheep received saline injections (Vehicle group, n = 6) for the following one year.

Ewes were weighed monthly and subjected to bone density measurements at the onset (0 month), one year after ovariectomy (13 month), and terminus of the experiment (24 month) (General Electric Lunar DEXA machine, Madison, Wisconsin, USA).

Quarterly serum analysis of PTH, calcium, CTx, NTx and vitamin D was provided over 2 years. One year after treatment with either PTH or saline, the ewes were euthanized. Sheep were given tetracycline injections 18 and 9 days before euthanasia for analysis of mineral apposition rate (MAR, μm/day). Cancellous tissue characterization was performed on two cores and one section from the distal end of the right femur, one core from the L6 vertebrae, and two biopsies from the iliac crest taken at 13 and 24 months.

3.2.2 MicroCT (2 femoral cores, 1 vertebral core, 2 iliac crest biopsies per sheep)

Cancellous bone architecture of all femoral and vertebral cores and iliac crest biopsies was examined by microCT. (12 μm voxel size, Micro-CT35, Scanco Medical AG, Brüttiselen, Switzerland or 25 μm voxel size, eXplore CT 120, GE Healthcare, Waukesha, WI, USA). Trabecular bone volume fraction (BV/TV), trabecular number (Tb.N), trabecular thickness (Tb.Th), trabecular separation (Tb.Sp), tissue mineral density (TMD) and connectivity density (Conn.D) were measured.

3.2.3 Individual trabeculae segmentation (ITS) (2 femoral cores and 1 vertebral core per sheep)

Cancellous morphology of the femoral and vertebral cores was evaluated using individual trabeculae segmentation (ITS). MicroCT images were segmented to identify individual plates and rods.[3] Number, volume fraction, and mean thickness/diameter were determined for rod- (rN, rBV/TV, rTb.Th) and plate-like trabeculae (pN, pBV/TV, pTb.Th). Orientations of each type were characterized as

longitudinal ($0° \leq \Phi \leq 30°$), oblique ($30° < \Phi \leq 60°$), and transverse ($60° < \Phi \leq 90°$). Volume fraction for each orientation within the type was also calculated.

3.2.4 Bulk cancellous tissue preparation (2 femoral cores per sheep)

Tissue architecture and mechanical properties were characterized in femoral cores (n = 2/sheep). Bulk samples were visually aligned in the principal stress directions[23] (Faxitron, Hewlett Packard, McMinnville, Oregon, USA) prior to removing cancellous cores (7.5 mm). Both ends of each specimen were glued (Loctite 406, Newington, CT, USA) into customized press-fit brass end-caps[24]. The average original length, exposed length and diameter of the core were measured for stress and strain calculation.

3.2.5 Monotonic compression and ashing (1 femoral core per sheep)

Bulk tissue properties were characterized by monotonic compression on a single femoral core. Preconditioning was completed by 5 cycles of 0 to 0.1% compressive strain. After preconditioning, monotonic loading was applied until 2.5% strain (858 Mini Bionix, MTS, Eden Prairie, MN, USA). Young's modulus, yield strength and ultimate strength were determined. After monotonic loading, cores were cut from the end caps and ashed at 600 ˚C for 18 hours. Ash fraction was calculated as ash weight/dry bone weight.[25]

3.2.6 Cyclic fatigue tests and damage staining (1 femoral core per sheep)

Using the second femoral core, fatigue behavior was determined by cyclic compressive loading (Bose Electroforce LM-1, Eden Prairie, Minnesota, USA). Preconditioning from 0%-0.1% strain was applied to calculate the initial modulus (E_0) and the force corresponding to a normalized stress (σ/E_0) of 0.004 mm/mm. Samples were loaded in force control between 0 N and the desired force at 4Hz using a haversine waveform until 2.5% strain. All testing was conducted at physiologic temperature (37˚C) in hydroxyapatite-buffered PBS. Cycles-to-failure (N_f), percent change of secant modulus (E/E_0 -1), and energy dissipation (U, kJ/m^3) were determined. Following fatigue loading, damage volume fraction (DV/BV) was determined with lead uranyl acetate (LUA).[26,27]

3.2.7 Tissue preparation (1 femoral section, 1 vertebral core and 2 iliac crest biopsies per sheep)

Nanoscale composition and nanomechanical properties of cancellous tissue from the femur, vertebra and iliac crest were characterized using nanoindentation, Raman spectroscopy, Fourier transform infra-red spectroscopy Imaging (FTIRI) and AFM-IR. Tissue samples were embedded in PMMA. For nanoindentation and Raman spectroscopy, a 3-mm slice was cut from the embedded distal femur and polished anhydrously.[28] For FTIRI, 1-2 μm thick sections were cut from the embedded iliac crest biopsies and vertebral core (Leica SM 2500 tissue microtome). For AFM-IR, 300 nm thick sections were cut from the embedded vertebral core (Reichert-Jung Ultracut E ultramicrotome, Vienna, Austria).

3.2.8 Nanoindentation (1 femoral section per sheep)

Tissue nanomechanical properties were determined using nanoindentation. Indents were made with a Berkovich diamond indenter in three selected trabeculae, resulting in 30-45 indentations per animal (TriboIndenter, Hyistron Inc., Minneapolis, MN).[11] The load function included a 10 second hold at 700 μN with loading/unloading at a rate of 50 μN/s, resulting in ~150 nm indentation depth. The indentation modulus (E_i) and hardness (H) were calculated from the unloading part of the load-displacement curve.[11,28,29]

3.2.9 Raman Spectroscopy (1 femoral section per sheep)

Nanoscale tissue composition was evaluated with Raman spectroscopy (InVia microRaman, Renishaw, Gloucestershire, United Kingdom).[30]. A 2 μm^2 laser spot was centered at the same mid-lamellar locations probed by nanoindentation. Spectra were collected between 800 and 1800 cm^{-1} with background fluorescence removed using WiRE^{TM} V4.1 software (Reinshaw). Outcomes included tissue mineralization (mineral:matrix), B-type carbonate substitution (carbonate:phosphate), and crystallinity.[30]

3.2.10 FTIRI (1 vertebral core and 2 iliac crest biopsies per sheep)

FTIRI spectra of vertebra and iliac crest specimens were collected, baselined

and analyzed as detailed elsewhere[31] (Spectrum 300 Imaging System, Perkin Elmer CT, USA; Isys 5 software, Spectral Dimensions, MD USA). Outcomes included mineral-to-matrix ratio (M/M), carbonate substitution (CO_3/PO_4), crystallinity (XST), acid phosphate substitution ratio (HPO_4) and collagen crosslink ratio (XLR).[31] In addition to mean values, heterogeneity was determined from the pixel distributions for each parameter.[9]

3.2.11 AFM-IR (1 vertebral core per sheep)

Three trabeculae per sample were analyzed by AFM-IR (nano-IR2^{TM} Anasys Instruments, Santa Barbara, CA). Data were acquired in contact mode using an Arrow cantilever (Anasys Instrument model PR-EX-nIR2-10). Images were collected at 6 different wavenumbers (1030 cm^{-1}, 1660 cm^{-1}, 1020 cm^{-1}, 1690 cm^{-1}, 1128 cm^{-1}, 1096 cm^{-1}) and analyzed at 50-100 nm spatial resolution (Analysis Studio software, Anasys Instruments, Santa Barbara, CA). All spectra were collected over a range of 900–1800 cm^{-1} at 4 cm^{-1} spectral resolution, then smoothed using a Savitzky-Golay filter and baselined (MATLAB, Mathworks®, Massachusetts, U.S.A). Outcomes included mineral:matrix ratio, crystallinity, collagen crosslink ratio, and acid phosphate substitution ratio.[32]

3.2.12 Data analysis

PTH-treatment effects on serum markers, microCT, ITS, mechanical testing and AFM-IR measurements were analyzed with Student's t-test (JMP 11.0, SAS

Institute, INC.). Data collected from nanoindentation and Raman spectroscopy were classified into three groups [11]: Superficial (< 20 μm away from trabecular edge), Intermediate (20-40 μm away from trabecular edge) and Central (> 40 μm from trabecular edge). Repeated nested ANOVA or generalized estimating equations (GEE) determined the effects of PTH treatment and tissue age on cancellous tissue properties from nanoindentation, Raman spectroscopy and FTIR. Regression analysis was performed with averaged values to determine the contribution of composition and microarchitecture to mechanical properties. Significance level was $p < 0.05$.

3.3 Results

3.3.1 Animal model

Vehicle group gained weight gradually throughout 24 months (Table 3.1). PTH-treated ewes, however, failed to gain weight during 24 months and weighted less than Vehicle group. At the onset of treatment, PTH level in the treated ewes rapidly increased, reached a plateau and remained at that level. Despite these increases in PTH level, calcium level remained steadfast (1.08±0.18 mg/l in Vehicle and 1.060±0.11 mg/l in PTH). Vitamin D level was comparable until month 20 (69±7 nmoles/L in Vehicle and 63±10 nmoles/L in PTH). 24 months following ovariectomy, vitamin D level in the PTH-treated ewes (61.14 ±18.67 nmoles/L) was at a significantly lower level than that in the Vehicle group (84.50 ±10.74 nmoles/L, $p = 0.012$, Table 1). CTx and NTx turnover markers did not vary throughout the study (Table 3.1). At 17 month, however, CTx in the PTH-treated ewes was greater than that in Vehicle. The bone mineral density

in vertebra from Vehicle group, determined by DEXA, was significantly lower at 0 month (Table 3.1). PTH maintained BMD after 1 year of treatment whereas BMD decreased in Vehicle group at 24 month compared to 13 month. Mineral apposition rate (MAR) in spine from Vehicle group was not lower (1.538 ± 0.06 μm/day) than that from PTH group (1.622 ± 0.23 μm/day).

Table 3.1 *Sheep body weight was lower with PTH treatment. Bone mineral density was maintained by PTH treatment whereas BMD had a trend towards decreasing in Vehicle group. Vitamin D was decreased at 24 months in PTH-treated group. Changes in serum CTx had a trend towards increasing with PTH treatment. Serum PTH at 24 months was higher in the PTH treatment group.*
*Data shown as mean (SD). *p < 0.05. **p < 0.1. $^{+}$compared the difference between 24 mo. to 13 mo. with treatment effect (p < 0.1).*

	Onset (ovariectomy) (0 mo.)		1 year after ovariectomy (13 mo.)		1 year after treatment (24 mo.)	
	Vehicle	**PTH**	**Vehicle**	**PTH**	**Vehicle**	**PTH**
Sheep characteristics						
Body weight (lb)	163.3 (7.7)	165.3 (8.3)	185.8 (8.0)	166.4 (11.8)*	185.5 (11.4)	157.9 (20.1)*
BMD (g/cm^2)	1.19 (0.15)	1.36 (0.18)*	1.28 (0.18)	1.21 (0.13)	1.16 (0.20)$^{+}$	1.16 (0.22)
Serum markers						
Calcium (mg/L)	1.11 (0.07)	1.03 (0.04)	0.74 (0.27)	0.89 (0.27)	1.20 (0.11)	1.12 (0.05)
Vitamin D (nmolel/L)	76.17 (12.9)	71.83 (19.9)	61.00 (19.9)	50.43 (15.6)	84.5 (11.8)	61.14 (20.2)*
CTx (ng/mL)	0.56 (0.3)	0.59 (0.2)	0.41 (0.2)	0.64 (0.5)**	0.18 (0.1)	0.86 (1.6)**
NTx	51.16 (20.6)	49.72 (25.8)	43.17 (30.4)	41.81 (13.4)	57.01 (22.6)	51.27 (28.9)
PTH (pmol/L)	0.05 (0.12)	0.03 (0.08)	0.22 (0.17)	0.11 (0.15)	0.05 (0.12)	0.31 (0.18)*

3.3.2 MicroCT (2 femoral cores, 1 vertebral core, 2 iliac crest biopsies per sheep)

MicroCT analysis for femoral cores (Table 3.2) had lower Tb.Sp and higher Connn.D in PTH group compared to Vehicle group. Other parameters were not different. In the vertebra no significant differences were noted. In iliac crest biopsies,

PTH maintained most parameters. BV/TV in the PTH group had a trend towards experiencing 35% less bone loss compared to the Vehicle group ($p < 0.1$). Compared to baseline, PTH treatment prevented a significant decrease in Tb.Th compared to the Vehicle group in iliac crest.

Table 3.2 *Loss of bone volume fraction from the cancellous site at iliac crest had a trend towards maintaining by PTH treatment. Trabecular number (Tb.N) was higher and trabecular separation (Tb.Sp) decreased with PTH treatment in femur. Data shown as mean (SD). *p < 0.05. **p < 0.1*
[a]Significant increase compared to baseline.
[b]Significant decrease compared to baseline

	Vehicle Group	**PTH Group**
Iliac crest		
Bone volume fraction (BV/TV)	0.14 (0.01)[b]	0.19 (0.03)**[b]
Tissue mineral density (TMD)	594.77 (21.92)	704.8 (16.90)
Trabecular thickness (Tb.Th)	0.10 (0.01)[b]	0.13 (0.03)
Trabecular separation (Tb.Sp)	0.56 (0.06)[a]	0.67 (0.06)[a]
Trabecular number (Tb.N)	1.30 (0.14)[b]	1.50 (0.15)[b]
Vertebra		
Bone volume fraction (BV/TV)	0.28 (0.02)	0.36 (0.20)
Tissue mineral density (TMD)	848.97 (30.31)	870.53 (35.25)
Trabecular thickness (Tb.Th)	0.13 (0.01)	0.15 (0.04)
Trabecular separation (Tb.Sp)	0.43 (0.06)	0.42 (0.14)
Trabecular number (Tb.N)	2.71 (0.50)	3.12 (1.67)
Femur		
Bone volume fraction (BV/TV)	0.25 (0.06)	0.22 (0.05)
Trabecular thickness (Tb.Th)	198.3 (23.03)	199.9 (18.90)
Trabecular separation (Tb.Sp)	6.20 (1.90)	4.29 (1.30)*
Trabecular number (Tb.N)	1.05 (0.40)	1.39 (0.80)*

3.3.3 Individual trabeculae segmentation (ITS) (2 femoral cores and 1 vertebral core per sheep)

Microstructure differed among regions of the skeleton (Table 3.3). In femoral cores, rN and rBV/TV were 12.5% and 52.0% greater with PTH treatment compared to the Vehicle group. rBV/TV in longitudinal, transverse, and oblique orientations were

all increased by 144.4%, 55.6%, and 32.8% ($p < 0.1$) in the PTH group relative to Vehicle group. pBV/TV declined by 5.8% with PTH treatment; specifically, pBV/TV in longitudinal orientation had a trend towards decreasing 10.1% ($p < 0.1$). pTb.Th and rTb.Th were not different between two groups. In the vertebra, rTb.Th was lower and pBV/TV in the oblique direction was higher in the PTH-treated group. There were trends for a lower pBV/TV in longitudinal direction, a higher pBV/TV in transverse direction and a higher pTb.Th in the PTH-treated group.

Table 3.3 *PTH treatment has anatomic-dependent effects. In femur, number and volume fraction of rods were increased with PTH treatment whereas in vertebrae, mean plate-shaped trabecular thickness was increased with PTH treatment. Data shown as mean (SD). *p < 0.05. **p < 0.1*

	Femur		Vertebra	
	Vehicle Group	**PTH Group**	**Vehicle Group**	**PTH Group**
Number of plates (pN, 1/mm)	3.74 (0.20)	3.90 (0.51)	3.44 (0.23)	3.23 (0.36)
Number of rods (rN, 1/mm)	2.56 (0.25)	2.88 (0.37)*	2.01 (0.19)	2.01 (0.29)
Volume fraction of plates (pBV/TV)	0.898 (0.04)	0.846 (0.05)*	0.971 (0.007)	0.975 (0.011)
Volume fraction of rods (rBV/TV)	0.102 (0.03)	0.155 (0.05)*	0.031 (0.006)	0.028 (0.01)
pBV/TV in longitudinal orientation	0.666 (0.07)	0.599 (0.08)**	0.87 (0.03)	0.85 (0.04)**
pBV/TV in transverse orientation	0.058 (0.01)	0.065 (0.02)	0.028 (0.008)	0.034 (0.01)**
pBV/TV in oblique orientation	0.174 (0.03)	0.183 (0.05)	0.074 (0.01)	0.095 (0.03)*
rBV/TV in longitudinal orientation	0.009 (0.004)	0.022 (0.013)*	0.003 (0.0007)	0.003 (0.001)
rBV/TV in transverse orientation	0.036 (0.01)	0.056 (0.02)*	0.02 (0.004)	0.02 (0.006)
rBV/TV in oblique orientation	0.058 (0.02)	0.077 (0.02)**	0.008 (0.002)	0.008 (0.003)
Mean plate-shaped trabecular thickness (pTb.Th, μm)	150.4 (16.6)	153.9 (28.4)	150.8 (6.4)	166.9 (21.7)*
Mean rod-shaped trabecular diameter (rTb.Th, μm)	129.4 (9.91)	132.7 (10.7)	106.8 (6.05)	100.4 (6.32)*

3.3.4 Mechanical tests at bulk and tissue-level (2 femoral cores and 1 femoral section per sheep)

The effect of PTH treatment was evident in the resistance to fatigue loading but not for monotonic loading. Young's modulus, yield stress/strain, ultimate stress/strain, total toughness to ultimate, and ash fraction from monotonic compression were not different among groups (Table 3.4). E_0, N_f, and DV/BV from cyclic fatigue loading were not different between two groups (Table 3.4). However, reduction in modulus and energy dissipation were maintained with PTH treatment relative to the Vehicle group before fatigue failure (Figure 3.1). Additionally, E_i was 10.7% greater at Central and 11.6% greater at Intermediate with PTH treatment (Figure 3.2). H was not different with PTH treatment (Figure 3.2).

Table 3.4 *No treatment effect with monotonic compression strength and fatigue life compared to Vehicle group.*

	Vehicle Group	**PTH Group**
Monotonic compression loading		
Young's modulus (MPa)	662.6 (312)	839.3 (374)
Yield stress (MPa)	4.15 (1.6)	4.96 (2.1)
Yield strain (%)	0.86 (0.2)	0.80 (0.1)
Ultimate stress (MPa)	5.38 (1.7)	5.91 (1.9)
Ultimate strain (%)	2.32 (0.86)	1.75 (0.66)
Total toughness to ultimate (kJ/m^3)	91.15 (44.0)	70.24 (20.1)
Ash fraction (%)	66.87 (8.91)	61.51 (11.9)
Cyclic fatigue loading		
Failure cycles (N_f, 10^6 cycles)	0.81 (1.4)	1.77 (2.7)
Initial modulus (E_0, MPa)	477.1 (212)	516.1 (122)
Damage fraction (DV/BV, %)	8.7 (6)	9.3 (6)

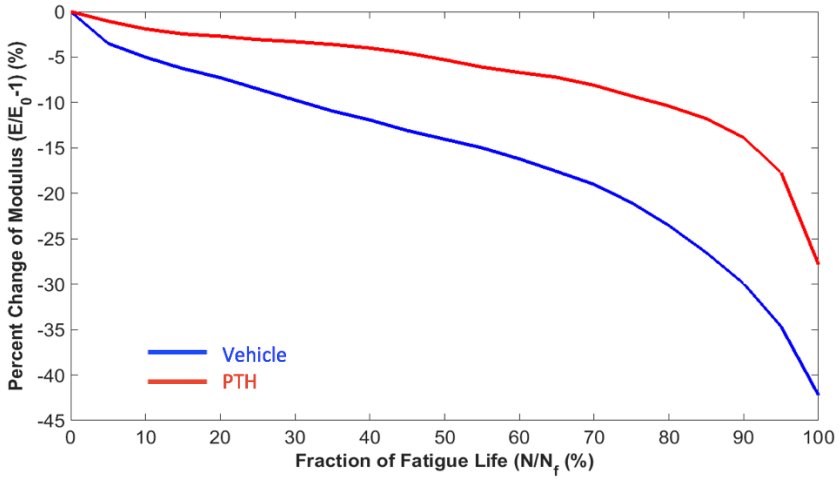

A

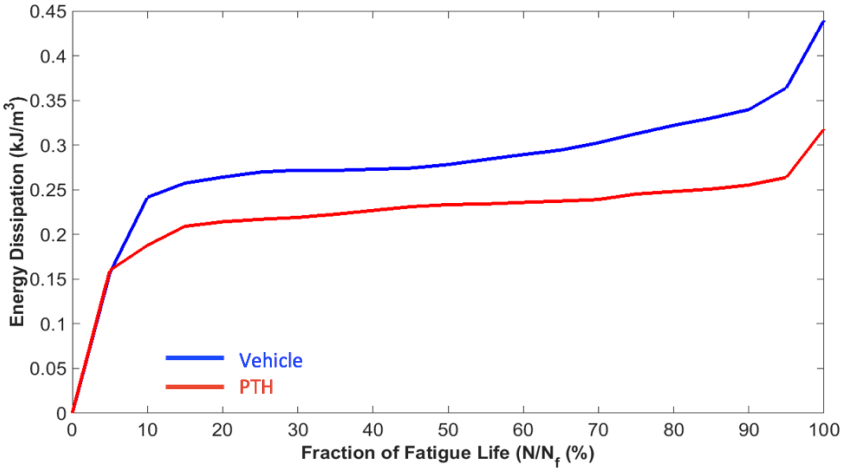

B

Figure 3.1 *PTH (A) maintained modulus and (B) experienced less energy dissipation during fatigue loading vs. Vehicle. Data shown as fraction of total fatigue life (0-100%). PTH = red lines; Vehicle = blue lines.*

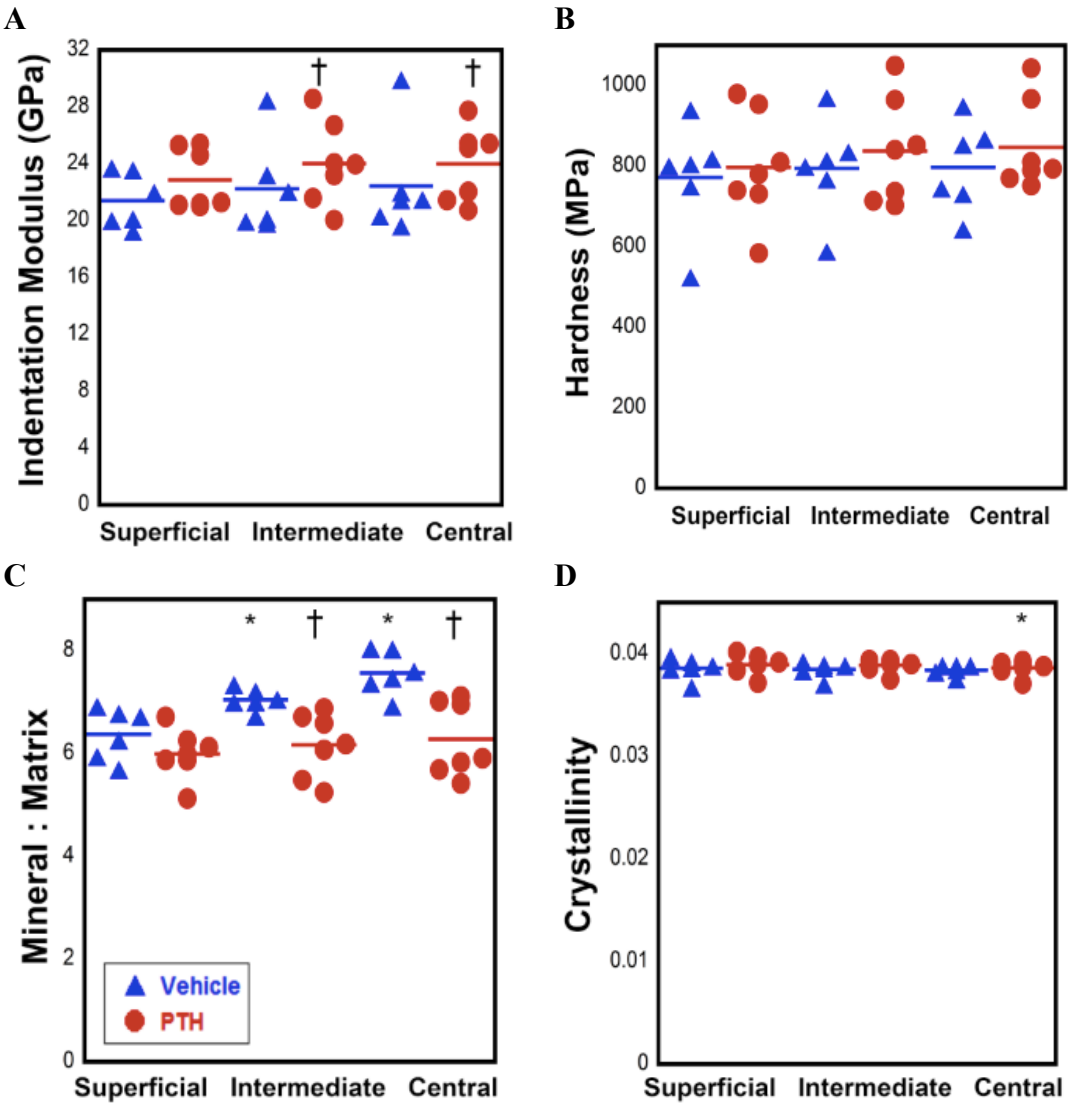

Figure 3.2 *(A) Indentation modulus (E_i) in Intermediate and Central increased with PTH treatment. (B) No treatment effect with hardness (H). (C) Mineralization in Central and Intermediate declined in PTH group. (D) Crystallinity was not affected by PTH treatment.*
*Blue empty bar indicated Vehicle group. Red solid bar indicated PTH group. †different from Vehicle group for the region indicated; *different from Superficial within the indicated group.*

3.3.5 Raman (1 femoral section per sheep)

Mineralization declined by 18.3% within Central and by 11.5% within

Intermediate with PTH treatment compared to the Vehicle group (Figure 3.2). Mineralization was higher in Central and Intermediate compared to Superficial zone. B-type carbonate substitution and crystallinity were not affected by PTH treatment (Figure 3.2).

3.3.6 Regression Analysis

Correlations between composition, microarchitecture and mechanical properties were examined. rBV/TV explained 50% of the variation in energy dissipation. pBV/TV in oblique orientation explained 57% of the variation in N_f while pBV/TV in longitudinal direction explained 60% of the variation of E_o. In addition, 77% of the variation in energy dissipation was explained by rBV/TV and mineralization (Table 3.5).

Table 3.5 *Correlations between microarchitecture, composition and mechanical properties. 77% of the variation in energy dissipation was explained by volume fraction of rods and mineralization. Shaded rows indicated more than one independent variables in the regression model. *p < 0.05.*

Predictor	*Response (Independent Variables)*	*Adjusted R^2*
Energy dissipation	Volume fraction of rods (rBV/TV)	0.40*
Energy dissipation	Mineralization (Superficial)	0.14
Energy dissipation	rBV/TV, Mineralization (Superficial)	0.77*
Fatigue life	Volume fraction of plates in transverse orientation	0.50*
Fatigue life	Volume fraction of plates in oblique orientation	0.57*
Initial modulus	Volume fraction of plates in longitudinal orientation	0.60*

3.3.7 FTIRI (1 vertebral core and 2 iliac crest biopsies per sheep)

Vertebral core at 24 month had no significant difference in means between two

groups (Table 3.6). Collagen crosslink ratio had a trend towards a decrease with PTH treatment. PTH treatment prevented the loss in crystallinity associated with ovariectomy and metabolic acidosis in iliac crest. Moreover, PTH treatment improved two parameters, carbonate-to-phosphate ratio decreased and acid phosphate substitution ratio increased relative to baseline.

The distribution of pixel intensities was characterized in terms of the line-width at half-maximum of the pixel histogram for each image. The averages of these heterogeneities (Table 3.6) showed that mineral-to-matrix heterogeneity was maintained and carbonate-to-phosphate heterogeneity was increased by PTH treatment compared to baseline in iliac crest. PTH treatment also prevented the loss in crystallinity heterogeneity; however, unexpectedly the carbonate-to-phosphate heterogeneity was also increased in the Vehicle group compared to baseline. None of the other variables were different from the Vehicle group because of the large scatter in the data.

Table 3.6 *FTIR mean and heterogeneity results in the iliac crest and vertebra. In the vertebra, there is no significant difference between Vehicle and PTH groups. In the iliac crest, the ovariectomized animals had higher crystallinity compared to baseline. PTH decreased the carbonate-to-phosphate ratio and increased the acid-phosphate-substitution ratio and the crystallinity heterogeneity compared to baseline.*
[a]vehicle is significantly different from baseline p<0.05
[b]PTH is significantly different from baseline p<0.05
**Vehicle is significantly different from PTH at completion p<0.05. ** p<0.1*

	Iliac crest			Vertebra	
	Baseline	**Vehicle**	**PTH**	**Vehicle**	**PTH**
Mean					
M/M	4.245±0.583	4.232±0.409	4.219±0.348	4.707±0.269	4.883±0.294
CO_3/PO_4x10^3	8.367±0.675[b]	8.100±1.010	7.286±1.074[b]	7.443±0.963	7.381±0.419
XST	1.180±0.020[a]	1.203±0.018[a]	1.193±0.030*	1.239 ±0.023	1.215±0.060
HPO_4	0.472±0.043[b]	0.476±0.032	0.496±0.040[b]	0.384±0.027	0.394±0.014
XLR	3.794±0.282	4.384±0.590	4.189±0.583	3.870±0.369	3.586±0.288**
Heterogeneity					
M/M	0.951±0.123[a]	0.833±0.182[a]	1.030±0.147	1.505±0.099	1.632±0.288
CO_3/PO_4x10^3	2.276±0.366[a,b]	2.679±0.553[a]	2.473±0.333[b]	2.678±0.163	2.995±0.053
XST	0.069±0.009[a,b]	0.067±0.011[a]	0.068±0.010[b]	0.139±0.015	0.135±0.028
HPO_4	0.062±0.017	0.082±0.027	0.067±0.012	0.104±0.011	0.111±0.022
XLR	0.350±0.090	0.346±0.078	0.360±0.131	0.490±0.104	0.421±0.081

3.3.8 AFM-IR (1 vertebral core per sheep)

To characterize the least-mature bone tissue, AFM-IR were performed on the tissue between double fluorescent labels. In this newly-formed bone tissue (superficial zone), higher mineral content, higher collagen content and collagen maturity were captured by line scans in PTH group compared to Vehicle group (Figure 3.3). In addition, PTH group had higher mineral-to-matrix ratio, crystallinity and collagen crosslink ratio and lower acid phosphate substitution ratio in IR images (Figure 3.4), indicating a faster maturation process. In the more-mature bone tissue (central zone)

(Figure 3.4), the mineral-to-matrix ratio and the acid phosphate substitution ratio were lower in the PTH group compared to Vehicle group.

Both groups presented variations with bone maturity. Mineral-to-matrix ratio increased with bone maturity, due to an increase in mineral content and a decrease in collagen content, whereas the acid phosphate substitution ratio decreased with bone maturity. The IR images also showed the same variations of IR parameters with bone maturity (Figure 3.4).

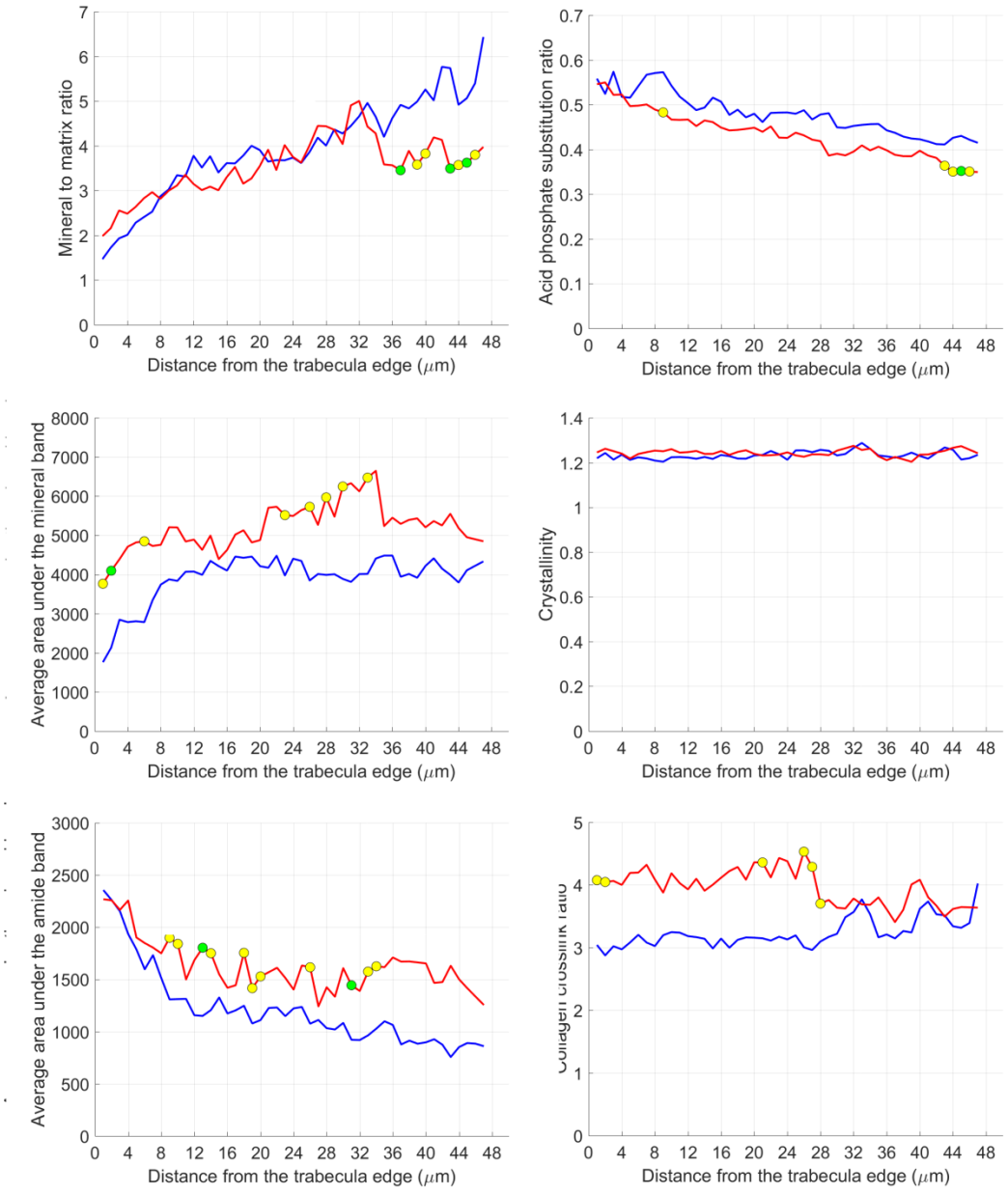

Figure 3.3 *AFM-IR parameters for the PTH group (red) compared to the Vehicle group (blue) as a function of distance from the trabecula edge, increasing distance representing more mature bone. The first 20 microns are considered as newly formed bone. In the newly formed bone, the bone formation process is accelerated when samples are treated with PTH. In the more mature bone, the bone formed with PTH has a lower mineral-to-matrix ratio and a lower acid-phosphate-substitution ratio. Green dot represented both groups are significantly different, yellow dot represented a trend.*

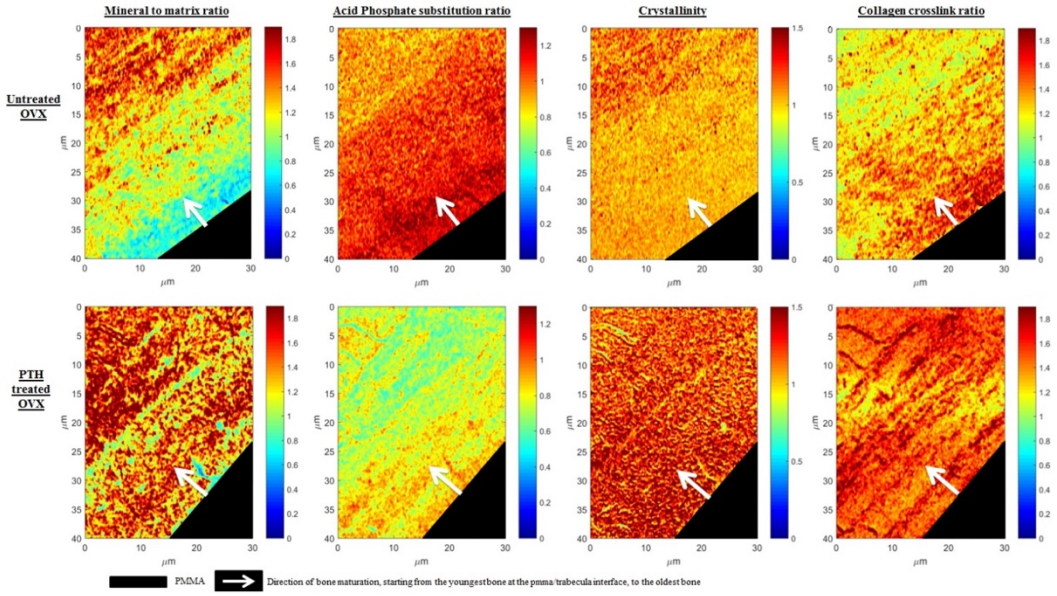

Figure 3.4 *AFM-IR images for one sample from the Vehicle group (top) and from the PTH group (bottom). In the first 20 microns from the trabecular edge, the PTH group shows higher mineral-to-matrix ratio, crystallinity and collagen crosslink ratio and lower acid phosphate substitution ratio, suggesting that the bone formation process is accelerated with PTH treatment.*

3.4 Discussion

PTH treatment is an FDA-approved anabolic agent for osteoporosis, stimulating bone formation in OVX animals[33] and in postmenopausal women;[34] thus potentially avoids the detrimental decrease in heterogeneity encountered with antiresorptive agents,[35] maintaining the mechanical integrity of bone.[36] Therefore, in the present study, we investigated the effect of intermittent PTH treatment on the mechanical properties and tissue heterogeneity in an osteopenia ovine model at several bone sites with microCT, histology, mechanical testing, nanoindentation, Raman, FTIR and AFM-

IR. We were able to verify our hypothesis that PTH treatment improved tissue heterogeneity and preserved the fatigue properties through increased rod-type trabeculae and tissue compositional changes.

PTH-treated sheep gained less weight, analogous to PTH-treated humans showing a weight loss, attributing to mild hypercalcemia reducing apatite.[37] However, hypercalcemia and altered vitamin D levels were not noted in these sheep. These sheep might be more active due to their improved health status. The metabolic acidosis diet can result in reduced muscle function correcting by a slight elevation in calcium level during PTH treatment. The paucity of labels in these samples was our failure to provide the tetracycline for multiple days prior to biopsy. Previous study[38] first injected tetracycline for two days before a 12-day break and a second injection for 14 days in PTH-treated sheep, showing a significant anabolic effect.

The ovariectomized ewe with metabolic acidosis had distinct changes at different bone sites.[39] Microarchitecture parameters measured by microCT were more altered in femur and iliac crest compared to vertebra, confirming a site-dependent effect of PTH. No significant difference was found in vertebra whereas Tb.N was higher and Tb.Sp was lower with PTH treatment in the femur. BV/TV was altered in iliac crest in PTH group compared to the Vehicle group (Table 2), consistent with new bone formation. Tb.Th and Tb.N were maintained with PTH treatment. Iida-Klein et al.[40] found a more robust response to PTH treatment in mice long bone relative to spine whereas the spine seemed to respond first in human. Moreover, as hypothesized by Iida-Klein, this difference might be due to a difference in posture,[40] and sheep have a posture closer to mice than to human.

ITS also showed site-dependent results. In femur, rN and rBV/TV increased whereas pBV/TV decreased. In vertebra, rTb.Th decreased whereas pTb.Th and pBV/TV in the oblique direction had a trend towards an increase. Injecting sclerostin antibody treatment in monkey model, which has shown to increase bone mineral density in vertebra and hip,[41,42] cancellous bone samples from vertebra had increased pTb.Th and converted rod- to plate-like trabeculae.[43] Those site-dependent results are likely to be associated with different loading conditions and mechanical purpose of the bone.

Absence of a greater difference between PTH and Vehicle groups may suggest there could be a different optimal duration for PTH treatment in sheep than in human, where 24 months of treatment is recommended.[44] Factors like age, because of the age-dependent effect of PTH treatment,[45] and turnover rate are also to be considered. Other studies treated elderly intact-ewes with PTH for only 3 months[38,46] and noted an increased bone turnover in iliac crest[38] or only at the lumbar spine.[46] The latter study, however, did not find any significant difference in microstructural parameters, suggesting that the osteoporotic model using old intact ewes was insufficient to see a major treatment effect. One can also consider the fact that two years post ovariectomy might not be representative of postmenopausal women turnover anymore because several studies showed ovariectomy altered turnover and material properties during the first year but after that period the effect stabilized or reduced.[47]

Despite the fact that no treatment-effect on monotonic strength, the resistance to fatigue loading was preserved with PTH treatment. Modulus reduction and energy dissipation under cyclic fatigue loading were maintained compared to Vehicle group (Figure 1). No one has studied the fatigue properties with PTH treatment in cancellous

bone with ovariectomized sheep model. In addition, fatigue loading occurs more frequently than traumatic single-overload. In cortical bone from these same sheep, we have shown increased fatigue life with PTH treatment compared to other anti-resorptive agents[48] and no difference in whole bone bending strength (Chen et al cortical paper). Therefore, PTH seems to affect fatigue behavior of bone tissue rather than monotonic resistance.

Tissue mineralization has shown to increase as tissue ages.[7,49] Therefore, decreased mineralization from Raman spectroscopy with PTH treatment indicated younger bone tissue in femur. 77% of the variation in energy dissipation was explained by rBV/TV and mineralization (Table 5). This correlation suggested that the preservation of mechanical properties before fatigue failure resulted from increased rod-type trabeculae and mineralization. Moreover, Torres et al. also showed rod-type trabeculae were important for initiation of fatigue failure.[50]

FTIRI did not show any significant difference in mineral-to-matrix ratio in the iliac crest and vertebra whereas Raman had decreased mineral-to-matrix ratio in femur. Ovariectomized monkeys treated with PTH for 18 months had a decrease in mineral-to-matrix ratio.[33] Similarly, in iliac crest biopsies from PTH–treated women with fractures contrasting to women who received no anabolic agent, had decreased mineral-to-matrix levels in cancellous bone.[31,51] Besides, acid phosphate substitution ratio from FTIRI, indicating new mineral formation, was not different between groups; perhaps due to the slow turnover rate in the sheep.

Carbonate-to-phosphate ratio was decreased compared to baseline (13 month), indicating there was increased remodeling in this model.[52] An increase in turnover with

PTH with a decrease in carbonate-to-phosphate ratio was similarly reported in PTH-treated intact mice.[53] There was no difference in carbonate-to-phosphate ratio in the human study of PTH-treated fractured patients, resulting from the small sample size.

Crystallinity was lower in the PTH-treated ewes at completion of the study, suggesting PTH prevented the increase of crystallinity caused by ovariectomy.[31,51] Crystallinity was also decreased in PTH-treated ovariectomized monkeys,[33] in PTH-treated women with fractures,[31] and in PTH-treated women for 19-24 months.[54] Similar lack of increase in collagen crosslink ratio had been reported in the PTH-treated ovariectomized monkeys[33] and PTH-treated women with fractures.[31] In agreement with the trend measured in the vertebra, decreases were reported in mice treated with PTH[55] and PTH-treated women.[54]

Heterogeneity of the bone matrix is important for preventing proliferation of micro-cracks.[10,56] Osteoporosis and bisphosphonate treatment decreased heterogeneity in human bone.[35,57] Our hypothesis was that PTH treatment, stimulating bone formation, would prevent the loss or increase heterogeneity in bone matrix. At micro-level, the heterogeneity of mineral-to-matrix ratio was decreased in Vehicle group but not in PTH-treated iliac crest. Unlike the increased heterogeneity in iliac crest of osteoporotic patients,[58] PTH prevented the loss in mineral-to-matrix heterogeneity in current study. Carbonate-to-phosphate ratio heterogeneity increased in the PTH group but the increase was less than in the Vehicle group; this unexpected result may be due to large standard deviations. The crystallinity heterogeneity was reduced in the PTH group but less than in the Vehicle group, which showed that PTH partially prevented the loss in crystallinity heterogeneity. Overall the heterogeneities were maintained or

increased as a consequence to PTH treatment, validating our hypothesis.

Focusing on newly formed bone at nano-level to characterize PTH treatment effect on the maturation process, AFM-IR measured higher mineral, higher collagen content and collagen maturity in PTH group. In more mature bone tissue, mineral-to-matrix ratio and acid phosphate substitution ratio were lower in the PTH group, suggesting new bone tissue was more youthful but with areas of high mineral maturity. These findings indicated that PTH treatment accelerated bone formation, but once the bone was mature, the mineral-to-matrix ratio tended to decrease as evidenced by Paschalis et al..[54]

More interestingly, AFM-IR was able to observe variations during the maturation process of new bone in both PTH- and saline-treated samples. An increase in mineral-to-matrix ratio and a decrease in acid phosphate substitution ratio during bone maturation were captured. Previous studies found the same variations with bone maturity.[59] For instance, Gourion et al. and Paschalis et al. found increased mineral-to-matrix ratio and crystallinity with distance from osteon center in baboon femur and human iliac crest.[49,57]

This study has several limitations. The extent of osteoporosis in our saline-treated sheep was not severe, suggesting additional stresses are needed to mimic human condition. Additionally, for economic reasons, we did not have parallel normal controls. Moreover, the duration for PTH treatment in sheep is not established, and the anabolic window[60] may be different from that in humans. Ovariectomized old sheep in the current study might have a low turnover, resulting low possibility to see a major treatment effect.

In conclusion, utilizing ovariectomized-mature ewes placed on a metabolic acidosis diet for one year prior to PTH treatment, we were able to verify our hypothesis that PTH treatment preserved mechanical properties during fatigue loading by maintaining/improving tissue heterogeneity. Monotonic behavior was not different with PTH treatment compared to Vehicle group, which might indicate that PTH treatment altered fatigue behavior rather than monotonic behavior. PTH treatment partially prevented the loss of bone quality parameters (microarchitecture and composition) in femur and iliac crests but did not seem to be as effective in the vertebra, confirming a site-dependent effect of PTH treatment. We also correlated increased rod-type trabeculae and decreased mineralization with maintained energy dissipation, corresponding the alterations in tissue properties and microstructures contributed to resistance to fatigue loading. Moreover, an accelerated bone formation process as a consequence of PTH treatment was captured in a novel nanoscale spectroscopic method.

References

1. Cummings SR, Browner W, Black D, et al. Bone density at various sites for prediction of hip fractures. The Lancet. 1993;341(8837):72-5.

2. Consensus N. Development panel on osteoporosis: prevention, diagnosis and therapy. J Am Med Assoc. 2001;285(11).

3. Liu XS, Sajda P, Saha PK, et al. Complete volumetric decomposition of individual trabecular plates and rods and its morphological correlations with anisotropic elastic moduli in human trabecular bone. Journal of Bone and Mineral Research. 2008;23(2):223-35.

4. Liu XS, Bevill G, Keaveny TM, Sajda P, Guo XE. Micromechanical analyses of vertebral trabecular bone based on individual trabeculae segmentation of plates and rods. Journal of Biomechanics. 2009;42(3):249-56.

5. Tai K, Dao M, Suresh S, Palazoglu A, Ortiz C. Nanoscale heterogeneity promotes energy dissipation in bone. Nature Materials. 2007;6(6):454-62.

6. Van der Meulen M, Jepsen K, Mikić B. Understanding bone strength: size isn't everything. Bone. 2001;29(2):101-4.

7. Donnelly E, Boskey AL, Baker SP, Van der Meulen MC. Effects of tissue age on bone tissue material composition and nanomechanical properties in the rat cortex. Journal of Biomedical Materials Research. 2010;92(3):1048-56.

8. McCreadie BR, Morris MD, Chen TC, et al. Bone tissue compositional differences in women with and without osteoporotic fracture. Bone. 2006;39(6):1190-5.

9. Gourion-Arsiquaud S, Allen MR, Burr DB, Vashishth D, Tang SY, Boskey AL. Bisphosphonate treatment modifies canine bone mineral and matrix properties and their heterogeneity. Bone. 2010;46(3):666-72.

10. Ettinger B, Burr D, Ritchie R. Proposed pathogenesis for atypical femoral fractures: lessons from materials research. Bone. 2013.

11. Burket JC, Brooks DJ, MacLeay JM, Baker SP, Boskey AL, van der Meulen MC. Variations in nanomechanical properties and tissue composition within trabeculae from an ovine model of osteoporosis and treatment. Bone. 2013;52(1):326-36.

12. Jilka RL, Weinstein RS, Bellido T, Roberson P, Parfitt AM, Manolagas SC. Increased bone formation by prevention of osteoblast apoptosis with parathyroid hormone. Journal of Clinical Investigation. 1999;104(4):439-46.

13. Dobnig H, Turner RT. Evidence that intermittent treatment with parathyroid hormone increases bone formation in adult rats by activation of bone lining cells. Endocrinology. 1995;136(8):3632-8.

14. de Bakker CM, Altman AR, Tseng W-J, et al. μCT-based, in vivo dynamic bone histomorphometry allows 3D evaluation of the early responses of bone resorption and formation to PTH and alendronate combination therapy. Bone. 2015;73:198-207.

15. Neer RM, Arnaud CD, Zanchetta JR, et al. Effect of parathyroid hormone (1-34) on fractures and bone mineral density in postmenopausal women with osteoporosis. New England journal of medicine. 2001;344(19):1434-41.

16. Dempster DW, Cosman F, Kurland ES, et al. Effects of daily treatment with parathyroid hormone on bone microarchitecture and turnover in patients with osteoporosis: a paired biopsy study. Journal of Bone and Mineral Research. 2001;16(10):1846-53.

17. Jerome C, Burr D, Van Bibber T, Hock J, Brommage R. Treatment with human parathyroid hormone (1-34) for 18 months increases cancellous bone volume and improves trabecular architecture in ovariectomized cynomolgus monkeys (Macaca fascicularis). Bone. 2001;28(2):150-9.

18. Jiang Y, Zhao JJ, Mitlak BH, Wang O, Genant HK, Eriksen EF. Recombinant human parathyroid hormone (1–34)[teriparatide] improves both cortical and cancellous bone structure. Journal of Bone and Mineral Research. 2003;18(11):1932-41.

19. Lane NE, Thompson J, Strewler GJ, Kinney J. Intermittent treatment with human parathyroid hormone (hPTH [1-34]) increased trabecular bone volume

but not connectivity in osteopenic rats. Journal of Bone and Mineral Research. 1995;10(10):1470-7.

20. Zhang L, Takahashi H, Inoue J, et al. Effects of intermittent administration of low dose human PTH (1–34) on cancellous and cortical bone of lumbar vertebral bodies in adult beagles. Bone. 1997;21(6):501-6.

21. Ejersted C, Andreassen T, Hauge E-M, Melsen F, Oxlund H. Parathyroid hormone (1–34) increases vertebral bone mass, compressive strength, and quality in old rats. Bone. 1995;17(6):507-11.

22. Søgaard C, Wronski T, McOsker J, Mosekilde L. The positive effect of parathyroid hormone on femoral neck bone strength in ovariectomized rats is more pronounced than that of estrogen or bisphosphonates. Endocrinology. 1994;134(2):650-7.

23. Morgan EF, Bayraktar HH, Keaveny TM. Trabecular bone modulus–density relationships depend on anatomic site. Journal of Biomechanics. 2003;36(7):897-904.

24. Keaveny TM, Pinilla TP, Crawford RP, Kopperdahl DL, Lou A. Systematic and random errors in compression testing of trabecular bone. Journal of Orthopaedic Research. 1997;15(1):101-10.

25. Carter DR, Caler WE, Spengler DM, Frankel VH. Fatigue behavior of adult cortical bone: the influence of mean strain and strain range. Acta Orthopaedica Scandinavica. 1981;52(5):481-90.

26. Schaffler M, Pitchford W, Choi K, Riddle J. Examination of compact bone microdamage using back-scattered electron microscopy. Bone. 1994;15(5):483-8.

27. Brock GR, Kim G, Ingraffea AR, Andrews JC, Pianetta P, van der Meulen MC. Nanoscale examination of microdamage in sheep cortical bone using synchrotron radiation transmission x-ray microscopy. PloS One. 2013;8(3):e57942.

28. Donnelly E, Baker SP, Boskey AL, van der Meulen MC. Effects of surface roughness and maximum load on the mechanical properties of cancellous bone

measured by nanoindentation. Journal of Biomedical Materials Research. 2006;77(2):426-35.

29. Rho JY, Tsui TY, Pharr GM. Elastic properties of human cortical and trabecular lamellar bone measured by nanoindentation. Biomaterials. 1997;18(20):1325-30.

30. Burket J, Gourion-Arsiquaud S, Havill LM, Baker SP, Boskey AL, Van der Meulen MC. Microstructure and nanomechanical properties in osteons relate to tissue and animal age. Journal of Biomechanics. 2011;44(2):277-84.

31. Boskey AL, Donnelly E, Boskey E, et al. Examining the Relationships Between Bone Tissue Composition, Compositional Heterogeneity, and Fragility Fracture: A Matched Case-Controlled FTIRI Study. Journal of Bone and Mineral Research. 2016;31(5):1070-81.

32. Gourion-Arsiquaud S, Marcott C, Hu Q, Boskey AL. Studying variations in bone composition at nano-scale resolution: a preliminary report. Calcified Tissue International. 2014;95(5):413-8.

33. Paschalis EP, Burr DB, Mendelsohn R, Hock JM, Boskey AL. Bone mineral and collagen quality in humeri of ovariectomized cynomolgus monkeys given rhPTH (1–34) for 18 months. Journal of Bone and Mineral Research. 2003;18(4):769-75.

34. Elaine WY, Neer RM, Lee H, et al. Time-dependent changes in skeletal response to teriparatide: Escalating vs. constant dose teriparatide (PTH 1–34) in osteoporotic women. Bone. 2011;48(4):713-9.

35. Donnelly E, Meredith DS, Nguyen JT, et al. Reduced cortical bone compositional heterogeneity with bisphosphonate treatment in postmenopausal women with intertrochanteric and subtrochanteric fractures. Journal of Bone and Mineral Research. 2012;27(3):672-8.

36. Gourion-Arsiquaud S, Lukashova L, Power J, Loveridge N, Reeve J, Boskey AL. Fourier transform infrared imaging of femoral neck bone: Reduced heterogeneity of mineral-to-matrix and carbonate-to-phosphate and more variable crystallinity in treatment-naive fracture cases compared with fracture-free controls. Journal of Bone and Mineral Research. 2013;28(1):150-61.

37. Schafer AL, Sellmeyer DE, Schwartz AV, et al. Change in undercarboxylated osteocalcin is associated with changes in body weight, fat mass, and adiponectin: parathyroid hormone (1-84) or alendronate therapy in postmenopausal women with osteoporosis (the PaTH study). Journal of Clinical Endocrinology & Metabolism. 2011;96(12):E1982-E9.

38. Delmas PD, Vergnaud P, Arlot ME, Pastoureau P, Meunier PJ, Nilssen M. The anabolic effect of human PTH (1–34) on bone formation is blunted when bone resorption is inhibited by the bisphosphonate tiludronate—is activated resorption a prerequisite for the in vivo effect of PTH on formation in a remodeling system? Bone. 1995;16(6):603-10.

39. Zarrinkalam M, Beard H, Schultz C, Moore R. Validation of the sheep as a large animal model for the study of vertebral osteoporosis. European Spine Journal. 2009;18(2):244-53.

40. Iida-Klein A, Zhou H, Lu SS, et al. Anabolic action of parathyroid hormone is skeletal site specific at the tissue and cellular levels in mice. Journal of Bone and Mineral Research. 2002;17(5):808-16.

41. Padhi D, Allison M, Kivitz AJ, et al. Multiple doses of sclerostin antibody romosozumab in healthy men and postmenopausal women with low bone mass: A randomized, double-blind, placebo-controlled study. Journal of Clinical Pharmacology. 2014;54(2):168-78.

42. McClung MR, Grauer A, Boonen S, et al. Romosozumab in postmenopausal women with low bone mineral density. New England Journal of Medicine. 2014;370(5):412-20.

43. Matheny JB, Torres AM, Ominsky MS, Hernandez CJ. Romosozumab Treatment Converts Trabecular Rods into Trabecular Plates in Male Cynomolgus Monkeys. Calcified Tissue International. 2017:1-10.

44. Johnston S, Andrews S, Shen V, et al. The effects of combination of alendronate and human parathyroid hormone (1–34) on bone strength are synergistic in the lumbar vertebra and additive in the femur of C57BL/6J mice. Endocrinology. 2007;148(9):4466-74.

45. Yukata K, Xie C, Li T-F, et al. Aging periosteal progenitor cells have reduced

regenerative responsiveness to bone injury and to the anabolic actions of PTH 1-34 treatment. Bone. 2014;62:79-89.

46. Portero-Muzy N, Chavassieux P, Bouxsein M, Gineyts E, Garnero P, Chapurlat R. Early effects of zoledronic acid and teriparatide on bone microarchitecture, remodeling and collagen crosslinks: comparison between iliac crest and lumbar vertebra in ewes. Bone. 2012;51(4):714-9.

47. Kreipke TC, Rivera NC, Garrison JG, Easley JT, Turner AS, Niebur GL. Alterations in trabecular bone microarchitecture in the ovine spine and distal femur following ovariectomy. Journal of Biomechanics. 2014;47(8):1918-21.

48. Brock GR, Chen JT, Ingraffea AR, et al. The effect of osteoporosis treatments on fatigue properties of cortical bone tissue. Bone Reports. 2015;2:8-13.

49. Paschalis E, DiCarlo E, Betts F, Sherman P, Mendelsohn R, Boskey A. FTIR microspectroscopic analysis of human osteonal bone. Calcified Tissue International. 1996;59(6):480-7.

50. Torres A MJ, Luna M, Lambers F, Rimnac C, Hernandez C. Trabecular Morphology Has Differential Effects in Uniaxial and Fatigue Failure of Cancellous Bone. European Society of Biomechanics Conference. Serville, Spain 2017.

51. Boskey AL. Bone composition: relationship to bone fragility and antiosteoporotic drug effects. BoneKEy Reports. 2013;2.

52. Isaksson H, Turunen MJ, Rieppo L, et al. Infrared spectroscopy indicates altered bone turnover and remodeling activity in renal osteodystrophy. Journal of Bone and Mineral Research. 2010;25(6):1360-6.

53. Bartlow CM, Oest ME, Mann KA, Zimmerman ND, Butt BB, Damron TA. PTH (1–34) and zoledronic acid have differing longitudinal effects on juvenile mouse femur strength and morphology. Journal of Orthopaedic Research. 2016.

54. Paschalis EP, Glass EV, Donley DW, Eriksen EF. Bone mineral and collagen quality in iliac crest biopsies of patients given teriparatide: new results from the fracture prevention trial. Journal of Clinical Endocrinology & Metabolism.

2005;90(8):4644-9.

55. Ross RD, Mashiatulla M, Robling AG, Miller LM, Sumner DR. Bone matrix composition following PTH treatment is not dependent on sclerostin status. Calcified Tissue International. 2016;98(2):149-57.

56. Torres AM, Matheny JB, Keaveny TM, Taylor D, Rimnac CM, Hernandez CJ. Material heterogeneity in cancellous bone promotes deformation recovery after mechanical failure. Proceedings of the National Academy of Sciences. 2016;113(11):2892-7.

57. Gourion-Arsiquaud S, Burket JC, Havill LM, et al. Spatial variation in osteonal bone properties relative to tissue and animal age. Journal of Bone and Mineral Research. 2009;24(7):1271-81.

58. Misof BM, Roschger P, Cosman F, et al. Effects of intermittent parathyroid hormone administration on bone mineralization density in iliac crest biopsies from patients with osteoporosis: a paired study before and after treatment. Journal of Clinical Endocrinology & Metabolism. 2003;88(3):1150-6.

59. Boskey AL, Coleman R. Aging and bone. Journal of Dental Research. 2010;89(12):1333-48.

60. Lindsay R, Krege J, Marin F, Jin L, Stepan J. Teriparatide for osteoporosis: importance of the full course. Osteoporosis International. 2016;27(8):2395-410.

CHAPTER 4

ROLE OF CORTICAL BONE MICROSTRUCTURE AND ANISOTROPY OF FRACTURE TOUGHNESS IN TISSUE FAILURE*

4.1 Introduction

Cortical bone is a relatively complex hierarchical material composed of fibers (osteons) within an interstitial matrix, similar to fiber-reinforced composites. Haversian canals with blood vessels are located in the middle of osteons. The interface between osteons and surrounding interstitial matrix is demonstrated by a cement line that behaves as a weak interface. This microstructural morphology is a critical to the mechanical properties of the tissue and determines the crack growth trajectory in cortical bone during failure. The presence of osteons reduced the strength and modulus of cortical bone but increased toughness by deviating or stopping crack propagation [1-3].

Fracture toughness, correlated with bone fragility, is a material property that determines the resistance to crack propagation when an initial crack is present. The relative toughness between two materials, toughness ratio, determines crack behavior at interfaces. For example, the cement line to osteon toughness ratio determined whether a crack deflected, when the cement line was tougher, or penetrated along the cement line, when the osteon was tougher [4,5]. However, these simulations assumed isotropic fracture toughness, based on available data and simulation methods.

---

*Submitted to Journal of Biomechanics. Julia T. Chen, Anthony Ingraffea, Marjolein C.H. van der Meulen. Role of Cortical Bone microstructure and anisotropy of fracture toughness in tissue failure.

Experimentally, fracture toughness of cortical bone can be determined at the microscale. Fracture toughness in cortical bone increases as a crack propagates [6,7]. In addition, fracture toughness is higher in the transverse than in the longitudinal direction [8,9]. To date measurements have focused mainly on longitudinal fracture in which a crack propagates parallel to the axis of the osteons. However, clinically the relevant crack orientation is transverse for propagation perpendicular to the axis of the osteons [6,7,10,11]. Bone fracture toughness at the nanoscale is anisotropic and difficult to measure. Therefore, anisotropic effects at the nanoscale have been examined using simulations [12].

Linear elastic fracture mechanics (LEFM) has been widely applied to characterize mechanical behavior in fiber-reinforced composite models [13,14]. Bone resistance to fracture has been characterized by LEFM [12,15-18], by measuring fracture toughness of cortical bone under tension/compression. However, bending is another common loading condition and may be more relevant to clinical events. In a beam under bending, the stress state varies with location and will be influenced by the microstructure. The effect of the location of osteons on crack propagation and effective toughness in the beam is still unknown.

In the current study, our objective was to use a computational mechanics approach to investigate the role of anisotropy of fracture toughness and of altered microstructure in crack growth trajectory and force needed to propagate a crack in cortical bone under bending, assuming LEFM theory. We altered anisotropy of fracture toughness in a beam loaded in three-point bending by including an osteon and varying its fracture toughness, location and diameter, and by varying the number of

osteons. Our hypothesis was that the force needed to propagate a crack would increase with the degree of anisotropy, with more material remaining to resist bending, with increasing osteon diameter, and with increasing numbers of osteons.

4.2 Methods

The computational models were analyzed with FRANC2D (Fracture Analysis Code, 2 Dimensions), a finite element code for performing fracture mechanics analysis of 2D structures under LEFM assumptions. This semi-automated code has been used in the engineering literature [19] as a more interactive approach and includes the traditional tasks of pre-processing, processing, and post-processing. The main features of the code are to automatically refine the mesh around the crack tip (Figure 4.1E) without losing unaffected structural information, to predict the crack trajectory in mixed-mode fracture, and to calculate the stress intensity factors [20-22]. A triangulation algorithm generates transition meshes between the extended crack path and the unaffected portion of the mesh [20]. Quarter-point elements are meshed around the crack tip to model the LEFM singularity. Additional refinement of the mesh around the crack tip can be specified by the user. Direction of propagation (kink angle) at each step is determined by maximum tensile stress theory. Calculations were virtually instantaneous and required no user interaction except specifying a crack increment at the beginning of each simulation.

A 2x20 mm, pre-notched (0.05 mm initial crack on tensile side) beam was created in FRANC2D and loaded in three-point bending. A plane strain assumption

was carried out in the simulations. Initial element side-length was 0.2 mm based on a mesh convergence for correct beam bending stresses. As the crack propagated, the mesh around the crack tip was refined, and quarter-point elements inserted. The interstitial matrix was defined as an isotropic material whereas osteons were modeled as a linear elastic, orthotropic material (Table 4.1), assuming osteons and interstitial matrix were perfectly bonded. Osteons were perfectly parallel to each other. The material properties were based on nanoindentation measurements for elastic moduli [23,24] and theoretical calculations for shear moduli and Poisson's ration [25]. Anisotropic fracture toughness was based on experimental measurements [9,15].

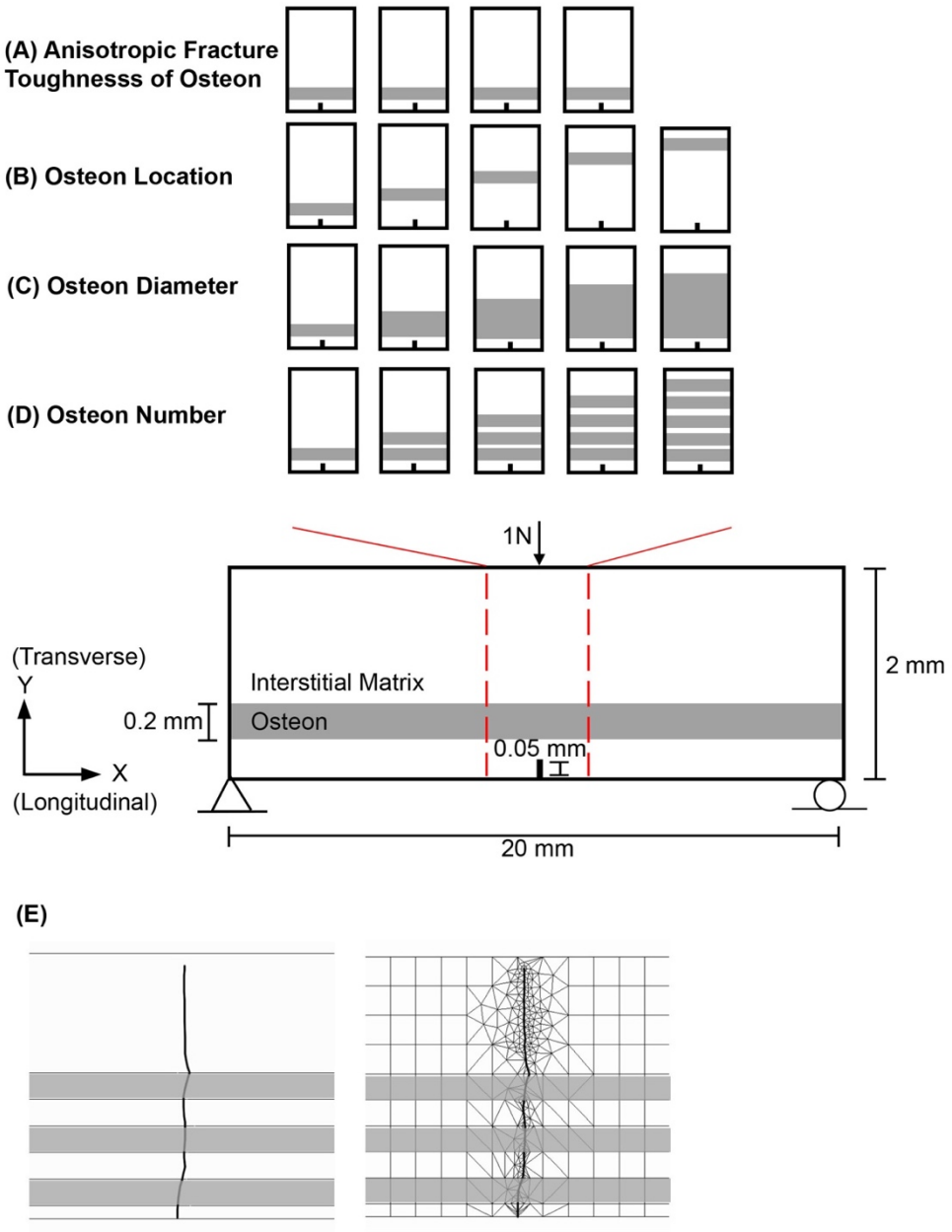

Figure 4.1 *A 2x20 mm beam loaded in 3-point bending with pre-notched central crack of 0.05 mm length. Model geometry for varying cases of (A) anisotropic fracture toughness of osteon (n = 1 osteon, d = 0.2 mm, K_{Ix} = 2 MPa√m, K_{Iy} = 2,4,6,8 MPa√m), (B) osteon location (n = 1 osteon, d = 0.2 mm), (C) osteon diameter (n = 1 osteon, d = 0.2, 0.4, 0.6, 0.8, 1 mm), (D) osteon number (n = 1-5 osteon(s), d = 0.2 mm). (E) Meshes were automatically refined along the crack trajectory.*

Table 4.1 *Material properties of interstitial matrix and osteons for all simulations except when K_{Iy} of the single osteon was varied from 2-8 MPa√m* [9,23-25].

Interstitial matrix: Isotropic			
E = 27 GPa	G = 7 GPa	v = 0.2	K_I = 3 MPa√m
Osteon: Orthotropic			
E_x = 25 GPa	G_{xy} = 7 GPa	v_{xy} = 0.2	K_{Ix} = 2 MPa√m
E_y = 17 GPa		v_{yz} = 0.3	K_{Iy} = 6 MPa√m
E_z = 17 GPa		v_{xz} = 0.2	

We initially included a single osteon within the beam and altered fracture toughness of the osteon (n = 1 osteon, diameter d = 0.2 mm, K_{Ix} = 2 MPa√m, K_{Iy} = 2, 4, 6, 8 MPa√m, Figure 4.1A), and its location (n = 1 osteon, diameter d = 0.2 mm in 5 locations, Figure 4.1B) and diameter (n = 1 osteon, d = 0.2, 0.4, 0.6, 0.8, 1 mm, Figure 4.1C) for different simulation cases. Then we increased the number of osteons (n = 1-5, d = 0.2 mm, Figure 4.1D). In our models, we neglected the contribution from the cement line (thickness 1 – 2 μm), which is much smaller than the diameter of the osteons (100 – 300 μm). Crack trajectory was examined. Stress intensity factors were calculated by the displacement correlation technique. The effective driving force (K_{eff}) at the crack tip was calculated from $\sqrt{(K_I^2+K_{II}^2)}$. To calculate the force needed to propagate a crack, we defined the effective fracture toughness (K_{ceff}) for the local system as a resisting force. No data on the effective mixed-mode fracture toughness of cortical bone were available in the literature. Therefore, the effective mixed-mode fracture toughness (K_{ceff}) was defined as a linear function (Figure 4.2), representing the local resisting force in the system. With $K_{eff} = K_{ceff}$, normalized critical load was calculated using the ratio, K_{ceff}/K_{eff}, indicating the load needed to propagate a unit length of a crack.

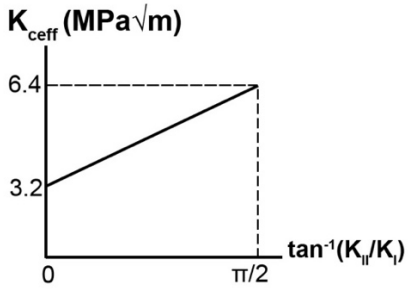

Figure 4.2 *To calculate force needed to propagate a crack requires defining the effective fracture toughness (K_{ceff}) for the local system as a resisting force. No available data on the effective mixed-mode fracture toughness of cortical bone in the literature. The effective mixed-mode fracture toughness (K_{ceff}) was defined as a linear function, representing the local resisting force in the system.*

4.3 Results

We first examined the effect of anisotropy of fracture toughness (Figure 4.3). As K_{Iy} increased (anisotropy of osteon increased), the crack trajectory moved into the longitudinal direction (parallel to the axis of osteon) and the normalized critical load, calculated as the ratio of K_{ceff}/K_{eff}, increased ($r^2 = 0.89$, $p = 0.06$). When we varied the location, the normalized critical load of a single osteon was negatively correlated with osteon location ($r^2 = 0.99$, $p < 0.05$, Figure 4.4A). The adjacent location (blue point in Figure 4.4A) was omitted from the regression due to proximity to the initial crack. When osteon diameter was increased, normalized critical load increased ($r^2 = 0.82$, $p < 0.05$, Figure 4.4B). When multiple osteons were included, normalized critical load was positively correlated with the number of osteons. As expected, a beam with 5 osteons presented the most resistance to crack propagation ($r^2 = 0.70$, $p = 0.08$, Figure 4.4C). However, the effect of increased numbers of osteons was less than the other

parameters examined.

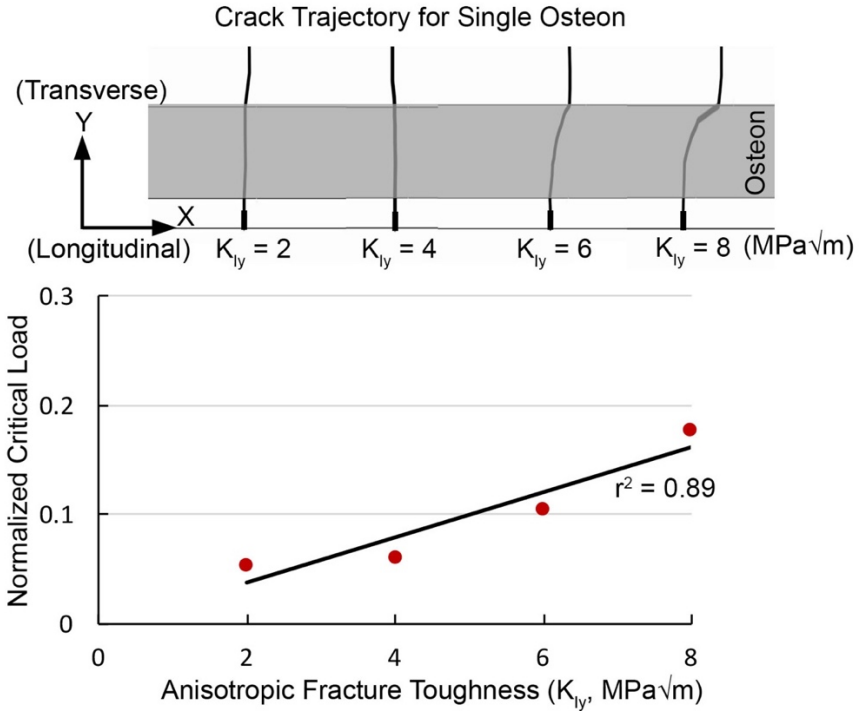

Figure 4.3 *Crack trajectories for varying fracture toughness K_{Iy} of a single osteon. As K_{Iy} increased (K_{Ix} = 2 MPa√m), the crack propagated more longitudinally (parallel to the axis of osteon) and normalized critical load increased (r^2 = 0.89, p = 0.06).*

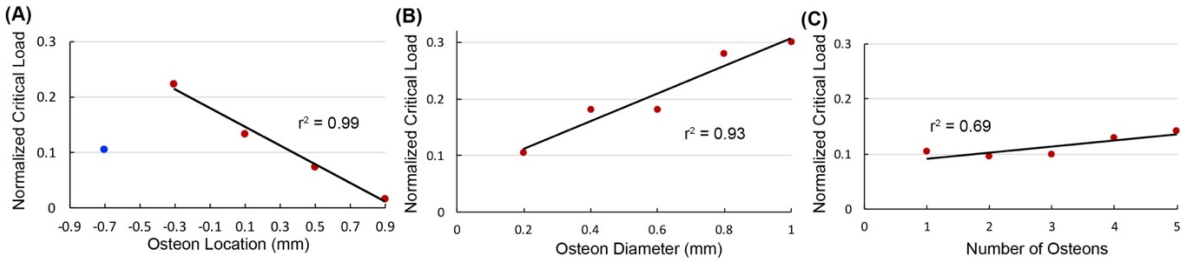

Figure 4.4 *Osteon location, diameter and number had differing influences on the force to propagate the initial crack when loaded in bending. Normalized critical load (A) decreased with osteon location moving towards the point of load application (r^2 = 0.99, p < 0.05); (B) increased as osteons became larger (r^2 = 0.93, p < 0.05); and, (C) gradually increased with increasing numbers of osteons (r^2 = 0.69, p = 0.08). For the relationship with osteon location relative to the initial crack, the adjacent location (blue point) was*

omitted from the regression due to proximity to the osteon, as discussed in the Results.

4.4 Discussion

This study used a computational mechanics approach to evaluate the role of anisotropy of fracture toughness and of altered microstructure in crack growth trajectory and force to propagate a crack in cortical bone. The force needed to propagate a crack was higher as the degree of anisotropy increased. In addition, the crack propagated more transversely as the ratio of transverse to longitudinal fracture toughness increased. Normalized critical load (K_{ceff}/K_{eff}) increased as the number of osteons increased, as more material remained to resist bending, and with a thicker single osteon.

With an increasing degree of anisotropy, indicating increased transverse fracture toughness, the crack trajectory moved more longitudinally and became more parallel to the axis of the osteon (Figure 4.3). Previous experimental studies reported lower measured longitudinal fracture toughness [8,9], indicating lower energy was needed to propagate in the longitudinal direction (parallel to the axis of osteon). In prior simulations, the main determinant for deflecting at or penetrating into an osteon was the ratio of strength between the osteon and cement line [26]. However, fracture toughness in this previous study was modeled as isotropic. In the current study, we implemented varying anisotropic fracture toughness values and showed that the crack propagation trajectory depended on the ratio of fracture toughness in the transverse and longitudinal directions. When the transverse fracture toughness was larger than

that in longitudinal direction (anisotropic fracture toughness), the crack propagated longitudinally. When applied to the crack morphology observed clinically, this finding suggests that the straight crack trajectory present in individuals with AFF could result from increased isotropic material properties due to reduced tissue heterogeneity [27].

Varying osteon location demonstrated the role of the bending stress state and the contribution of material resistance to bending. Longitudinal bending stress is proportional to $1/h^2$ according to beam theory [28], in which h is the depth of the uncracked (intact) section of the beam. The maximum critical load was for h = 1.3 mm when the crack tip exited the single osteon in the first location (-0.7 mm). As the crack tip exited from osteons located deeper in the material, less material remained to resist bending; therefore, the crack propagated more easily, as indicated by lower critical loads (Figure 4.4A).

The effects of osteon diameter were more complex, reflecting the combined effects of bending stress state and material distribution relative to the neutral axis. The absence of a Haversian canal in the model osteons was a limitation in this study, particularly for the osteon diameter simulation. Experimentally, as osteon size increases, Haversian canals are also larger, increasing the porosity of the bone tissue and reducing the fracture toughness [11,29]. This behavior was not captured by our simple osteon model when we altered the diameter. Therefore, to investigate the overall fracture toughness of bone, we suggest incorporating porosity in the bone tissue in future computational models.

When additional osteons were modeled, the heterogeneity of the material increased, and the load required to propagate cracks increased (Figure 4.4C). This

increase was also consistent with experimental measurements in bone of elevated fracture toughness with increased density of small osteons [11,29].

The current study utilized a 2D model to evaluate the contribution of microstructural features and fracture toughness to crack trajectory and force needed for crack propagation. This model could not capture the crack growth behavior in the radial/circumferential plane. Nevertheless, our simulations provide insight into crack growth when comparing isotropic and anisotropic material behavior. Another limitation of this study was the assumption of a linear relationship for effective fracture toughness as a function of mode mixity (Figure 4.2). To calculate normalized critical load, representing the required load to propagate a unit of crack, required defining the effective fracture toughness for the local system as a resisting force. No data on the effective mixed-mode fracture toughness of cortical bone are available in the literature. Therefore, the effective fracture toughness values used herein were based on experimental data from fracture toughness of cortical bone measured individually in both transverse and longitudinal directions [9].

In summary, the current study provided additional insights into tissue failure at the microscale. The anisotropy of cortical bone, osteon location, and osteon numbers were critical to increasing the fracture toughness of cortical tissue loaded in bending. Cortical bone with more osteons located further away from the applied loads to maximize intact material would withstand more load before propagating cracks and fracturing.

References

1. O'Brien FJ, Taylor D, Lee TC. The effect of bone microstructure on the initiation and growth of microcracks. Journal of Orthopaedic Research. 2005;23(2):475-80.

2. Taylor D, Hazenberg JG, Lee TC. Living with cracks: damage and repair in human bone. Nature Materials. 2007;6(4):263-8.

3. Nyman JS, Reyes M, Wang X. Effect of ultrastructural changes on the toughness of bone. Micron. 2005;36(7):566-82.

4. Guo XE, He M, Goldstein SA. Understanding cement line interface in bone tissue: a linear fracture mechanics approach. American Society of Mechanical Engineering. 1995;29:303-.

5. Evans AG, He MY, Hutchinson JW. Interface debonding and fiber cracking in brittle matrix composites. Journal of the American Ceramic Society. 1989;72(12):2300-3.

6. Nalla RK, Kruzic JJ, Kinney JH, Ritchie RO. Effect of aging on the toughness of human cortical bone: evaluation by R-curves. Bone. 2004;35(6):1240-6.

7. Vashishth D. Rising crack-growth-resistance behavior in cortical bone:: implications for toughness measurements. Journal of Biomechanics. 2004;37(6):943-6.

8. Phelps J, Hubbard G, Wang X, Agrawal C. Microstructural heterogeneity and the fracture toughness of bone. Journal of Biomedical Materials Research. 2000;51(4):735-41.

9. Koester KJ, Iii JA, Ritchie R. The true toughness of human cortical bone measured with realistically short cracks. Nature Materials. 2008;7(8):672.

10. Wright T, Hayes W. Fracture mechanics parameters for compact bone—effects of density and specimen thickness. Journal of Biomechanics. 1977;10(7):419427-25430.

11. Yeni Y, Brown C, Wang Z, Norman T. The influence of bone morphology on fracture toughness of the human femur and tibia. Bone. 1997;21(5):453-9.

12. Ural A, Vashishth D. Anisotropy of age-related toughness loss in human cortical bone: a finite element study. Journal of Biomechanics. 2007;40(7):1606-14.

13. Müller W, Schmauder S. Stress-intensity factors of r-cracks in fiber-reinforced composites under thermal and mechanical loading. International Journal of Fracture. 1993;59(4):307-43.

14. Erdogan F, Gupta G. The inclusion problem with a crack crossing the boundary. International Journal of Fracture. 1975;11(1):13-27.

15. Norman TL, Vashishth D, Burr D. Fracture toughness of human bone under tension. Journal of Biomechanics. 1995;28(3):309313-11320.

16. Bonfield W. Advances in the fracture mechanics of cortical bone. Journal of Biomechanics. 1987;20(11-12):1071-81.

17. Guo X, Liang L, Goldstein S. Micromechanics of osteonal cortical bone fracture. Journal of Biomechanical Engineering. 1998;120(1):112-7.

18. Ural A, Vashishth D. Cohesive finite element modeling of age-related toughness loss in human cortical bone. Journal of Biomechanics. 2006;39(16):2974-82.

19. Yan X. Automated simulation of fatigue crack propagation for two-dimensional linear elastic fracture mechanics problems by boundary element method. Engineering Fracture Mechanics. 2007;74(14):2225-46.

20. Bittencourt T, Wawrzynek P, Ingraffea A, Sousa J. Quasi-automatic simulation of crack propagation for 2D LEFM problems. Engineering Fracture Mechanics. 1996;55(2):321-34.

21. Wawrzynek PA, Ingraffea A. Interactive finite element analysis of fracture processes: an integrated approach. Theoretical and Applied Fracture Mechanics. 1987;8(2):137-50.

22. Wawrzynek PA, Ingraffea AR. An interactive approach to local remeshing around a propagating crack. Finite Elements in Analysis and Design. 1989;5(1):87-96.

23. Fan Z, Swadener J, Rho J, Roy M, Pharr G. Anisotropic properties of human tibial cortical bone as measured by nanoindentation. Journal of Orthopaedic Research. 2002;20(4):806-10.

24. Donnelly E, Boskey AL, Baker SP, Van der Meulen MC. Effects of tissue age on bone tissue material composition and nanomechanical properties in the rat cortex. Journal of Biomedical Materials Research. 2010;92(3):1048-56.

25. Yoon YJ, Cowin SC. An estimate of anisotropic poroelastic constants of an osteon. Biomechanics and Modeling in Mechanobiology. 2008;7(1):13-26.

26. Mischinski S, Ural A. Finite element modeling of microcrack growth in cortical bone. Journal of Applied Mechanics. 2011;78(4):041016.

27. Lloyd AA, Gludovatz B, Riedel C, et al. Atypical fracture with long-term bisphosphonate therapy is associated with altered cortical composition and reduced fracture resistance. Proceedings of the National Academy of Sciences. 2017:201704460.

28. Davies J, Leach P. First-order generalised beam theory. Journal of Constructional Steel Research. 1994;31(2-3):187-220.

29. McCalden RW, McGeough JA, Barker MB. Age-related changes in the tensile properties of cortical bone. The relative importance of changes in porosity, mineralization, and microstructure. The Journal of Bone and Joint Surgery. 1993;75(8):1193-205.

CHAPTER 5

SUMMARY AND FUTURE DIRECTIONS

5.1 Summary

Osteoporosis decreases bone quantity and quality[1-4]. In addition to adverse changes in bone geometry and density, osteoporosis decreases apparent level strength and stiffness[5,6]. Furthermore, bone tissue mineralization is reduced, and carbonate substitution and crystallinity are increased in animal models and patients[1,7]. Parathyroid hormone (PTH) is an FDA-approved anabolic osteoporosis treatment that increases bone mass and density in animal studies[8-10]; however, little is known about its effect on bone tissue composition and mechanics. Moreover, few studies have utilized a larger animal model, such as the sheep, with Haversian remodeling. Thus, the objectives of this work were first to examine the alterations of mechanical and material properties of cortical bone, and secondly of cancellous bone, with PTH treatment utilizing osteopenia sheep model. Tissue failure at the microscale is primarily affected by heterogeneity of material properties such as fracture toughness and microstructure[11,12]. To understand bone fragility, fracture behavior of bone at the tissue level should be examined. Fracture toughness of bone is anisotropic, but difficult to measure; anisotropic effects can be examined using simulations. Therefore, to gain additional insights into fracture behavior, we investigated the contributions of microstructure and fracture toughness to crack propagation using computational simulations as the third portion of this research.

We used an osteopenic sheep model to investigate the effects of PTH on mechanical performance and tissue properties of cortical bone. The effect of PTH treatment on the femur in the sheep model was greater at the micro- and nanoscale than at the whole bone level. The whole bone properties of the PTH-treated and vehicle groups were not different. PTH-treated bone tissue had lower fracture toughness and higher osteon density. At the tissue-level, PTH treatment also increased mineralization, decreased indentation modulus, and decreased hardness. Millimeter and nano-scale material properties were correlated with whole bone bending strength: fracture toughness and crystallinity explained 63% of the variation in whole-bone bending strength, but fatigue properties correlated little with whole bone bending strength or fracture toughness.

Although fracture toughness correlated with whole bone bending strength, the changes in fracture toughness were not evident at the whole bone level through differences in bending strength. Mechanical failure of a whole bone may occur from a single load, which is sensitive to whole bone strength, from cyclic loading that is sensitive to fatigue life, or from sensitivity to crack growth, reflected by fracture toughness. The altered tissue properties measured here reflected alterations in fatigue life and fracture toughness, which would cause mechanical failure independent of whole bone strength changes. In a short summary, the alterations at nano- and micro-scale contributed to tissue properties that describe bone failure; moreover, this study is the first to compare three mechanical failure properties: whole bone strength, fracture toughness, fatigue behavior.

Secondly, the effects of PTH treatment on bone tissue composition and mechanics of cancellous bone in an osteopenia sheep model were examined. Sheep treated with PTH gained less weight, analogous to PTH-treated humans who also lost weight, attributed to mild hypercalcemia reducing apatite[13]. PTH-treated samples experienced less energy dissipation before fatigue failure than those in the vehicle group. For microstructural measures, PTH increased the volume fraction of rod-type trabeculae and decreased mineralization. Correlating tissue composition, microstructure, and mechanical performance, 77% of the variation in energy dissipation was explained by volume fraction of rods and mineralization. When we examined tissue heterogeneity, carbonate-to-phosphate heterogeneity was increased and mineral-to-matrix heterogeneity was maintained with PTH treatment. Moreover, the results from AFM-IR showed the PTH-treated group had higher mineral-to-matrix ratio, crystallinity and collagen crosslink ratio and lower acid phosphate substitution ratio, in agreement with a faster tissue maturation process. In summary, our findings showed that PTH altered microarchitecture, material properties, and tissue heterogeneity to improve maintenance of mechanical properties following cyclic loading.

The third portion of this research modeled the fracture behavior of cortical bone at the tissue level. The role of anisotropy of fracture toughness and of altered microstructure in crack trajectory and the force needed to propagate a crack was investigated. When we examined the effect of anisotropy of fracture toughness, as the anisotropy of osteons increased (K_{Iy}) the crack trajectory propagated more longitudinally and the normalized critical load, calculated as the ratio of K_{ceff}/K_{eff}, increased. Considering the

effect of osteon location, the normalized critical load of a single osteon was negatively correlated with osteon location. When osteon diameter was increased, the normalized critical load increased. When multiple osteons were included, normalized critical load was positively correlated with number of osteons. As expected, a beam with more osteons presented the most resistance to crack propagation. In the first study, presented in Chapter 2, PTH increased osteon density and decreased fracture toughness in cortical bone tissue, which contradicts the simulation results (Chapter 4). Although resistance to crack propagation increased with increasing numbers of osteons, the central Haversian canal of the osteons was not included in the simulations. In addition to the Haversian canal of osteons, higher turnover rate induced by PTH treatment might decrease fracture toughness directly, which cannot be simulated in the model. In summary, the anisotropy of cortical bone, osteon location, and osteon numbers were critical to increasing the fracture toughness of cortical tissue loaded in bending. Cortical bone with more osteons located further away from the applied loads would withstand more load before propagating cracks and fracturing.

The first two studies presented in this body of work used an osteopenic sheep model to examine the effects of PTH treatment on mechanical and material properties in cortical and cancellous bone. In both bone types, PTH treatment affected fatigue behavior rather than resistance to monotonic loading, which could contributed to the 53% reduction in osteoporosis fracture risk seen clinically[14]. Fatigue life in cortical bone tissue was increased compared to bisphosphonate-treated samples whereas energy dissipation of cancellous bone under cyclic loading was preserved with PTH

treatment before failure. Alterations in tissue composition with PTH treatment were more evident at cancellous sites. Tissue heterogeneity was increased and mineralization was decreased in cancellous bone with PTH treatment. Correlations between microstructural features and mechanical and material properties were present in both bone tissue types. To our knowledge we are the first to investigate the contribution of anisotropic fracture toughness to crack propagation in bone at the tissue level, providing additional insights into tissue failure at the microscale and the cortical data presented in Chapter 2. Continued research into the alterations of material properties and microstructural features in bone tissue with aging and/or treatments will yield important information regarding fracture mechanisms.

5.2 Future Directions

Results of the three studies presented in this thesis have identified several future directions that can be divided roughly into two categories: continued and new research avenues. Continued research avenues include analysis of other anabolic osteoporosis treatments and three-dimensional anisotropic simulations of crack behavior. New research avenues include additional characterization techniques, combinations of drug holiday and sequential treatments, and bone tissue engineering.

5.2.1 Continued Research Avenues

5.2.1.1 Continued Osteoporosis Treatment Analysis

Investigating and comparing new anabolic osteoporosis treatments with PTH and anti-resorptive agents can help us to obtain a better understanding of treatment mechanisms. Abaloparatide (ABL), an anabolic osteoporosis treatment approved by the FDA less than a year ago, has been shown to reduce fracture risk by 57%[15]. ABL increases bone formation but not bone resorption, whereas teriparatide (PTH), investigated in this thesis, increases both bone formation and resorption, limiting bone mineral density gains[16,17]; thus, PTH-treated samples had increased porosity and less cortical bone formation[18]. ABL reduces the risk of both vertebral and non-vertebral fractures whereas PTH decreases the risk of vertebral fractures only[15,19,20]. In rat models, ABL increases bone mass and density in the femur and vertebrae, and monotonic compressive strength on vertebrae[21]. In clinical trials, bone mineral density is increased with ABL compared to placebo and PTH groups[22]. However, biomechanical properties such as fatigue behavior and tissue composition of ABL-treated bone are still unknown. Similar to the aims in this thesis, a better understanding of normal and osteoporotic bone function can be provided by determining the correlations between mechanical performance across different length-scales and tissue material properties.

5.2.1.2 Continued Three-dimensional Anisotropic Simulation

Our simulations are the first to examine anisotropic fracture properties. However, one of the limitations of our approach in Chapter 4 is the assumption that osteons are perfectly parallel to each other. By altering the orientations of osteons, cracks could propagate into the radial/circumferential plane, which would require a three-

dimensional simulation. FRANC3D can be utilized and taken the advantages of refining mesh along the crack tip. Models with osteons oriented 0, 30, 45, 60 degrees relative to the longitudinal direction can be examined. The results from the models will help us understand crack behavior in three dimensions with anisotropic fracture toughness and varying microstructures.

5.2.2 New Research Avenues

5.2.2.1 New Synchrotron Imaging Methods

Additional characterization techniques, such as transmission x-ray microscopy (TXM) with synchrotron radiation, can be applied to examine microstructures and tissue mineralization at nanoscale. TXM with synchrotron radiation is a novel imaging technique[23]. A monochromatic x-ray source is used to image samples through x-ray transmission, absorption and scattering. This method has been used for nondestructive high-resolution (approximately 30 nm) imaging and quantification of tissue mineralization[24]. Two dimensional images can be collected from TXM, and after imaging processing of tiling individual images, a 3D tomography of a structure is created[25]. Applying this technique to bone samples, the lacunar-canalicular network can be visualized, exploring the complex interconnected bone cell network[26]. Changes in lacunar-canalicular properties can affect the tissue permeability, which is important to bone nutrition and mechanotransduction[27,28]. In addition to mechanotransduction, critical contributors to fracture, such as microdamage and mineralization, can be investigated in three dimensions using synchrotron

imaging[29,30]. Applying this new technique to characterize tissue microstructural features and tissue mineralization will allow us to better understand the role of osteoporosis treatment at the nanoscale, and the effects on mechanotransduction, microdamage and mineralization that might ultimately affect the fracture risk.

5.2.2.2 New Combinations of Drug Holiday and Sequential Treatments

The effects of PTH treatment have been investigated and presented in Chapters 2 and 3. PTH treatment alone increased fatigue strength but did not have positive effects on whole bone strength; thus, a drug holiday and/or sequential treatments should be considered. Moreover, the combination of treatments (drug holiday, anabolic/anti-resorptive agents) that would best serve osteoporotic patients is still unclear. For sequential treatments, patients with treated with PTH during the first year and a bisphosphonate for the second year had increased BMD at the hip and spine after the first year and maintained BMD in the spine after the second year. On the other hand, patients with 2-years of PTH treatment had progressively increasing BMD in both hip and spine[31-33]. BMD decreased with PTH treatment for one year followed by one-year of placebo[32]. Long-term use of bisphosphonates in patients has shown unexpected adverse events such as osteonecrosis of jaw[34], atypical femoral fractures[35], and atrial fibrillation[36]; thus, a drug holiday after 5 years of treatment is considered for patients who are not at high risk for fracture[37]. Fracture risk was increased in patients who received 2-years of bisphosphonate treatment and up to 1-year drug holiday,[38] whereas women who received approximately 5 years of bisphosphonate treatment did not have increased fracture risk[39,40]. Continued

bisphosphonate treatment beyond 5 years had little benefit for BMD[41,42]. Even with all the clinical data, the optimal duration of therapy and the length of the holiday are still unknown. At present patients must assess the benefits and risk individually. Thus, for future studies, we can use the same sheep model as presented in this thesis, with several modifications including a Sham-operated group, treatment with PTH for 1 year followed by one year of alendronate treatment; or, 5 years of alendronate treatment followed by one year of drug holiday or one year of PTH treatment.

5.2.2.3 New Tissue Engineering

Beyond additional experimental techniques and comparison of other osteoporosis treatments, the knowledge of bone fracture behavior can be applied to tissue engineering and 3D tissue printing. Three dimensional printing (3DP) is a powder-based freeform fabrication method developed in the early 1990s[43]. The important parameters that control the quality of 3DP scaffolds are powder-packing density, powder flowability, layer thickness, binder drop volume and powder wettability[44]; thus, extensive optimization is needed to generate high-quality 3DP scaffolds. Several combinations of the material-binder system currently are used in 3DP bone scaffolds[44]. For example, starch-based scaffolds are biocompatible and can have the similar mechanical strength as trabecular bone[45]. The effective pore size on human fetal osteoblasts (hFOB) was studied in TCP scaffolds[46]; new bone formation was observed at the interconnected micro-pores in TCP scaffolds in the rat distal femur[47]. CaP ceramics scaffolds are widely used because of good osteoconductivity, bioactivity such as capillaries and vessel formation, and similarities to bone composition[48].

Osteoclast-like cells were confirmed with TRAP stained in CaP ceramics scaffolds[49]. However, 3DP has limitations. Two major limitations include poor mechanical performance and required minimum struts distance. Scaffolds made from TCP had a maximum compressive strength of 10.95 MPa[46] but compressive stiffness and yield strength have not been reported. Because of the low mechanical strength, most scaffolds are used in non-load bearing applications. On the other hand, a minimum struts distance is required so that the pore size of scaffolds has to be larger than 300 μm[50]; therefore, highly porous scaffolds are difficult to print.

3DP technology has great advantages for producing defined shapes with controlled porosity bone scaffolds, allowing medical device to be customized for patients. Applying the knowledge obtained in this thesis can help design optimized bone scaffold structures. For example, the volume fraction of rod-type trabeculae and mineralization were correlated with fatigue behavior compared to osteoporotic cancellous bone in sheep (Chapter 3). Therefore, if we can design the bone scaffolds with a great proportion of rod-like microstructure and lower mineralization, the scaffolds should preserve mechanical performance during cyclic loading. Specifically, finding the appropriate microstructural features for bone scaffolds to resist fatigue loading is possible and can be tested.

In summary, several future directions can be investigated based on the findings in this thesis. Analyzing another anabolic osteoporosis treatment, Abaloparatide, can provide more understanding of normal and osteoporotic bone function. Altering orientations of osteons in simulation models will help us understand crack behavior in three

dimensions with anisotropic fracture toughness and varying microstructures. Applying TXM imaging techniques can characterize tissue microstructural features and tissue mineralization, providing better understanding to the role of osteoporosis treatment at nanoscale, such as mechanotransduction, microdamage and mineralization, which might ultimately affect the fracture risk. For sequential and drug holiday study designs, we can use the same sheep model as presented here and include additional treatment groups to compare the outcomes of combining PTH and alendronate or including drug holidays. Last but not least, by taking the advantage of three dimensional printing, finding the appropriate microstructural features for bone scaffolds to resist fatigue loading would be possible.

References

1. McCreadie BR, Morris MD, Chen TC, et al. Bone tissue compositional differences in women with and without osteoporotic fracture. Bone. 2006;39(6):1190-5.

2. Burket JC, Brooks DJ, MacLeay JM, Baker SP, Boskey AL, van der Meulen MC. Variations in nanomechanical properties and tissue composition within trabeculae from an ovine model of osteoporosis and treatment. Bone. 2013;52(1):326-36.

3. Seeman E, Martin TJ. Co-administration of Antiresorptive and Anabolic Agents: A Missed Opportunity. Journal of Bone and Mineral Research. 2015;30(5):753-64.

4. Boskey A, Mendelsohn R. Infrared analysis of bone in health and disease. Journal of biomedical optics. 2005;10(3):031102-0311029.

5. Zioupos P, Currey J. Changes in the stiffness, strength, and toughness of human cortical bone with age. Bone. 1998;22(1):57-66.

6. McCalden RW, McGeough JA. Age-related changes in the compressive strength of cancellous bone. The relative importance of changes in density and trabecular architecture. JBJS. 1997;79(3):421-7.

7. Gadeleta S, Boskey A, Paschalis E, et al. A physical, chemical, and mechanical study of lumbar vertebrae from normal, ovariectomized, and nandrolone decanoate-treated cynomolgus monkeys (Macaca fascicularis). Bone. 2000;27(4):541-50.

8. Jilka RL, Weinstein RS, Bellido T, Roberson P, Parfitt AM, Manolagas SC. Increased bone formation by prevention of osteoblast apoptosis with parathyroid hormone. The Journal of clinical investigation. 1999;104(4):439-46.

9. Oxlund H, Ejersted C, Andreassen T, Tørring O, Nilsson M. Parathyroid hormone (1-34) and (1-84) stimulate cortical bone formation both from periosteum and endosteum. Calcified tissue international. 1993;53(6):394-9.

10. Fox J, Miller M, Newman M, Recker R, Turner C, Smith S. Effects of daily treatment with parathyroid hormone 1–84 for 16 months on density, architecture

and biomechanical properties of cortical bone in adult ovariectomized rhesus monkeys. Bone. 2007;41(3):321-30.

11. Akkus O, Yeni YN, Wasserman N. Fracture mechanics of cortical bone tissue: a hierarchical perspective. Critical Reviews™ in Biomedical Engineering. 2004;32(5&6).

12. Wang X, Puram S. The toughness of cortical bone and its relationship with age. Annals of biomedical engineering. 2004;32(1):123-35.

13. Schafer AL, Sellmeyer DE, Schwartz AV, et al. Change in undercarboxylated osteocalcin is associated with changes in body weight, fat mass, and adiponectin: parathyroid hormone (1-84) or alendronate therapy in postmenopausal women with osteoporosis (the PaTH study). The Journal of Clinical Endocrinology & Metabolism. 2011;96(12):E1982-E9.

14. Greenblatt D. Treatment of postmenopausal osteoporosis. Pharmacotherapy: The Journal of Human Pharmacology and Drug Therapy. 2005;25(4):574-84.

15. Miller PD, Hattersley G, Riis BJ, et al. Effect of abaloparatide vs placebo on new vertebral fractures in postmenopausal women with osteoporosis: a randomized clinical trial. Jama. 2016;316(7):722-33.

16. Potts JT, Gardella TJ. Progress, paradox, and potential. Annals of the New York Academy of Sciences. 2007;1117(1):196-208.

17. Recker RR, Marin F, Ish-Shalom S, et al. Comparative effects of teriparatide and strontium ranelate on bone biopsies and biochemical markers of bone turnover in postmenopausal women with osteoporosis. Journal of Bone and Mineral Research. 2009;24(8):1358-68.

18. Tsai JN, Uihlein AV, Lee H, et al. Teriparatide and denosumab, alone or combined, in women with postmenopausal osteoporosis: the DATA study randomised trial. The Lancet. 2013;382(9886):50-6.

19. Hadji P, Zanchetta J, Russo L, et al. The effect of teriparatide compared with risedronate on reduction of back pain in postmenopausal women with osteoporotic vertebral fractures. Osteoporosis International. 2012;23(8):2141-50.

20. Saag KG, Shane E, Boonen S, et al. Teriparatide or alendronate in glucocorticoid-induced osteoporosis. New England Journal of Medicine. 2007;357(20):2028-39.

21. Bahar H, Gallacher K, Downall J, Nelson CA, Shomali M, Hattersley G. Six weeks of daily abaloparatide treatment increased vertebral and femoral bone mineral density, microarchitecture and strength in ovariectomized osteopenic rats. Calcified tissue international. 2016;99(5):489-99.

22. Leder BZ, O'dea LSL, Zanchetta JR, et al. Effects of abaloparatide, a human parathyroid hormone-related peptide analog, on bone mineral density in postmenopausal women with osteoporosis. The Journal of Clinical Endocrinology & Metabolism. 2015;100(2):697-706.

23. Andrews J, Brennan S, Pianetta P, et al. Full-field transmission x-ray microscopy at SSRL. Journal of Physics: Conference Series: IOP Publishing; 2009. p. 012002.

24. Andrews JC, Almeida E, van der Meulen MC, et al. Nanoscale X-ray microscopic imaging of mammalian mineralized tissue. Microscopy and Microanalysis. 2010;16(3):327-36.

25. Liu Y, Meirer F, Williams PA, Wang J, Andrews JC, Pianetta P. TXM-Wizard: a program for advanced data collection and evaluation in full-field transmission X-ray microscopy. Journal of synchrotron radiation. 2012;19(2):281-7.

26. Pacureanu A, Langer M, Boller E, Tafforeau P, Peyrin F. Nanoscale imaging of the bone cell network with synchrotron X-ray tomography: optimization of acquisition setup. Medical physics. 2012;39(4):2229-38.

27. Gailani G, Benalla M, Mahamud R, Cowin SC, Cardoso L. Experimental determination of the permeability in the lacunar-canalicular porosity of bone. Journal of biomechanical engineering. 2009;131(10):101007.

28. Burger EH, Klein-Nulend J. Mechanotransduction in bone—role of the lacuno-canalicular network. The FASEB Journal. 1999;13(9001):S101-S12.

29. Larrue A, Rattner A, Peter Z-A, et al. Synchrotron radiation micro-CT at the micrometer scale for the analysis of the three-dimensional morphology of microcracks in human trabecular bone. PLoS one. 2011;6(7):e21297.

30. Brock GR, Kim G, Ingraffea AR, Andrews JC, Pianetta P, van der Meulen MC. Nanoscale examination of microdamage in sheep cortical bone using synchrotron radiation transmission x-ray microscopy. PloS one. 2013;8(3):e57942.

31. Eastell R, Nickelsen T, Marin F, et al. Sequential treatment of severe postmenopausal osteoporosis after teriparatide: final results of the randomized, controlled European Study of Forsteo (EUROFORS). Journal of bone and mineral research. 2009;24(4):726-36.

32. Black DM, Bilezikian JP, Ensrud KE, et al. One year of alendronate after one year of parathyroid hormone (1–84) for osteoporosis. New England Journal of Medicine. 2005;353(6):555-65.

33. Rittmaster RS, Bolognese M, Ettinger MP, et al. Enhancement of bone mass in osteoporotic women with parathyroid hormone followed by alendronate. The Journal of Clinical Endocrinology & Metabolism. 2000;85(6):2129-34.

34. Khosla S, Burr D, Cauley J, et al. Bisphosphonate-associated osteonecrosis of the jaw: report of a task force of the American Society for Bone and Mineral Research. Journal of Bone and Mineral Research. 2007;22(10):1479-91.

35. Shane E, Burr D, Ebeling PR, et al. Atypical subtrochanteric and diaphyseal femoral fractures: report of a task force of the American Society for Bone and Mineral Research. Journal of Bone and Mineral Research. 2010;25(11):2267-94.

36. Cummings SR, Schwartz AV, Black DM. Alendronate and atrial fibrillation. New England Journal of Medicine. 2007;356(18):1895-6.

37. McClung M, Harris ST, Miller PD, et al. Bisphosphonate therapy for osteoporosis: benefits, risks, and drug holiday. The American journal of medicine. 2013;126(1):13-20.

38. Curtis JR, Westfall A, Cheng H, Delzell E, Saag K. Risk of hip fracture after bisphosphonate discontinuation: implications for a drug holiday. Osteoporosis international. 2008;19(11):1613.

39. Whitaker M, Guo J, Kehoe T, Benson G. Bisphosphonates for osteoporosis—where do we go from here? New England Journal of Medicine. 2012;366(22):2048-51.

40. Black DM, Schwartz AV, Ensrud KE, et al. Effects of continuing or stopping alendronate after 5 years of treatment: the Fracture Intervention Trial Long-term Extension (FLEX): a randomized trial. Jama. 2006;296(24):2927-38.

41. Food, Administration D. Background document for meeting of Advisory Committee for reproductive health drugs and drug safety and risk management advisory committee. Center for Drug Evaluation and Research. 2011:17-20.

42. Black DM, Bauer DC, Schwartz AV, Cummings SR, Rosen CJ. Continuing bisphosphonate treatment for osteoporosis—for whom and for how long? New England Journal of Medicine. 2012;366(22):2051-3.

43. Sachs EM, Haggerty JS, Cima MJ, Williams PA. Three-dimensional printing techniques. Google Patents; 1994.

44. Bose S, Vahabzadeh S, Bandyopadhyay A. Bone tissue engineering using 3D printing. Materials Today. 2013;16(12):496-504.

45. Salgado A, Coutinho O, Reis R. Novel starch-based scaffolds for bone tissue engineering: cytotoxicity, cell culture, and protein expression. Tissue engineering. 2004;10(3-4):465-74.

46. Tarafder S, Balla VK, Davies NM, Bandyopadhyay A, Bose S. Microwave-sintered 3D printed tricalcium phosphate scaffolds for bone tissue engineering. Journal of tissue engineering and regenerative medicine. 2013;7(8):631-41.

47. Tarafder S, Davies NM, Bandyopadhyay A, Bose S. 3D printed tricalcium phosphate bone tissue engineering scaffolds: effect of SrO and MgO doping on in vivo osteogenesis in a rat distal femoral defect model. Biomaterials Science. 2013;1(12):1250-9.

48. Becker ST, Bolte H, Schünemann K, et al. Endocultivation: the influence of delayed vs. simultaneous application of BMP-2 onto individually formed hydroxyapatite matrices for heterotopic bone induction. International journal of oral and maxillofacial surgery. 2012;41(9):1153-60.

49. Detsch R, Schaefer S, Deisinger U, Ziegler G, Seitz H, Leukers B. In vitro-osteoclastic activity studies on surfaces of 3D printed calcium phosphate scaffolds. Journal of biomaterials applications. 2011;26(3):359-80.

50. Khalyfa A, Vogt S, Weisser J, et al. Development of a new calcium phosphate powder-binder system for the 3D printing of patient specific implants. Journal of Materials Science: Materials in Medicine. 2007;18(5):909-16.

APPENDIX A: CHAPTER 2 DATA

Table A.1: Whole bone mechanical testing (4-point bending) for femurs of sheep used in the study in Chapter 2

Sample ID	Group	Moment of inertia (cm^4)	Bending stiffness ($N\text{-}m^2$)	Bending strength (N-m)
e191-1	Vehicle	0.80	70.3	169
e191-2	Vehicle	2.29	103.8	138
e191-3	Vehicle	1.27	94.8	148
e191-4	Vehicle	1.77	107.1	168
e191-5	Vehicle	1.81	70.5	104
e191-6	Vehicle	2.27	103.7	141
e191-7	PTH	4.31	94.7	116
e191-8	PTH	1.44	135.3	160
e191-9	PTH	1.93	130.1	192
e191-10	PTH	1.09	105.0	143
e191-11	PTH	1.56	79.7	118
e191-12	PTH	2.01	108.7	188
e191-13	PTH	2.41	113.3	220

Table A.2: Fatigue testing, fracture toughness testing and SEM data for cortical beams from mid-diaphyseal femurs of sheep used in the study in Chapter 2

Sample ID	Group	Initial modulus (GPa)	Cycles to failure	Modulus loss at failure (%)	Fracture toughness (Mpa√m)	Osteon density (#/mm^2)	Crack Length (Pixel)
e191-1	Vehicle	21.04	2006	23.49	7.17	20	59.998
e191-2	Vehicle	29.59	9629	34.27	5.69	15	57.45
e191-3	Vehicle	25.86	31351	NA	6.17	7	45.43
e191-4	Vehicle	26.5	4270	14.89	4.97	12	70.642
e191-5	Vehicle	31.29	1338	18.87	6.77	6	75.04
e191-6	Vehicle	29.5	2390	17.42	6.69	15	70.37
e191-7	PTH	28.01	23819	38.45	5.16	19	59.934
e191-8	PTH	24.44	47314	27.94	3.96	14	48.684
e191-9	PTH	30.36	11159	20.58	3.20	27	NA
e191-10	PTH	27.26	45447	37.31	7.15	16	72.094
e191-11	PTH	NA	NA	NA	5.51	43	NA
e191-12	PTH	28.26	1908	15.29	4.64	37	58.41
e191-13	PTH	24.79	31501	26.3	4.13	36	52.32

Table A.3: Nanomechanical and tissue composition data for mid-diaphyseal cortical bone of sheep used in the study in Chapter 2

Sample ID	Group	Distance (%)	Er (GPa)	H (MPa)	Min : Mat	CO : PO	Crystallinity	Peak height ratio
e191-1	Vehicle	10.0%	29.28	1127.00	6.39	0.216	0.038	1.52
e191-1	Vehicle	17.4%	30.55	1101.58	6.62	0.223	0.038	1.44
e191-1	Vehicle	24.7%	31.72	1150.43	7.01	0.218	0.037	1.40
e191-1	Vehicle	35.2%	30.64	1106.92	6.82	0.218	0.038	1.55
e191-1	Vehicle	45.2%	33.02	1196.00	6.83	0.236	0.038	1.57
e191-1	Vehicle	55.0%	32.25	1181.86	6.73	0.217	0.038	1.48
e191-1	Vehicle	66.0%	32.70	1253.08	6.76	0.220	0.038	1.66
e191-1	Vehicle	76.1%	32.54	1220.91	6.99	0.219	0.038	2.00
e191-1	Vehicle	85.3%	31.27	1203.00	7.01	0.220	0.038	2.10
e191-1	Vehicle	92.6%	30.36	1127.50	7.11	0.220	0.038	1.98
e191-1	Vehicle	100.0%	29.44	1071.15	7.43	0.219	0.038	2.00
e191-2	Vehicle	10.0%	30.84	1050.55	6.17	0.201	0.038	1.83
e191-2	Vehicle	17.6%	31.53	1118.50	6.70	0.196	0.039	1.31
e191-2	Vehicle	24.1%	30.58	1069.28	6.61	0.205	0.038	1.71
e191-2	Vehicle	34.0%	29.60	1006.18	6.69	0.207	0.039	1.49
e191-2	Vehicle	44.4%	31.10	1090.88	6.39	0.205	0.039	1.67
e191-2	Vehicle	53.9%	32.24	1143.61	6.85	0.201	0.039	1.68
e191-2	Vehicle	63.1%	31.16	1119.92	6.74	0.207	0.038	1.56
e191-2	Vehicle	73.7%	31.01	1113.32	6.72	0.207	0.038	1.61
e191-2	Vehicle	83.9%	32.22	1145.17	6.64	0.208	0.038	2.45
e191-2	Vehicle	91.7%	30.63	1058.95	6.85	0.207	0.038	1.37
e191-2	Vehicle	100.0%	30.20	1025.43	6.60	0.206	0.038	1.60
e191-3	Vehicle	10.0%	28.04	960.08	7.03	0.220	0.038	1.93
e191-3	Vehicle	21.3%	27.03	868.66	6.92	0.216	0.038	2.22
e191-3	Vehicle	32.5%	26.05	957.82	7.40	0.220	0.038	2.75
e191-3	Vehicle	43.8%	25.18	884.89	7.20	0.209	0.039	2.19
e191-3	Vehicle	55.0%	26.95	888.97	7.64	0.228	0.038	2.61
e191-3	Vehicle	66.3%	26.38	893.35	7.01	0.218	0.039	2.50
e191-3	Vehicle	77.5%	26.66	875.49	7.39	0.221	0.038	2.26
e191-3	Vehicle	88.8%	26.12	868.98	7.88	0.218	0.038	2.45
e191-3	Vehicle	100.0%	24.86	860.69	7.69	0.216	0.038	2.28
e191-4	Vehicle	10.0%	27.43	992.47	6.46	0.229	0.038	1.87
e191-4	Vehicle	21.3%	28.30	997.88	7.01	0.227	0.039	2.21

e191-4	Vehicle	32.5%	27.36	912.94	7.29	0.222	0.039	1.63
e191-4	Vehicle	43.8%	28.43	1050.44	7.49	0.219	0.038	2.73
e191-4	Vehicle	55.0%	29.19	1082.14	6.84	0.227	0.039	2.52
e191-4	Vehicle	66.3%	29.50	1056.05	7.37	0.220	0.039	2.46
e191-4	Vehicle	77.5%	27.81	1061.18	7.10	0.220	0.039	2.45
e191-4	Vehicle	88.8%	27.19	982.83	7.24	0.212	0.039	1.94
e191-4	Vehicle	100.0%	28.23	1050.00	7.33	0.213	0.038	1.82
e191-5	Vehicle	10.0%	28.82	1059.79	6.32	0.213	0.038	1.68
e191-5	Vehicle	20.0%	30.55	1037.53	7.06	0.215	0.038	1.87
e191-5	Vehicle	30.0%	31.97	1031.05	6.76	0.216	0.039	1.80
e191-5	Vehicle	40.0%	30.62	1022.37	6.70	0.225	0.038	1.91
e191-5	Vehicle	50.0%	32.88	1154.00	6.74	0.225	0.039	1.86
e191-5	Vehicle	60.0%	30.21	1075.90	6.76	0.219	0.038	2.05
e191-5	Vehicle	70.0%	29.58	1034.83	6.87	0.218	0.039	3.00
e191-5	Vehicle	80.0%	29.51	1134.63	6.92	0.212	0.039	2.27
e191-5	Vehicle	90.0%	28.24	953.28	7.29	0.201	0.039	2.18
e191-5	Vehicle	100.0%	26.38	1055.35	6.80	0.224	0.039	1.64
e191-6	Vehicle	10.0%	21.43	754.18	6.23	0.202	0.038	2.06
e191-6	Vehicle	17.7%	21.87	737.44	6.53	0.201	0.038	1.39
e191-6	Vehicle	26.2%	39.35	779.77	6.79	0.206	0.038	1.57
e191-6	Vehicle	35.8%	22.18	755.80	6.71	0.207	0.038	1.50
e191-6	Vehicle	45.2%	22.47	765.29	7.04	0.205	0.038	1.42
e191-6	Vehicle	55.7%	22.95	770.69	6.47	0.203	0.038	1.41
e191-6	Vehicle	66.7%	22.69	786.23	6.65	0.206	0.038	1.40
e191-6	Vehicle	76.5%	22.82	780.83	6.42	0.204	0.038	1.60
e191-6	Vehicle	85.5%	21.84	778.31	6.67	0.206	0.038	1.81
e191-6	Vehicle	92.9%	23.55	835.67	6.71	0.202	0.038	1.62
e191-6	Vehicle	100.0%	21.84	765.95	6.86	0.209	0.038	1.75
e191-7	PTH	10.0%	24.14	813.02	7.13	0.216	0.038	2.29
e191-7	PTH	21.3%	25.54	857.03	7.63	0.214	0.038	2.47
e191-7	PTH	32.5%	25.29	880.70	7.61	0.213	0.038	2.48
e191-7	PTH	43.8%	25.41	877.02	7.61	0.209	0.038	3.29
e191-7	PTH	55.0%	25.15	924.55	7.93	0.212	0.039	2.12
e191-7	PTH	66.3%	23.52	709.81	7.41	0.218	0.039	1.70
e191-7	PTH	77.5%	25.05	807.81	7.17	0.210	0.038	2.27
e191-7	PTH	88.8%	24.82	782.59	8.00	0.212	0.038	2.78
e191-7	PTH	100.0%	24.40	779.88	7.87	0.219	0.038	2.67
e191-8	PTH	10.0%	24.60	796.85	6.82	0.208	0.038	2.14

e191-8	PTH	21.3%	26.05	866.10	7.49	0.211	0.038	2.40
e191-8	PTH	32.5%	26.23	864.12	7.49	0.210	0.038	2.12
e191-8	PTH	43.8%	26.44	856.94	7.32	0.212	0.038	2.59
e191-8	PTH	55.0%	25.88	837.47	7.40	0.208	0.038	2.03
e191-8	PTH	66.3%	27.69	874.59	7.53	0.212	0.038	2.30
e191-8	PTH	77.5%	27.18	905.71	7.33	0.216	0.038	3.01
e191-8	PTH	88.8%	24.60	857.69	7.33	0.212	0.038	2.58
e191-8	PTH	100.0%	26.35	891.96	7.64	0.209	0.038	1.89
e191-9	PTH	10.0%	28.53	939.53	6.99	0.200	0.038	2.69
e191-9	PTH	20.0%	26.76	891.83	7.47	0.199	0.038	1.54
e191-9	PTH	30.0%	26.56	844.78	7.38	0.199	0.038	2.53
e191-9	PTH	40.0%	25.14	845.47	7.66	0.197	0.038	2.43
e191-9	PTH	50.0%	29.13	928.12	7.58	0.201	0.038	2.78
e191-9	PTH	60.0%	28.41	919.15	7.69	0.202	0.038	2.88
e191-9	PTH	70.0%	28.00	873.72	7.38	0.199	0.038	4.30
e191-9	PTH	80.0%	26.28	882.31	7.69	0.204	0.038	2.70
e191-9	PTH	90.0%	27.88	944.53	8.28	0.199	0.038	2.25
e191-9	PTH	100.0%	25.18	809.88	7.63	0.196	0.038	2.56
e191-10	PTH	10.0%	29.46	914.05	6.86	0.219	0.038	2.31
e191-10	PTH	21.3%	28.57	863.05	6.95	0.219	0.039	1.81
e191-10	PTH	32.5%	28.55	878.49	7.15	0.223	0.038	2.75
e191-10	PTH	43.8%	28.87	917.02	6.75	0.217	0.038	2.24
e191-10	PTH	55.0%	28.07	915.41	6.63	0.218	0.039	2.08
e191-10	PTH	66.3%	26.50	892.89	7.15	0.221	0.039	2.15
e191-10	PTH	77.5%	27.61	920.03	7.12	0.221	0.039	2.36
e191-10	PTH	88.8%	25.98	822.13	6.93	0.217	0.039	2.25
e191-10	PTH	100.0%	28.10	893.99	7.41	0.220	0.039	2.30
e191-11	PTH	10.0%	27.78	939.30	7.26	0.193	0.039	2.45
e191-11	PTH	20.0%	27.07	841.51	7.47	0.196	0.038	2.36
e191-11	PTH	30.0%	27.42	894.59	7.67	0.196	0.039	2.37
e191-11	PTH	40.0%	28.20	926.66	7.95	0.193	0.039	2.35
e191-11	PTH	50.0%	27.09	905.83	7.59	0.200	0.039	2.65
e191-11	PTH	60.0%	27.36	975.47	6.73	0.200	0.038	3.33
e191-11	PTH	70.0%	26.22	930.52	7.98	0.202	0.039	2.42
e191-11	PTH	80.0%	26.24	873.22	7.62	0.201	0.039	3.02
e191-11	PTH	90.0%	25.40	861.43	7.22	0.195	0.040	3.17
e191-11	PTH	100.0%	24.66	824.73	7.95	0.197	0.038	2.63
e191-12	PTH	10.0%	27.79	1010.03	6.60	0.222	0.038	1.64

e191-12	PTH	21.3%	28.54	946.37	6.64	0.218	0.037	1.89
e191-12	PTH	32.5%	31.18	1261.96	7.03	0.226	0.038	2.14
e191-12	PTH	43.8%	30.91	1077.77	6.88	0.213	0.038	1.97
e191-12	PTH	55.0%	30.72	981.97	7.23	0.216	0.039	2.54
e191-12	PTH	66.3%	33.63	1178.75	6.98	0.209	0.038	1.80
e191-12	PTH	77.5%	33.60	1137.78	7.19	0.224	0.038	2.21
e191-12	PTH	88.8%	31.89	1060.56	6.85	0.225	0.038	2.09
e191-12	PTH	100.0%	32.06	1210.00	7.35	0.222	0.038	2.07
e191-13	PTH	10.0%	24.67	864.58	6.33	0.200	0.037	2.00
e191-13	PTH	20.0%	25.32	808.53	7.15	0.204	0.037	1.62
e191-13	PTH	30.0%	25.39	785.26	7.46	0.210	0.037	1.73
e191-13	PTH	40.0%	25.62	846.23	7.20	0.209	0.038	1.73
e191-13	PTH	50.0%	26.38	888.17	7.24	0.218	0.038	2.23
e191-13	PTH	60.0%	25.67	863.43	6.91	0.217	0.038	1.71
e191-13	PTH	70.0%	25.03	842.35	7.15	0.212	0.037	2.19
e191-13	PTH	80.0%	25.82	861.61	7.32	0.214	0.038	2.22
e191-13	PTH	90.0%	27.37	896.19	7.60	0.210	0.038	2.00
e191-13	PTH	100.0%	25.72	852.03	7.77	0.206	0.038	3.17

Table A.4: Correlations between microstructures, mechanical and material properties data used in Chapter 2

Predictor	Independent variables	r^2	*p*-value
M_f	Crystallinity	0.6	0.002
$logN_f$	Min:Mat	0.27	0.09
K_{Ic}	Min:Mat	0.35	0.03
Crack length	Min:Mat	0.29	0.09
Work to failure	Osteon #	0.37	0.04
Min:Mat	Peak height ratio	0.85	<0.0001
M_f	Work to failure	0.22	0.12
M_f	Crack length	0.27	0.1
M_f	K_{Ic}	0.32	0.04
EI	K_{Ic}	0.56	0.003
$logN_f$	Work to failure	0.31	0.07
$logN_f$	Crack length	0.32	0.07
M_f	Crystallinity + K_{Ic}	0.63	0.03
M_f	Crystallinity + Work to failure	0.59	0.008
M_f	Crystallinity + Crack length	0.45	0.04
$logN_f$	Min:Mat + Work to failure	0.32	0.09
$logN_f$	Min:Mat + Crack length	0.42	0.11
K_{Ic}	Min:Mat + M_f	0.54	0.008
K_{Ic}	Min:Mat + EI	0.67	0.0016
crack length	Min:Mat + M_f + $logN_f$	0.38	0.1
crack length	Min:Mat + M_f	0.39	0.06
crack length	Min:Mat + $logN_f$	0.23	0.14
crack length	M_f + $logN_f$	0.36	0.07
Work to failure	Osteon# + M_f + $logN_f$	0.5	0.05
Work to failure	Osteon# + M_f + $logN_f$ + M_f*$logN_f$	0.98	<0.0001
Work to failure	Osteon# + M_f	0.31	0.08
Work to failure	Osteon# + M_f + Osteon#*M_f	0.56	0.022
Work to failure	Osteon# + logNf	0.55	0.02
Work to failure	Osteon# + $logN_f$ + Osteon#*$logN_f$	0.82	0.002
Work to failure	M_f + $logN_f$	0.45	0.04
Work to failure	M_f + $logN_f$ + M_f*$logN_f$	0.95	<0.0001

APPENDIX B: CHAPTER 3 DATA

Table B.1: Microstructural features for cancellous core from distal femurs of sheep used in the study in Chapter 3

Sample ID	Group	BV/TV	Conn. D. (#/mm^3)	Tb.Th (μm)	Tb.Sp (mm)
e191-1	Vehicle	0.293	1.56	231	5.88
e191-2	Vehicle	0.180	1.12	175	5.61
e191-3	Vehicle	0.191	1.19	195	4.77
e191-4	Vehicle	0.352	1.07	240	7.05
e191-5	Vehicle	0.212	1.03	183	4.31
e191-6	Vehicle	0.234	0.83	183	9.54
e191-7	PTH	0.266	1.35	217	3.53
e191-8	PTH	0.293	1.41	216	4.61
e191-9	PTH	0.229	1.34	206	3.71
e191-10	PTH	0.243	1.87	210	3.27
e191-11	PTH	0.227	1.63	170	7.08
e191-12	PTH	0.188	1.12	177	3.28
e191-13	PTH	0.196	1.02	204	4.53

Table B.2: Features for plate-like trabeculae in cancellous core of sheep femur used in the study in Chapter 3

Sample ID	Group	longitudinal Plate/BV	transverse Plate/BV	oblique Plate/BV	Plate V/BV	Plate number	mean Plate th. (μm)
e191-1	Vehicle	0.589	0.075	0.214	0.878	3.65	161
e191-2	Vehicle	0.602	0.069	0.175	0.846	4.05	127
e191-3	Vehicle	0.704	0.051	0.158	0.913	3.59	165
e191-4	Vehicle	0.764	0.039	0.144	0.947	3.65	154
e191-5	Vehicle	0.647	0.065	0.207	0.918	3.57	164
e191-6	Vehicle	0.692	0.052	0.143	0.888	3.93	133
e191-7	PTH	0.673	0.057	0.146	0.876	3.83	141
e191-8	PTH	0.619	0.066	0.201	0.886	3.40	184
e191-9	PTH	0.530	0.094	0.230	0.854	3.69	156
e191-10	PTH	0.457	0.079	0.235	0.771	3.51	170
e191-11	PTH	0.629	0.058	0.159	0.846	4.16	133
e191-12	PTH	0.630	0.043	0.113	0.786	3.27	185
e191-13	PTH	0.653	0.056	0.194	0.904	4.75	108

Table B.3: Features for rod-like trabeculae in cancellous core of sheep distal femur used in the study in Chapter 3

Sample ID	Group	longitudinal Rod/BV	transverse Rod/BV	Oblique Rod/BV	Rod V/BV	Rod number	mean Rod diameter (μm)
e191-1	Vehicle	0.016	0.060	0.047	0.122	2.59	143
e191-2	Vehicle	0.011	0.095	0.048	0.154	2.97	130
e191-3	Vehicle	0.008	0.047	0.033	0.088	2.48	128
e191-4	Vehicle	0.004	0.034	0.017	0.055	2.31	114
e191-5	Vehicle	0.007	0.044	0.031	0.082	2.36	136
e191-6	Vehicle	0.009	0.066	0.038	0.112	2.74	126
e191-7	PTH	0.019	0.067	0.037	0.124	2.72	129
e191-8	PTH	0.015	0.055	0.044	0.114	2.46	145
e191-9	PTH	0.013	0.072	0.061	0.146	2.68	145
e191-10	PTH	0.036	0.110	0.089	0.235	2.93	152
e191-11	PTH	0.016	0.084	0.055	0.154	3.09	123
e191-12	PTH	0.044	0.107	0.064	0.214	2.73	161
e191-13	PTH	0.010	0.048	0.039	0.096	3.58	76

Table B.4: Monotonic mechanical properties for cancellous core of sheep distal femur used in the study in Chapter 3 (data except ash fraction were analyzed by Remy Walk)

Sample ID	Group	Young's modulus (Mpa)	Yield stress (Mpa)	Ultimate stress (Mpa)	Total toughness to fracture (kJ/m^3)	Ash fraction (%)
e191-1	Vehicle	367	3.60	4.74	103	65.2
e191-2	Vehicle	652	4.08	6.92	145	78.3
e191-3	Vehicle	425	2.48	3.02	126	72.6
e191-4	Vehicle	1353	7.86	8.33	50	68.9
e191-5	Vehicle	1154	6.74	7.17	95	64.2
e191-6	Vehicle	715	3.84	5.06	124	52.0
e191-7	PTH	587	4.71	5.70	135	63.2
e191-8	PTH	386	1.99	3.72	74	86.6
e191-9	PTH	636	4.00	6.10	83	63.1
e191-10	PTH	593	3.23	3.50	87	54.2
e191-11	PTH	1216	6.99	7.90	189	52.3
e191-12	PTH	1306	7.07	7.72	199	55.8
e191-13	PTH	947	5.79	6.90	172	55.3

Table B.5: Fatigue behavior for cancellous core of sheep distal femur used in the study in Chapter 3

Sample ID	Group	Cycles to failure	Initial modulus (Mpa)	Modulus loss at 50% N_f (%)	Energy dissipation at 50% N_f (kJ/m^3)	DV/BV
e191-1	Vehicle	64561	127	NA		NA
e191-2	Vehicle	106000	323	7.4%	0.169	0.090
e191-3	Vehicle	15277	546	11.4%	0.258	0.035
e191-4	Vehicle	260658	710	14.7%	0.334	0.093
e191-5	Vehicle	3598702	573	25.2%	0.286	0.178
e191-6	Vehicle	796318	582	16.6%	0.349	0.041
e191-7	PTH	198800	568	2.6%	0.277	0.076
e191-8	PTH	424908	481	6.3%	0.251	0.073
e191-9	PTH	6844999	335	17.1%	0.203	0.218
e191-10	PTH	81	103	NA	NA	NA
e191-11	PTH	80107	555	5.4%	0.280	0.047
e191-12	PTH	5459	460	7.9%	0.223	0.057
e191-13	PTH	3052800	698	3.4%	0.165	0.087

Table B.6: Nanomechanics and tissue composition for cancellous core of sheep distal femur used in the study in Chapter 3

Sample ID	Group	Zone	Er (Gpa)	H (Mpa)	Min:Mat	Crystallinity
e191-1	Vehicle	Superficial	23.7	799	6.25	0.0386
e191-1	Vehicle	Intermediate	23.2	834	6.99	0.0386
e191-1	Vehicle	Central	22.0	730	7.46	0.0384
e191-2	Vehicle	Superficial	20.1	817	5.93	0.0397
e191-2	Vehicle	Intermediate	20.1	766	7.05	0.0392
e191-2	Vehicle	Central	21.5	852	7.59	0.0388
e191-3	Vehicle	Superficial	20.0	939	6.77	0.0392
e191-3	Vehicle	Intermediate	19.8	969	7.20	0.0388
e191-3	Vehicle	Central	19.6	948	8.02	0.0388
e191-4	Vehicle	Superficial	23.5	523	5.68	0.0367
e191-4	Vehicle	Intermediate	28.4	587	6.99	0.0370
e191-4	Vehicle	Central	29.9	642	7.36	0.0375
e191-5	Vehicle	Superficial	21.9	804	6.91	0.0385
e191-5	Vehicle	Intermediate	22.0	798	6.72	0.0389
e191-5	Vehicle	Central	21.4	744	6.91	0.0388
e191-6	Vehicle	Superficial	19.2	749	6.71	0.0388
e191-6	Vehicle	Intermediate	19.9	814	7.33	0.0383
e191-6	Vehicle	Central	20.3	866	8.04	0.0382
e191-7	PTH	Superficial	25.3	980	5.88	0.0390
e191-7	PTH	Intermediate	23.2	853	5.24	0.0390
e191-7	PTH	Central	22.0	790	5.83	0.0388
e191-8	PTH	Superficial	24.6	954	6.26	0.0392
e191-8	PTH	Intermediate	26.7	1049	6.59	0.0390
e191-8	PTH	Central	25.4	967	6.96	0.0390
e191-9	PTH	Superficial	21.3	584	5.99	0.0372
e191-9	PTH	Intermediate	24.0	714	6.19	0.0375
e191-9	PTH	Central	25.1	752	5.42	0.0371
e191-10	PTH	Superficial	21.2	732	5.87	0.0397
e191-10	PTH	Intermediate	28.6	965	6.07	0.0393
e191-10	PTH	Central	27.7	1044	5.69	0.0384
e191-11	PTH	Superficial	25.4	740	6.12	0.0402
e191-11	PTH	Intermediate	24.0	703	6.72	0.0394
e191-11	PTH	Central	25.4	794	7.11	0.0393

e191-12	PTH	Superficial	21.0	780	6.71	0.0384
e191-12	PTH	Intermediate	21.6	841	6.88	0.0386
e191-12	PTH	Central	20.7	811	7.02	0.0387
e191-13	PTH	Superficial	21.1	810	5.13	0.0397
e191-13	PTH	Intermediate	20.1	737	5.48	0.0394
e191-13	PTH	Central	21.4	770	5.91	0.0391

Table B.7: Correlations between microstructures, mechanical and material properties for cancellous core of sheep distal femur used in the study in Chapter 3

Predictor	Response (Independent Variables)	r^2	*p*-value
Energy Dissipation	Rod-type volume fraction	0.4	0.02*
Energy Dissipation	Rod-type Trab. Number	0.24	0.07**
Energy Dissipation	BV/TV	0.37	0.03*
Energy Dissipation	Oblique Rod volume	0.43	0.02*
Energy Dissipation	Min:Mat (superficial)	0.14	0.14
Energy Dissipation	Rod V, Rod N	0.5	0.03*
Energy Dissipation	Ash fraction, BV/TV	0.54	0.02*
Energy Dissipation	Rod V, Rod N, Min:Mat (sup.)	0.74	0.005*
Energy Dissipation	Rod V, Rod N, Min:Mat (centeral)	0.48	0.06**
Energy Dissipation	Rod V, Rod N, Min:Mat (inter.)	0.47	0.06**
Energy Dissipation	Rod V, Rod N, Min:Mat	0.66	0.05*
Modulus Reduction	Rod-type volume fraction	0.03	0.27
Modulus Reduction	Rod-type Trab. Number	0.27	0.06**
Modulus Reduction	Rod N, Min:Mat (sup.)	0.24	0.13
Modulus Reduction	Rod N, Crystallinity (sup.)	0.27	0.12
Modulus Reduction	Rod V, Rod N	0.22	0.15
Modulus Reduction	Ash fraction, BV/TV	0.19	0.17
Fatigue Life	Transverse Plate volume	0.5	0.009*
Fatigue Life	Oblique Plate volume	0.57	0.005*
Fatigue Life	Trans. & Obli. Plate volume	0.55	0.02*
Initial Modulus	Plate-type Trab. volume	0.36	0.03*
Initial Modulus	Longitudinal Plate volume	0.6	0.003*
Total Toughness	Plate thickness	0.26	0.06**

APPENDIX C: CHAPTER 4 DATA

Table C.1: Normalized critical load for altered anisotropic fracture toughness (K_{Iy} = 2,4,6,8 MPa$\sqrt{m}$) of cortical beam under 3-point bending in Chapter 4 (shaded rows represented osteon location)

	Normalized critical load			
Crack tip location (mm)	$K_{Iy} = 2$	$K_{Iy} = 4$	$K_{Iy} = 6$	$K_{Iy} = 8$
-0.95	0.000	0.000	0.003	0.000
-0.9	0.000	0.000	0.002	0.000
-0.8	0.039	0.062	0.054	0.041
-0.7	0.003	0.027	0.105	0.178
-0.6	0.002	0.012	0.035	0.128
-0.5	0.054	0.034	0.001	0.034
-0.4	0.004	0.004	0.001	0.003
-0.3	0.005	0.005	0.000	0.002
-0.2	0.000	0.000	0.000	0.003
-0.1	0.000	0.000	0.000	0.001
0	0.001	0.000	0.000	0.000
0.1	0.001	0.001	0.000	0.001
0.2	0.001	0.000	0.000	0.001
0.3	0.000	0.000	0.000	0.000
0.4	0.000	0.000	0.000	0.000
0.5	0.000	0.000	0.000	0.000
0.6	0.000	0.000	0.000	0.000
0.7	0.000	0.000	0.000	0.000
0.8	0.000	0.000	0.000	0.000
0.9	0.000	0.000	0.000	0.000

Table C.2: Normalized critical load for altered osteon locations of cortical beam under 3-point bending in Chapter 4 (shaded rows represented osteon location)

	Normalized critical load				
Crack tip location (mm)	Location 1	Location 2	Location 3	Location 4	Location 5
-0.95	0.003	0.001	0.007	0.006	0.006
-0.9	0.002	0.002	0.013	0.017	0.016
-0.8	0.054	0.001	0.004	0.008	0.008
-0.7	0.105	0.002	0.002	0.002	0.001
-0.6	0.035	0.000	0.002	0.000	0.001
-0.5	0.001	0.002	0.000	0.001	0.001
-0.4	0.001	0.077	0.001	0.003	0.000
-0.3	0.000	0.224	0.002	0.002	0.001
-0.2	0.000	0.021	0.002	0.000	0.000
-0.1	0.000	0.003	0.001	0.000	0.000
0	0.000	0.002	0.054	0.000	0.001
0.1	0.000	0.001	0.133	0.000	0.000
0.2	0.000	0.000	0.006	0.000	0.000
0.3	0.000	0.000	0.002	0.000	0.000
0.4	0.000	0.000	0.002	0.013	0.001
0.5	0.000	0.000	0.001	0.074	0.000
0.6	0.000	0.000	0.000	0.001	0.000
0.7	0.000	0.000	0.000	0.000	0.000
0.8	0.000	0.000	0.000	0.000	0.004
0.9	0.000	0.000	0.000	0.000	0.002

Table C.3: Normalized critical load for altered numbers of osteons (n = 1-5 osteons) of cortical beam under 3-point bending in Chapter 4 (shaded rows represented osteon location)

	Normalized critical load				
Crack tip location (mm)	1 Osteon	2 Osteon	3 Osteon	4 Osteon	5 Osteon
-0.95	0.003	0.001	0.000	0.000	0.000
-0.9	0.002	0.002	0.000	0.000	0.000
-0.8	0.054	0.026	0.049	0.036	0.069
-0.7	0.105	0.089	0.099	0.093	0.141
-0.6	0.035	0.042	0.057	0.038	0.051
-0.5	0.001	0.011	0.010	0.009	0.007
-0.4	0.001	0.014	0.031	0.039	0.027
-0.3	0.000	0.095	0.007	0.129	0.076
-0.2	0.000	0.021	0.017	0.016	0.033
-0.1	0.000	0.003	0.002	0.001	0.002
0	0.000	0.001	0.024	0.026	0.028
0.1	0.000	0.002	0.040	0.087	0.053
0.2	0.000	0.001	0.017	0.023	0.018
0.3	0.000	0.000	0.002	0.001	0.003
0.4	0.000	0.001	0.000	0.009	0.007
0.5	0.000	0.000	0.000	0.029	0.024
0.6	0.000	0.000	0.000	0.005	0.007
0.7	0.000	0.000	0.000	0.001	0.001
0.8	0.000	0.000	0.000	0.000	0.003
0.9	0.000	0.002	0.000	0.000	0.003

Table C.4: Normalized critical load for altered osteon thickness (t = 0.2-1 mm) of cortical beam under 3-point bending in Chapter 4 (shaded rows represented osteon location)

	Normalized critical load				
Crack tip location (mm)	0.2 mm	0.4 mm	0.6 mm	0.8 mm	1.0 mm
-0.95	0.003	0.002	0.002	0.000	0.000
-0.9	0.002	0.001	0.001	0.000	0.000
-0.8	0.054	0.034	0.040	0.038	0.047
-0.7	0.105	0.058	0.011	0.067	0.099
-0.6	0.035	0.130	0.014	0.131	0.174
-0.5	0.001	0.181	0.036	0.247	0.300
-0.4	0.001	0.040	0.098	0.263	0.281
-0.3	0.000	0.002	0.182	0.263	0.277
-0.2	0.000	0.000	0.026	0.280	0.247
-0.1	0.000	0.000	0.001	0.048	0.249
0	0.000	0.000	0.000	0.022	0.177
0.1	0.000	0.000	0.000	0.000	0.210
0.2	0.000	0.000	0.000	0.001	0.013
0.3	0.000	0.001	0.000	0.001	0.001
0.4	0.000	0.000	0.000	0.000	0.000
0.5	0.000	0.000	0.000	0.000	0.000
0.6	0.000	0.000	0.000	0.000	0.000
0.7	0.000	0.000	0.000	0.000	0.000
0.8	0.000	0.000	0.000	0.000	0.000
0.9	0.000	0.000	0.000	0.000	0.000

APPENDIX D: MATLAB CODE

D.1 Fracture Toughness Analysis

Matlab m-file for analyzing fracture toughness load-displacement data in the form of text files.

```
%Fracture Toughness calculation output
clc;
clear all;
close all;

%input data
prompt = {'input the file name', 'a=', 'W=', 'B=', 'S='};
dlg_title = 'input';
num_lines = 1;
input = inputdlg(prompt, dlg_title, num_lines);
str = input{1};
a = str2num(input{2})*10^(-3);
W = str2num(input{3})*10^(-3);
B = str2num(input{4})*10^(-3);
S = str2num(input{5})*10^(-3); %unit: mm

[ndata, text, alldata] = xlsread(str);
lengdata = length(ndata);

clear var text alldata

%offset
dis_ori = -1*ndata(19:end,4);    %mm
load_ori = -1*ndata(19:end,5);   %N
offsetdis = dis_ori(1);
offsetload = load_ori(1);
dis = dis_ori - offsetdis;
load = load_ori - offsetload;
moment = load*20/2; %N-mm

%plot load-disp plot
plot(dis, load,'linewidth', 2)
% title (str)
xlabel('displacement (mm)')
ylabel('force (N)')

%max values
[FORCEmax,index_max] = max(load); %max force
Dmax = dis(index_max);% displacement at fail (mm)
MOMENTmax = FORCEmax*20/2; %max moment (N-mm)

%calculate Kc
R = a/W;
```

```
Y = 3* (R^0.5) * (1.99-R*(1-R)*(2.15-3.93*R+2.7*R^2)) /
(2*(1+2*R)*((1-R)^(3/2)));  %ASTM
kic = FORCEmax*S*Y/B/(W^3/2)  %ASTM

pause
a=a*10^3;   %um
W=W*10^3;   %mm
kic=kic*10^-6;    %M N/m^3/2

%wrtie data to excel sheet
sfile=fopen(['output_FractureToughness_3076.xls'],'a');
fprintf(sfile,'%s,', date); % today's date
fprintf(sfile,'%s,',str);  %reading name (filename)
fprintf(sfile,'%.3f,',a);  %notch depth
fprintf(sfile,'%.3f,',W);  %width
fprintf(sfile,'%.3f,',FORCEmax); %maximum force
fprintf(sfile,'%.3f,',kic); %fracture toughness
fprintf(sfile,'\n');
fclose(sfile);
```

D.2 Fatigue Properties Analysis

Matlab m-files for analyzing fatigue testing load-displacement data in the form of text files.

```
%% cancellous fatigue data analysis
% convert Bose file to strain and stress matrix

% clc;
clear all;  close all;

prompt = 'Enter the file name:  ';
str = input(prompt, 's')

leng = 22.19   %eff length
area = 43.98   %area
[load, disp] = imtxt(str);
[nload, ndisp] = trunc(load, disp);

%% calculate/plot stress & strain
stress = nload(20:end-13)./area;
strain = ndisp(20:end-13)./leng;

% figure
% scatter(strain, stress)
% figure
% plot(strain, stress)

%% find each minimum strain --> cycle counts and E calculation
[E,cyc,minstra, indmin, indmax, indmax2] = calE(stress, strain);
```

```
figure
plot(strain(indmax(1):indmax2(1)), stress(indmax(1):indmax2(1)))
hold on
plot(strain(indmax(2):indmax2(2)), stress(indmax(2):indmax2(2)))
plot(strain(indmax(3):indmax2(3)), stress(indmax(3):indmax2(3)))
plot(strain(indmax(100):indmax2(100)),
stress(indmax(100):indmax2(100)))
% hold on
plot(strain(indmax(end):indmax2(end)),
stress(indmax(end):indmax2(end)))
hold off

% figure
% plot(minstra)
% hold on
% plot(cyc-1:cyc+4, strain(end-20:end-15))
% axis([1, cyc, -1*10^-3,0])
figure
plot(E)
E(1)
% axis([1, cyc-1, 0,350])

j = 1;
for i = 1:10:length(E)
    newE(j) = E(i);
    j = j+1;
end
figure
plot(newE)
```

```
%% import text file
function [load, disp] = imtxt(str)
    fileID = fopen(str);
    data = textscan(fileID, '%s %s %n %n %n %n %n');
    fclose(fileID);
    disp = data{4};
    load = data{5};
end
```

```
%% truncate load & disp

function [nnload, nndisp] = trunc(load, disp)
    load = load - load(2);
    disp = disp - disp(2);

    Q = fix(length(load)/29);
    R = rem(length(load),29);

    if R ~= 0
        newload = zeros(28,Q+1);
        newdisp = zeros(28,Q+1);
    else
        newload = zeros(28, Q);
        newdisp = zeros(28, Q);
```

```
    end

    j = 1;
    for i = 1:length(load)
            i = i+28*(i-1);
            newload(1:28, j) = load(i+1:i+28,1);
            newdisp(1:28, j) = disp(i+1:i+28,1);
            j = j+1;

            if i+57 > length(load)
                i = i+29;
                newload(1:R-1, j) = load(i+1:end);
                newdisp(1:R-1, j) = disp(i+1:end);
                break
            end
    end

    j = 1;
    for i = 1:Q
        i = 27*(i-1)+i;
        nnload(i:i+27,1) = newload(1:28, j);
        nndisp(i:i+27,1) = newdisp(1:28, j);
        j = j+1;
    end

    if R ~= 0
        nnload(28*Q+1:28*Q+R-1, 1) = newload(1:R-1, Q+1);
        nndisp(28*Q+1:28*Q+R-1, 1) = newdisp(1:R-1, Q+1);
    end
end
```

```
%% calculate E & cycle

function [E, cyc, minstra, indmin, indmax, indmax2] = calE(stress,
strain)
i = 1; cyc = 1;
   while 1
       [cycL] = [i:i+6];
       maxL = find(strain(cycL)==max(strain(cycL)));   %start of
loading portion
       [indxx] = [maxL(1)+ i-1];

       [cycL] = [indxx(1)+1 : indxx(1)+6];
       min2L = find(strain(cycL)==min(strain(cycL)));   %local
index in strain
       [indxn2] = [min2L(1)+ indxx(1)];    %global index in strain

       [cycL] = [indxn2(1)+1 : indxn2(1)+6];
       max2L = find(strain(cycL)==max(strain(cycL)));
       [indxx2] = [max2L(1)+ indxn2(1)];
%
%         figure
%         plot(strain(indxx(1):indxx2(1)),
stress(indxx(1):indxx2(1)))
%         axis([-2.5*10^-2,0, -1.8,0]);
```

```
%         pause

        [pf] = polyfit(strain(indxx(1):indxx2(1)),
stress(indxx(1):indxx2(1)), 2);
%         E(cyc) = 2*pf(1)*strain( floor((cyc + indx(1))/2) ) +
pf(2)
%         E(cyc+1) = 2*pf(1)*strain( floor((indx(1) + indx2(1))/2) )
+ pf(2)
        E(cyc) = 2*pf(1)*strain(indxn2(1)) + pf(2);

        minstra(cyc) = strain(indxn2(1));
        indmin(cyc) = indxn2(1);
        indmax(cyc) = indxx(1);
        indmax2(cyc) = indxx2(1);
        cyc = cyc+1;

        i = indxx2(1)+1;
        if i > length(strain)-20
            return
        end

    end
end
```